Microwave Radiometry of Vegetated Surfaces in Different Environments

by Yogesh Kumar Singh
Dipartimento di Ingegneria Civile e Ingegneria Informatica (DICII)
University of Rome Tor Vergata, Italy

Submitted in total fulfillment of the requirements of the degree of
Doctor of Philosophy

Date: 30th Nov 2013

Supervisor: **Prof. Paolo ferrazzoli**

Thesis committee: Prof. Domenico Solimini
Prof. Schiavon Giovanni
Dr.
Dr.

Day of the defense: 14th Jan 2014

Signature from head of PhD committee:

To my family

Jai Sai Nath

When I started writing my PhD thesis,
I began to wonder what would make the best opening lines.
I got many suggestions from my friends and colleagues (many thanks to all of them).
I analyzed that the whole duration of PhD was an amalgamation of different emotions,
tension, worries, happiness and most of all, confusion.
But the most overwhelming of all was the overall satisfaction of completing the task
I had undertaken.
So I choose to start my preface on a lighter note, with all the
enthralling memories of my unforgettable experience.
I could not think of one unique event because there were numerous episodes that put my mind in impasse.

I could tell you about the time I felt like almost drown in River Brahmaputra
Or losing my way in thick American forests.
Or, I could try to describe the first reprimand; I received from the director of my hostel
for not keeping the room clean.
Or perhaps, I could tell about my first conference/seminar, when my friends described me as ''more of teacher than student'' to illustrate the work carried out, but when in fact All
I was trying was to fight the feeling of running away howling.
The truth is that I found all the processes of research to be an incredibly fascinating game.
Sometimes you win and feel like you deserve the Nobel Prize for a silly calculation that a fresher could have done, and sometimes you lose and you cannot stop thinking about the return match
and a new strategy that will get you to the laurels.
With the impossibility of finding a single episode, I cannot do more than just say that all the words, electromagnetic theory and algorithms, the reader will find in the thesis are the result of a game that I enjoyed a lot to play both while winning or while trying to win.
My ultimate hope is that the reader will enjoy the content as well. But now I am too tempted to lay bare the content of this thesis!

Contents

Contents V
Preface VIII
Acknowledgement XI
List of Figures XIII
List of Tables XVII
List of Tables XVII
Glossary XVIII
1. Introduction 2
1.1 Basic Concepts 2
1.1.1 Brightness and power collected by an antenna 2
1.1.2 Blackbody radiation 2
1.1.3 Gray body radiation 4
1.1.4 Power-temperature correspondence 5
1.1.5 Measuring brightness temperatures from space and concerns 6
1.1.6 Polarization and Stokes parameters 9
1.1.7 Microwave electromagnetic spectrum 10
1.1.8 Microwave Radiometers 11
1.2 Applications 14
1.2.1 Soil Moisture Monitoring 14
1.2.2 Floods and Methods of its monitoring: 16
1.2.3 Forest monitoring 21
1.3 Historical notes about Microwave Passive Systems 23
1.4 Recent Satellite Missions 24
1.4.1 Advanced Microwave Scanning Radiometer (AMSR-E) 24
1.4.2 Soil Moisture and Ocean Salinity (SMOS) Mission: 30
1.5 Research objectives: 36
1.6 Organization of the Thesis 37

2 Microwave Emission of Land covers 38
2.1 Bare Soils 38
2.1.1 Physical properties of soils 38
2.1.2 Dielectric constant of soils 42
2.1.3 Soil surface roughness 46
2.1.4 Soil effective temperature 47
2.1.5 Microwave Emission Models 48
2.2 Vegetative Soil 51
2.3 Soil moisture retrieval algorithms 51
3 Flood Monitoring using Microwave Passive Remote Sensing (AMSR-E) in part of Brahmaputra basin, India 53
3.1 Introduction 53
3.2 Study Area 54
3.2.1 General properties 54
3.2.2 Regional Hydrology 55
3.3 AMSR-E Observations 56
3.3.1 Dynamic ranges of emissivity at vertical and horizontal polarization 56
3.3.2 Polarization Index 58
3.3.3 Fractional Water Surface 60
3.4 Correlations with ground truth 61
3.4.1 General considerations 61
3.4.2 Fractional Water Surface FWS vs Water Level WL 61
3.4.3 Polarization Index (PI) vs Water Level (WL) 62
3.5 Effect of falling raindrops 63
3.6 Rain pixels elimination 63
3.7 Possible use of PI to generate flood maps 66
3.8 Conclusion 68
4 Retrieving soil moisture over Forests : SMOS results and comparison with ground observation, other algorithms and independent observations 70

4.1 Introduction 70
4.2 SMOS Algorithm 72
4.2.1 General properties of SMOS Algorithm over forests 72
4.3 AMSRE Algorithm 76
4.4 Test Sites 76
4.4.1 SCAN/SNOTEL Nodes 76
4.4.2 BERMS (CANADA) 77
4.4.3 Indian sites 79
4.5 Results and Analysis 81
4.5.1 Retrieved Optical Depth 81
4.5.2 Retrieved Soil Moisture 84
4.6 Conclusion 99
Publications: 100
Paper 100
Conference Proceedings 100
Bibliography 101
Appendix A 117
Radiative Transfer Equation (RTE) 117
Appendix B 120
Taylor Diagrams 120

Preface

Earth functions as a system – a large, complex and dynamic one, but a system nonetheless. It is affected in measurable ways by external forces such as sun and its variability, and by the internal forces that are shaped by variations in the atmosphere, oceans, continents, life, and the complex web of interactions among them. According to Thermodynamics, the Earth can be defined as a closed system; In fact, it can only exchange energy, not matter, with its surroundings (asteroid penetrations and satellite remnants can be definitely neglected). Global water content on Earth, as any other matter, doesn't change; nevertheless water doesn't stand steady, but it is in continuous movement.

Water relentlessly changes in position and state, moving throughout the whole planet in liquid, gaseous, and solid states; this process is called the Water Cycle (Figure I). The Water Cycle affects, and is studied by, several disciplines, among them Oceanography, Meteorology, Hydrology, Agronomy etc.

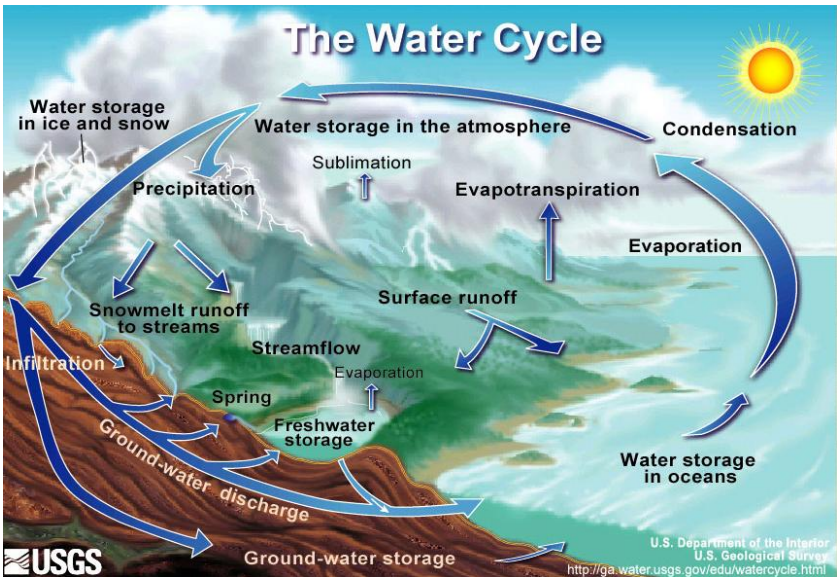

Figure I : The water cycle (from http:ga.water.usgs.gov)

"Water is at the heart of climate change and the impacts of climate variability.
Any assessment of climate change, its causes and impacts, must be based on significantly better observations of the water cycle."

(National Research Council 1999)

It is obvious that water is crucial for human life in the day-by-day needs, and it has the same importance in large-scale dynamics. The water cycle is, in fact, responsible for mitigating climate variations and homogenizing Earth's temperature, being at the same time a good tracer and forcer of climate changes.

Among the variables mirroring the water cycle, soil moisture is probably the most important one, or at least, it is the one whose knowledge would improve most of the characterization of the large-scale water dynamics. Measurements of soil moisture, both its global distribution and temporal variations, are required to study the water and carbon cycles. Soil moisture is fundamental to land surface hydrology,

affecting flooding, groundwater recharge, and evapotranspiration (Viterbo and Betts 1999). It also influences weather and climate via its influence on turbulent and radiative fluxes between the land surface and atmosphere (Entekhabi and Rodriguez-Iturbe 1994). The water status of land plants and microorganisms is partly regulated by soil water, so soil moisture is a key component of the terrestrial carbon cycle (Howard and Howard 1993). Accordingly, soil moisture is usually a state variable in hydrologic (Rodriguez-Iturbe 2000) ecological (Running 1994), and climate models (Robock 2000). The global distribution and temporal variations of soil moisture are sought both for analyses and modeling purposes.

Looking at the importance of the water cycle and of the role played by soil moisture for the same, a lot of progress in their knowledge and understanding has been exploited using the available technology. Prior to the space age (conventionally dated from 1957), humankind had never been able to take in the whole of a hemisphere in a single glance. In fact it had never had a global view of the world in which it lived. It was not until the first spacecraft went into orbit that our horizons expanded and we saw our planet as never before. During more than four decades of the spaceflights, planet Earth has been rediscovered through the systematic collection and analysis of vast amounts of information. During the last decades much effort has been spent by the scientific community in this direction and satellite microwave radiometry has been proposed as the optimal measurement technique. Satellite microwave radiometry presents several advantages: from one side, satellites permit the synoptic measurements of the Earth with a good revisit time; on the other side, microwave measurements can be acquired during both day-time and night-time regardless of the weather conditions (atmosphere is almost transparent at these frequencies). The attenuation properties of the atmosphere have been a hindrance to the development of Microwave and millimeter-wave, while the same have made it possible to sound the atmosphere. The millimeter wave spectrum contains two principal gaseous absorbers: oxygen and water vapor. In addition to gaseous absorption, aerosols (solid and liquid), produces significant attenuation.

A passive system is restricted to measuring the incoming radiation of wave spectrum in question. Hence, a passive system is restrained to that portion of radiation that is emitted with a reasonable intensity from the observed objects. Microwave radiation can directly measure the dielectric properties of the Earth's surface. Any change in these properties directly affects the reflectivity or emissivity measured by the passive microwave system. The dielectric property of the Earth's surface layer is in turn strongly dependent on the surface moisture content. Hence, an analysis of the microwave data can be related to the moisture content of the soil surface layer. *Microwave radiometry*, uses, the measurement of naturally emitted microwave radiation, which is sensitive to the presence of liquid water. When directed toward the earth's surface, it can reveal the quantity and distribution of water stored in vegetation and the first few centimeters of the soil, key components of the water cycle as well. Both the European Space Agency (ESA) and the National Aeronautics and Space Administration (NASA) have active programme to measure soil moisture using satellite microwave radiometers.

This Ph.D. thesis contains the result of research undertaken at the University of Rome "Tor Vergata", Doctorate Course on Computer Science, Control and Geoinformation.

The general subject is microwave radiometry of vegetated areas under different conditions of soil wetness. The research work can be subdivided into two parts.

The first part talks about analyzing in detail the multifrequency passive microwave signatures collected by AMSR-E instruments in the Brahmaputra Basin, Assam, India. The obtained results were analyzed to understand the interactions between microwave signatures and flooded surfaces and helped in exploiting the potential of microwave radiometry to monitor flood events.

The second part of the research involves refining, exploiting and testing the soil moisture retrieval algorithm of the SMOS mission, particularly over forests. The SMOS mission is a strategic program of the European Space Agency, aimed at monitoring soil moisture over land and ocean salinity using an L band radiometer.

Acknowledgement

Though only my name appears on the cover of this thesis, a great many people have contributed to its production. I owe my gratitude to all those people who have made this thesis possible and because of whom my experience at Rome has been one that I will cherish forever.

First and foremost I want to thank my advisor Prof. Paolo Ferrazzoli. It has been an honor to be his Ph.D. student. He has taught me, both consciously and un- consciously, not just about remote sensing but many others facets of life. I appreciate all his contributions of time, ideas, and funding to make my Ph.D. experience productive and stimulating. The joy and enthusiasm he has for his research was very motivational for me, even during tough times in the Ph.D. pursuit. I am also thankful for the excellent example he has provided as a dedicated, hardworking, unbiased and honest professor. I am grateful to him for holding me to a high research standard and enforcing strict validations for each research result, and thus teaching me how to do best research.

It is with immense gratitude that I acknowledge the support and help of Dr. Rachid Rahmoune. His insightful comments and constructive criticism at different stages of my research were thought-provoking and they helped me focus my ideas. I am indebted to him for his continuous encouragement and guidance.

I will forever be thankful to Prof Domenico Solimini. He is one of the best teachers that I have had in my life. He sets high standards for his students and he encourages and guides them to meet those standards. His enthusiasm and love for teaching is contagious. His lectures on Understanding Earth Observation, The Electromagnetic Foundations of Satellite Remote Sensing, have helped me a lot to understand the basic concepts of Remote Sensing and understanding its implementation in the research work.

I acknowledge the support of the Doctorate School of Tor Vergata University, Rome, Italy, for giving me the opportunity to carry out my doctoral research with the scholarship and LAZIODISU, for providing me accommodation. I cannot find words to express my gratitude for Sharon, Daya Singh, Mrs Bartolini, Lui Chi and all the staff of the International office of the University for providing all the administrative help during my stay in Rome.

I am thankful to Antonio Perrone, Prof Leila Guerriero, Prof Elisabetta Marino and all the former as well as the current PhD students for their constant help and support.

Most of the results described in this thesis would not have been obtained without a close collaboration with few laboratories. I owe a great deal of appreciation and gratitude to Dr. Y. Kerr and Dr. P. Richaume, CESBIO, Toulouse, France and Dr. R. Magagi, University of Sherbrooke, Canada. Thanks are also due to, ESA (Euopean Space Agency) for giving me opportunity to work on SMOS data, IMD, India, and State Water Resource Department, Lakhimpur, Assam, India for providing the daily rainfall and water level data, respectively, for the research.

I take this opportunity to owe my deepest gratitude to, Centre for Development of Advanced Computing (C-DAC), Pune, India, for allowing me to avail my study leave to peruse my PhD. I would like to thank Mrs Upasana Dutta, Dr. Medha Dhurandhar, Sandeep Srivastava, Dr. Manoj Khare, Late Dr. V. Sundarajan and Sunil Misar for all the support and encouragement both at personal and professional level.

Few people support you directly and few support you indirectly to achieve your goals in life. My deepest gratitude goes to my Brother in law Ashutosh Singh for his unflagging love and support

throughout my professional carrier.

I also thank my friends Mrs. Anjali Sharma, Saikat Sen Gupta, Deepak Nair, Raja Chakraborty, Cristina Vittucci (too many to list all here but you know who you are!) for providing support and friendship that I needed. Their support and care helped me overcome setbacks and stay focused on my study. I greatly value their friendship and I deeply appreciate their belief in me.

I would like to thank my family for all their love and encouragement. For my parents who raised me, supported me and did so many untold sacrifices for me in all my pursuits.

The acknowledgement will be incomplete, if I miss to thank my loving son, Achintya, whose eyes always inspired me to be through with this research work quickly.

A journey is easier when you travel together. Interdependence is certainly more valuable than independence. A very special thanks to my loving, supportive, encouraging, and patient wife, Aastha, whose faithful support during all the stages of this Ph.D. is so appreciated.

Above all, I owe it all to the Almighty God for granting me the wisdom, health and strength to undertake this research task and enabling me to its completion.

Thank you.

List of Figures

Figure I : The water cycle (from http:ga.water.usgs.gov) VIII

Figure 1.1 : Geometry of the incident radiation from an extended source on an antenna, from (Ulaby et al. 1981) 2

Figure 1.2 : Comparision of Plank radiation law with its low-frequency approximation (Rayleigh-Jeans law) for T = 300K and T = 6000K 3

Figure 1.3: Radiation incident upon an Earth-looking radiometer. relationship between the antenna temperature T_A, apparanet temperature T_{AP} and brightness temperature T_B, from Ulaby et al., (1981)] 5

Figure 1.4: Atmospheric attenuation by absorption at different frequencies (Solimini 2013) 7

Figure 1.5: Typical values of Faraday rotation angle as a function of TEC and frequency, from (P.531-6 et al. 2001)..... 8

Figure 1.6: A Total Power radiometer block diagram. from [(Ulaby et al. 1982)]..... 11

Figure 1.7: (a) total power, (b) Dicke, and (c) noise injection radiometer schematic [Skou, 1989] 13

Figure1.8: Cause of floods (http://drace-project.org/index.php/floods/human factor) 16

Figure 1.9: Photo of AMSR-E sensor unit during deployment testing at NASDA Tsukuba Space Center..... 25

Figure 1.10 : Overview of AMSR-E sensor unit 26

Figure 1.11: AMSR-E scanning geometry..... 27

Figure 1.12 : Schematic diagram of 89 GHz scan geometry. Beam centers of three successive scans are shown by solid (N), dotted (N+1), and thick-solid (N+2) lines. 28

Figure 1.13 : MIRAS arm and LICEF details. Courtesy ESA 31

Figure 1.14 : Geometric concentions for the definition of the (ξ, η) coordinates. 32

Figure 1.15 : SMOS (a) AF and (b) EAF-FOV in the cosine domain: (black) unit circle, (red) SMOS aliased zone borders, and (green) SMOS (a) AF-FOV and (b) EAF-FOV 32

Figure 1.16: (a) Radiometric Radiometric (blue) Accuracy and (red) Sensitivity, and (b) (blue) Incidence Angle and (red) Spatial Resolution [calculated using SEPS]. 33
Figure 1.17: (a) Stereo pairs of a regular icosahedron., (b) Subdividing the faces of a regular icosahedron: Gray and black regions represent the central hexagons for resolutions 1 and 2, respectively. 34

Figure 2.1 : USDA Soil classification triangle 39
Figure 2.2 : Relative real (upper curves) and imaginary (lower curves) parts of permittivity of two different soil types at f = 1.4GHz (left) and f = 5.0 GHz (right) vs. volumetric water content m_v (m^3/m^3). (Solimini 2013) 42
Figure 2.3 : Microwave emissivity of a fresh water at surface at L- (left), C- (middle) and X-band (right). 48
Figure 2.4: C-band emissivity of ideal flat-surface terrain: top left, dry (m_v = 12%); top right, moist (m_v = 21%); bottom left, wet (m_v = 31%); bottom right, very wet (m_v = 35%). Red curves refer to v polarization and the blue curves to h polarization. 49
Figure 2.5: L-band emissivity of ideal at-surface terrain: top left, dry (m_v = 12%); top right, moist (m_v = 21%); bottom left, wet (m_v = 31%); bottom right, very wet (m_v = 35%). Red curves refer to vertical polarization, the blue curves to horizontal polarization. Note that $e_v < 1$ at the pseudo-Brewster angle ..... .49

Figure 3.1: Study area:Lakhimpur District, Assam, India 55
Figure 3.2: Relationship between emissivities at H(e_H) and V(e_V) polarization at 10.65, 18.7 and 36.5 GHz for Dhalghat Site (2007) 57
Figure 3.3: Upper figures: PI (C, X and Ka band) vs Julian Date of 2007 for Dhalgat, Ghansari and Jamugurihat sites. Lower figures: corresponding trends of Water Level (WL). . 59
Figure 3.4: Temporal trend of F_{WS} at H and V Polarization as a function of Julian Date of 2007. Left: X band. Right: K_a band. 61
Figure 3.5: Scatterplots of Polarization Index (PI) vs. Water Level (WL) for Dhalgat, Ghansari and Jamugurihat sites. Left: 10 GHz. Right: 36 GHz. 62

Figure 3.6: Multitemporal trends. a) PI at 36 Ghz, b) PI at 10 Ghz and c) Water Level. Rainfall measurements are reported for comparison. 64
Figure 3.7: (a) Maps of F_{WSH}, F_{WSV} and PI at 10 GHz and 36 GHz on 29/06/2007, without rain (b): Maps of F_{WSH}, F_{WSV} and PI at 10 GHz and 36 GHz on 15/07/2007 with rain..... 65
Figure 3.8: Scatterplots of T_{BV} at 89.0 GHz vs. the difference T_{BV} (23 GHz – 89.0 GHz). Left: June 29 (no rain). Right: July 15 (rain)..... 66
Figure 3.9: Scatterplots of Polarization Index (PI) at X band vs. Water Level for Dhalgat, Ghansari..... 67
Figure 3.10: Maps of PI at X band of Lakhimpur District and neighboring areas, in 2007. Left hand side, top to bottom: March 18th (before flood), September 10th (during flood) and difference image. Right had side, top to bottom: September 10th (during flood), November 13th (after flood) and the difference image. White squares indicate the locations of water level stations and the blue line represents the main rivers..... 68

Figure 4.1: Trends of fitted radiative transfer parameters τF and ωF as a function of maximum yearly value of forest LAI, for broadleaf forests (Rahmoune 2013)…… 74
Figure 4.2: SCAN/SNOTEL network 77
Figure 4.3: CanEx-SM10 study area over BERMS 78
Figure 4.4: RFI map over India 80
Figure 4.5: RFI issues over forests (Western Ghats) in India (a) RFI maps at X and Y pol (b) TB at V and Ho pol. vs Julian Days 81
Figure 4.6: Global Map of Retreived optical depth..... 82
Figure 4.7: Optical Depth Maps obtained from SMOS (1-4 July 2011) (a) and..... 83
Figure 4.8: Retrieved optical depth vs. forest height (m) reported in (Masson et al. 2003a) 84
Figure 4.9: Tailor Diagram of S6 and S8 Model for 80% (a) & 40% (b) Forest Cover 87
Figure .4.10: Correlation coefficient and Root Mean Square Error S6 Model..... 88
Figure 4.11: Taylor Diagram for S6 and S8 model SMOS retrieved SM vs BERMS ground observed SM at OJP (a) and OBS (b) sites. 89

Figure 4.12: Scatterplot of All the SMOS retrieved SM and SCAN node SM obtained from case 1..... 91
Figure 4.13: Bar charts showing CC, RMSE, Ba and % of samples obatined for each case for 40 % FFO and 80 % FFO 93
Figure 4.14: Scatterplot of all the SMOS retrieved SM vs BERMS Ground observed SM obtained from case 1. 94
Figure 4.15: Comparison of Soil Moisture Retrieved from different algorithms vs. SCAN/SNOTEL Ground Observation over different forest land covers (80% forest (a), 40% forest (b) and low vegetation (c)). Results are given in form of a global scatterplot, including all nodes. 96

List of Tables

Table 1.1: Microwave Electromagnetic Spectrum 10

Table 1.2: Summary of Major Performance and Characteristic of AMSR-E..... 25

Table 2.1: Classification of soil particles as a function of their diameter (in mm)..... .39

Table 2.2: Properties of Soil as a function of Texture.....39

Table 2.3 : Details of parameters emperically determined by Dobson et., al. (1985) 44

Table 3.1: Minimum and maximum values of emissivities, and average PI values, on selected dates at X and Ka Bands..... 59

Table 3.2: Cumulative distribution of F_{WS} calculated at specific days using X band T_B values and surface temperature data provided by IMD. 60

Table 4.1: Correlation coefficient (CC), Root Mean Square Error (RMSE) and Bais (BA) for different SCAN nodes with respect to SMOS nodes averaged over 15Km buffer (with 80% forest) fraction for S6 and S8 algorithm 86

Table 4.2: Correlation coefficient (CC), Root Mean Square Error (RMSE) and Bais (BA) for different SCAN nodes with respect to SMOS nodes averaged over 15Km buffer (with 40% forest) fraction for S6 and S8 algorithm 87

Table 4.3: CC, RMSE and Bais for the case 1 for 80% and 40% forest fraction.....90

Table 4.4: CC, RMSE and Bais for the case 2 of 80 % and 40% forest fraction.....91

Table 4.5: CC, RMSE and Bais for the case 3 for 80% and 40% forest fraction 92

Table 4.6: CC, RMSE and Bais for all the cases for OBS and OJP sites.....94

Table 4.7: Correlation coefficient (CC) and Root Mean Square Error (RMSE) for each node of SMOS node under different forest fractions covered area with respect to the ground observed SM.....97

Table 4.8: Correlation coefficient (CC) and Root Mean Square Error (RMSE) for each node of LPRM node under different forest fractions covered area with respect to the ground observed SM.....98

Glossary

AMSR-E Advanced Microwave Scanning Radiometer - Earth Observing System

ATBD Algorithm Theoretical Baseline Document

DFFG Discrete Flexible Fine Grid

DFG Discrete Fine Grid

DGG Discrete Global Grid: the SMOS grid

ECMWF European Centre for Medium-range Weather Forecasting

ESA European Space Agency

FOV SMOS alias-free Field of View

L1c SMOS Level 1c processor or Data Products

L2 SMOS Level 2 processor or Data Products

LAI Leaf Area Index

LAI_{Max} Maximum value of the LAI over one year for a forest stand

RFI Radio Frequency Interference

RMSE Root Mean Square Error

RTE RT Radiative Transfer Equation, Radiative Transfer

SM Soil volumetric Moisture content

TEC Total Electron Content

IEEE Institute of Electrical and Electronics Engineers

TPR Total Power Radiometer

NIR Noise Injection Radiometer

TDR Time Domain Reflectometry

NP Neutron Probe

AVHRR Advanced Very High Resolution Radiometer

TRMM Tropical Rainfall Measuring Mission

T_B Brightness Temperatures

SMOS Soil Moisture and Ocean Salinity

ISEA – Grid - Inverse Snyder Icosahedral equal area projection

BSW Bound Soil Water

FSW Free Soil Water

RMDM refractive mixing dielectric model

VMC Volumetric Water Content

PI Polarization Index

WL Water Level

FWS Fractional Water Surface

1. Introduction

1.1 Basic Concepts

The Earth continuously receives electromagnetic radiation coming mainly from the Sun. Part of it is scattered and/or absorbed by the atmosphere, and the other part is transmitted to the Earth's surface. At the Earth's surface, part of this energy is absorbed, and part is scattered outwards. The energy absorbed is then transformed into thermal energy, which leads to a temperature increase until the thermodynamic equilibrium is reached. At this state, according to Thermodynamics, all media (gases, liquids, solids and plasma) radiate energy to keep the energy balance. Radiometry is the field of science that studies the thermal electromagnetic energy radiated by the bodies. Radiometers are instruments capable of measuring the power emitted by a body with high accuracy. A microwave radiometer is a passive sensor that simply measures electromagnetic energy radiated towards it from some target or area. As a passive sensor, it is related more to the classical optical and IR sensors than to radar, its companion active microwave sensor. The energy detected by a radiometer at microwave frequencies is the thermal emission from the target itself as well as thermal emission from the sky that arrives at the radiometer after reflection from the target.

The basic concepts of microwave radiometry are reviewed in this section.

1.1.1 Brightness and power collected by an antenna

Brightness, is defined as the power emitted by a source in a solid angle per unit area of the emitting surface B (θ, ϕ) [$Wsr^{-1}m^{-2}$]. Although the proper SI term for this quantity is actually radiance, but the term brightness is still commonly used in radiometry, photonics and laser work. Since the word "brightness" conveys a more intuitive understanding of its meaning than the technical term radiance, brightness is more commonly used.

Brightness depends on the source's normalized radiation pattern F_t (θ, ϕ) (power density per unit solid angle) and the total radiating area A_t.

$$B(\theta,\phi) = \frac{F_t(\theta,\phi)}{A_t} \tag{1.1}$$

Considering the case represented in Figure 1.1, where an antenna with effective area A_r and normalized radiation pattern F_n (θ, ϕ) is receiving an incident brightness coming from an extended source (such as the sky or the terrain), the total power received by the antenna is given by (Ulaby et al., 1981):

$$P = \frac{A_r}{2}\int_f^{f+\Delta f}\iint_{4\pi} B_f(\theta,\phi)F_n(\theta,\phi)d\Omega df \tag{1.2}$$

Where, B_f (θ, ϕ) is the spectral brightness, defined as the brightness per unit bandwidth df, $d\Omega$ is the differential of soil angle, and Δf is the bandwidth of the receiving antenna. The factor 1/2 accounts for the fact that thermal radiation is randomly polarized, while antennas can only collect one polarization.

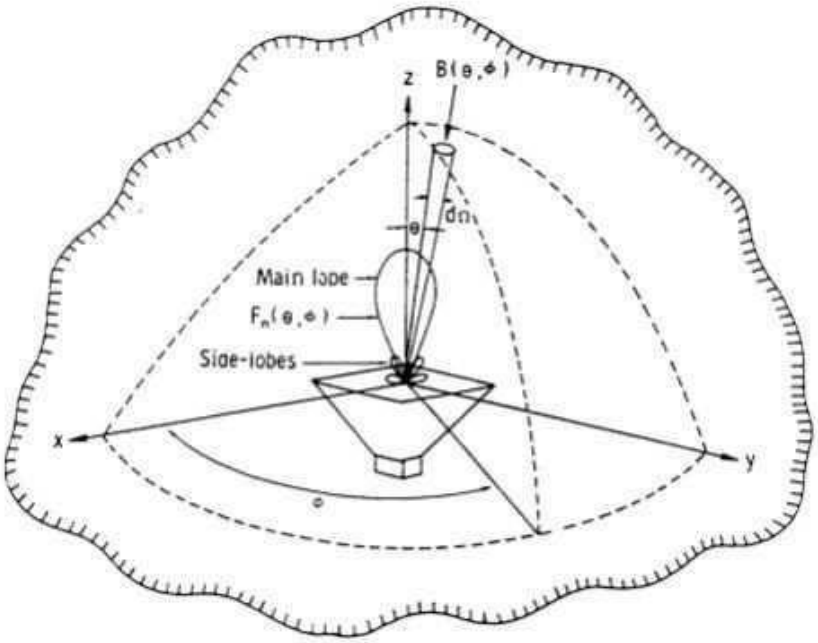

Figure 1.1 : Geometry of the incident radiation from an extended source on an antenna, from Ulaby et al. (1981)

1.1.2 Blackbody radiation

All bodies at a non-zero absolute physical temperature radiate electromagnetic energy. If the body has a definite temperature, the higher it is the higher is the total emitted radiation, and the shorter is the wavelength of maximum emission. For example, at room temperature (~300 K), bodies emit thermal radiation that is mostly infrared and invisible to the eye. At higher temperatures the amount of infrared radiation increases and can be felt as heat, and the object glows red. At extremely high temperatures, bodies are dazzlingly bright yellow or blue-white and emit significant amounts of short wavelength radiation, including ultraviolet and even x-rays. In 1901, Planck introduced the concept of a blackbody radiator in his quantum theory, which represents a reference, relative to which the radiant emittance of a material can be expressed. A blackbody is defined as an idealized, perfectly opaque material that absorbs all the incident radiation at all frequencies, without reflection. Also, a blackbody is a perfect emitter. Therefore, when a black-body reaches the thermodynamic equilibrium, it radiates all the absorbed energy omnidirectionally. The blackbody spectral brightness B_f is given by the Planck's radiation law:

$$B_f = \frac{2hf^3}{c^2}\left(\frac{1}{e^{hf/k_BT}-1}\right) \tag{1.3}$$

Where, f is the frequency in Hz, h = $6.63*10^{-34}$ J·s is the Planck's constant, k_B = $1.38*10^{23}$ J/K is the Boltzmann's constant, T is the physical temperature in K, and c = $3*10^8$ m/s is the speed of propagation.

At microwave frequencies, $hf/k_BT \ll 1$, and the Taylor's approximation

$$e^x - 1 = (1 + x + \frac{x^2}{2} + ...) - 1 \simeq x,\ for x \ll 1 \tag{1.4}$$

can be used to simplify (1.3) into a simple linear law such as:

$$B_f = \frac{2 f^2 k_B T}{c^2} = \frac{2 k_B T}{\lambda^2} \tag{1.5}$$

where λ = c/f is the wavelength. This is the Rayleigh-Jeans law, a low-frequency approximation of the Planck's radiation law. The Rayleigh-Jeans law is widely used in microwave radiometry since it is mathematically simpler than the Planck law and has a deviation error smaller than 1% for f < 117 GHz and T=300 K. A graphical comparison of the Planck law and the Rayleigh-Jeans law is provided in (Figure 1.2) for T=300 K (the Earth's temperature) and T=6000 K (the Sun's temperature).

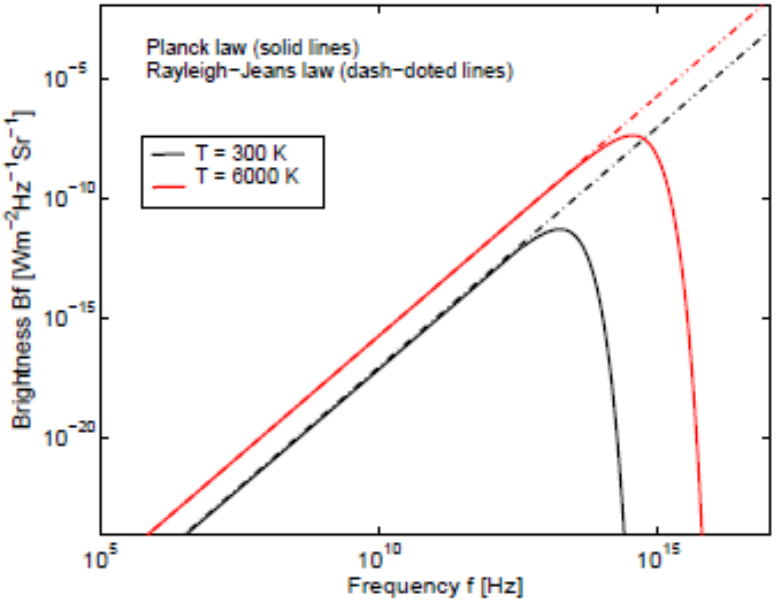

Figure 1.2: Comparison of Plank radiation law with its low-frequency approximation (Rayleigh-Jeans law) for T = 300K and T = 6000K

Hence, the brightness of a blackbody B_{bb} at a physical temperature T and a bandwidth Δf in the microwave region can be expressed as

$$B_{bb} = B_f \Delta f = \frac{2 k_B T}{\lambda^2} \Delta f \tag{1.6}$$

The power collected by an antenna with normalized radiation pattern F_n (θ, ϕ) surrounded by a blackbody at a constant physical temperature T is given by (1.2) and (1.5), and can be expressed as

$$P_{bb} = \frac{A_r}{2} \int_f^{f+\Delta f} \iint_{4\pi} \frac{2 k_B T}{\lambda^2} F_n(\theta, \phi) d\Omega df \tag{1.7}$$

The solid angle Ω is the 2-Dimension analog of the conventional 1-Dimension angle. Just as the 1-D angle is defined as the distance along a circle divided by the radius of that circle, so the solid angle Ω is analogously defined as the area on the surface of a sphere divided by the radius squared of that sphere. The unit for Ω is steradians (sr), although it should be noted that both of these measures of angle (1-D and 2-D) have no actual dimensions. Since the total surface area of a sphere is $4\pi R^2$, the total solid angle in one sphere is 4π sr.

In case of the antenna, solid angle can be expressed as a function of its effective area

$$\Omega_p = \iint_{4\pi} F_n(\theta,\phi)d\Omega = \frac{\lambda^2}{A_r} \tag{1.8}$$

Hence, assuming the system bandwidth Δf small enough so that Bf can be considered constant over the frequency range, equation (1.7), becomes

$$P_{bb} = k_B T \Delta f \tag{1.9}$$

This direct linear relationship between power and temperature is of fundamental importance in microwave remote sensing, where the power received by an antenna is commonly given in units of temperature (see Section 1.1.4).

1.1.3 Gray body radiation

A blackbody is a useful theoretical concept for describing radiation principles, but real materials or gray bodies do not behave like blackbodies: they do not absorb the entire energy incident upon them and their emission is lower than that of perfect blackbodies. It is therefore convenient to define a microwave brightness temperature $T_B(\theta, \phi)$, so that the brightness of a gray body can be expressed, similarly to equation (1.6) as,

$$B(\theta,\phi) = \frac{2k_B}{\lambda^2} T_B(\theta,\phi)\Delta f \tag{1.10}$$

$T_B(\theta, \phi)$ is the temperature that a blackbody would have to produce the observed brightness $B(\theta, \phi)$; it is not the real temperature of the object, but an effective temperature. The brightness of gray bodies relative to that of blackbodies at the same physical temperature is called the emissivity $e(\theta, \phi)$.

$$e(\theta,\phi) = \frac{B(\theta,\phi)}{B_{bb}} = \frac{T_B(\theta,\phi)}{T} \tag{1.11}$$

Note that, since real materials emit less than a blackbody, $B(\theta, \phi) \leq B_{bb}$, and therefore $0 \leq e(\theta, \phi) \leq 1$. The emissivity equals 0 in the case of a perfect reflector (e.g. a lossless metal), and 1 in the case of a perfect absorber, a blackbody. Thus, the brightness temperature $T_B(\theta, \phi)$ of a material is always smaller than, or equal to, its physical temperature T.

1.1.4 Power-temperature correspondence

In the microwave region, since the radiance emitted by an object is proportional to its physical temperature (1.5), it is convenient to express the radiance in units of temperature. Hence, the brightness temperature $T_B(\theta, \phi)$ is used to characterize the radiation of an object (equation 1.10). Similarly, an apparent temperature T_{AP} is defined to characterize the total brightness incident over a radiometer antenna $B_i(\theta, \phi)$, as

$$B_i(\theta,\phi) = \frac{2k_B}{\lambda^2} T_{AP}(\theta,\phi)\Delta f \tag{1.12}$$

Therefore, the power collected by an antenna with normalized radiation pattern $F_n(\theta, \phi)$ receiving a non-blackbody incidence brightness is given by (1.2) and (1.12),

$$P_{bb} = \frac{A_r}{2}\int_f^{f+\Delta f}\iint_{4\pi} \frac{2k_B T}{\lambda^2} T_{AP}(\theta,\phi)F_n(\theta,\phi)d\Omega df \tag{1.13}$$

It is convenient to define an antenna temperature T_A as the temperature equivalent of the power received with an antenna, so that (1.9) holds as $P = k_B T_A \Delta f$ for gray bodies. Hence, T_A can be expressed as

$$T_A = \frac{A_r}{\lambda^2}\iint_{4\pi} T_{AP}(\theta,\phi)F_n(\theta,\phi)d\Omega \tag{1.14}$$

Note that T_A includes contributions from the target being observed as well as from radiation emitted and scattered from other sources, but not from internal elements

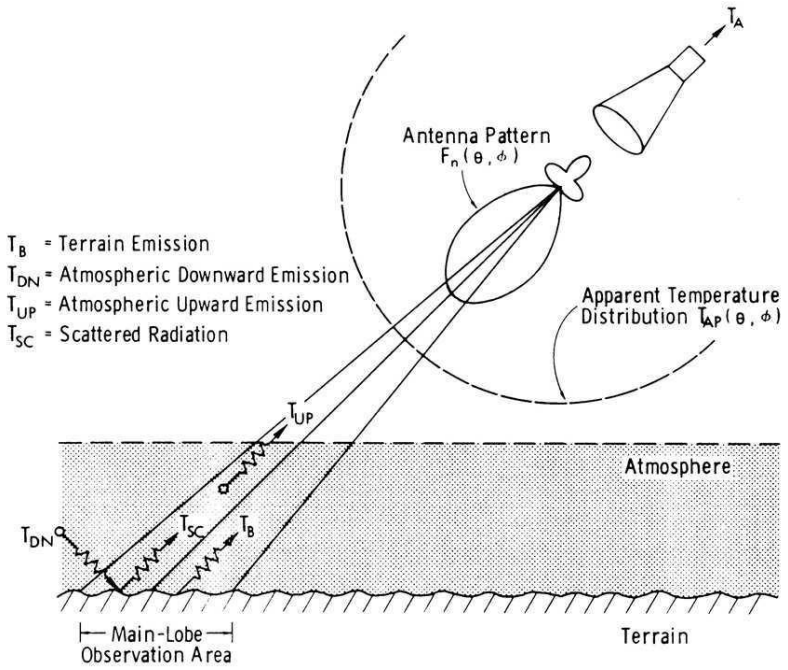

Figure 1.3: Radiation incident upon an Earth-looking radiometer. Relationship between the antenna temperature T_A, apparent temperature T_{AP} and brightness temperature T_B, from Ulaby et al. (1981).

The case of prime interest in passive remote sensing is that of an Earth-looking radiometer, as illustrated in (Figure 1.3). In this case, the radiation incident upon the antenna is a function of both the land surface and the atmosphere, and may be expressed as

$$T_{AP}(\theta,\phi) = T_{UP} + (T_S + T_{SC})\frac{1}{L_a} \tag{1.15}$$

where T_S is the brightness temperature of the land surface, T_{UP} is the atmospheric upward radiation, T_{SC} is the downward atmospheric radiation scattered by the Earth's surface in the direction of the antenna, and L_a represents the attenuation of the atmosphere. At the lower microwave frequencies used in soil moisture sensing, the atmospheric effects are small and may be safely neglected in most cases.

1.1.5 Measuring brightness temperatures from space and concerns

Space-borne radiometers are very sensitive receivers capable of measuring the radiance emitted by the Earth's surface with high accuracy. They are designed to transform the radiation collected by an antenna into mapable electric signals, and its performance is usually characterized by its radiometric resolution, accuracy, and spatial resolution (Randa 2008):

- The **radiometric resolution** (sometimes called sensitivity) is computed as the smallest change in input brightness temperature or radiance that can be detected in the system output.

- The **radiometric accuracy** represents the closeness of the agreement between the measured antenna temperature and its true value (systematic error). Because the true value cannot be determined exactly, the measured or calculated value of highest available accuracy is typically taken to be the true value.

- The **spatial resolution** is the ability of the sensor to separate two closely spaced identical point sources.

In a remote sensing mission, in addition to instrumental errors, other phenomena can degrade the radiometric resolution and must be corrected (compensated for). At lower frequencies, the atmosphere is almost transparent, and the main error sources are the Faraday rotation and the space radiation, which are described hereafter.

1.1.5.1 The atmosphere:

The atmosphere plays an obvious crucial role in Earth observation from space, since the electromagnetic field has to cross it. The damping of the field caused by the atmosphere affects the performance of the observing systems. Atmospheric attenuation caused by absorption from the constituent gases is strongly dependent on the frequency. The atmosphere essentially consists of nitrogen (78.1%) and oxygen (20.9%), a small amount of water vapor and minor quantities of other gases(carbon dioxide, methane, ozone etc.). Because of the low activity of nitrogen, permittivity of the atmosphere mainly results from the polarization of the other molecule species of which water vapor, being polar, is particularly active. At radio frequency (i.e., microwave), main interactive gases are oxygen and especially water vapor, which determine the dominant trend with frequency of real and imaginary parts of atmospheric permittivity. As indicated by the diagram in Figure 1.4, the overall attenuation by absorption show peaks at the resonance frequencies of water vapor and oxygen.

In general, many materials change their spatial arrangement of charges according to different configurations, resulting in different permittivity patterns, in particular in resonances at different frequencies, since involved charges, masses, frictional and restoring forces differ according to the deformation modes. A number of resonances are exhibited by materials, generally related to their complex and microscopic structure. The resonance frequencies and corresponding values of permittivity are actually related to transitions between vibrational and electronic energy levels.

In general, an increasing trend of attenuation as a function of frequency is observed. It indeed, exalts in the thermal range, which is the spectral regions at which rotational and vibrational resonances of atmospheric species are more numerous, so that the atmosphere is practically opaque. Low absorption is found again in the visible, which, together with the microwave, is the main transparent band at which the Earth observing systems operate (Solimini 2013) .

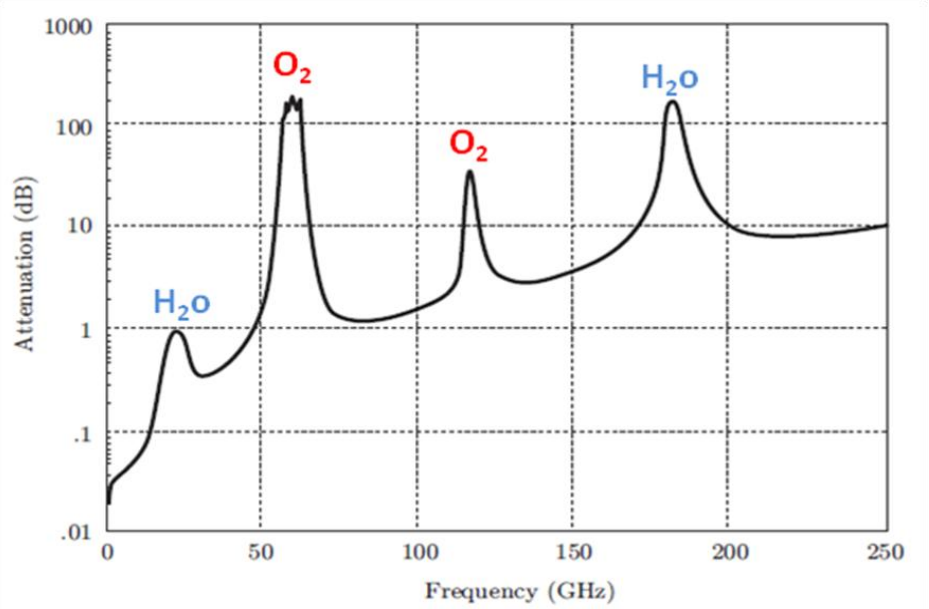

Figure 1.4: Atmospheric attenuation by absorption at different frequencies (Solimini 2013)

1.1.5.2 Electromagnetic Interferences

Radio Frequency Interference (RFI) in passive microwave remote sensing occurs due to the anthropogenic (man-made) signals, which contaminate calibrated radiometric brightness temperature measurements of naturally occurring background thermal radiation, resulting in anomalous measurements. The Noise levels generated due to the contamination are frequently sufficient to saturate the total power channel. RFI is a serious concern for future passive remote sensing missions in space. This is especially true for synthetic aperture radiometers because they employ small antennas with a wide field-of-view.

1.1.5.3 Faraday Rotation

When propagating through the ionosphere, a linearly polarized wave undergoes a progressive rotation of its plane of polarization due to the presence of the geomagnetic field and the anisotropy of the plasma medium (P.531-6 et al. 2001). This phenomena is known as Faraday rotation, which may be expressed as

$$\varphi = 2.36*10^{-14} B_{av} N_T f^{-2} \quad (1.16)$$

where φ [rad] is the rotation angle, f [GHz] is the frequency, N_T [electrons/m^2] is the ionospheric total electron content (TEC), and B_{av} [Wb/m^2] is the average Earth's magnetic field along the propagation path.

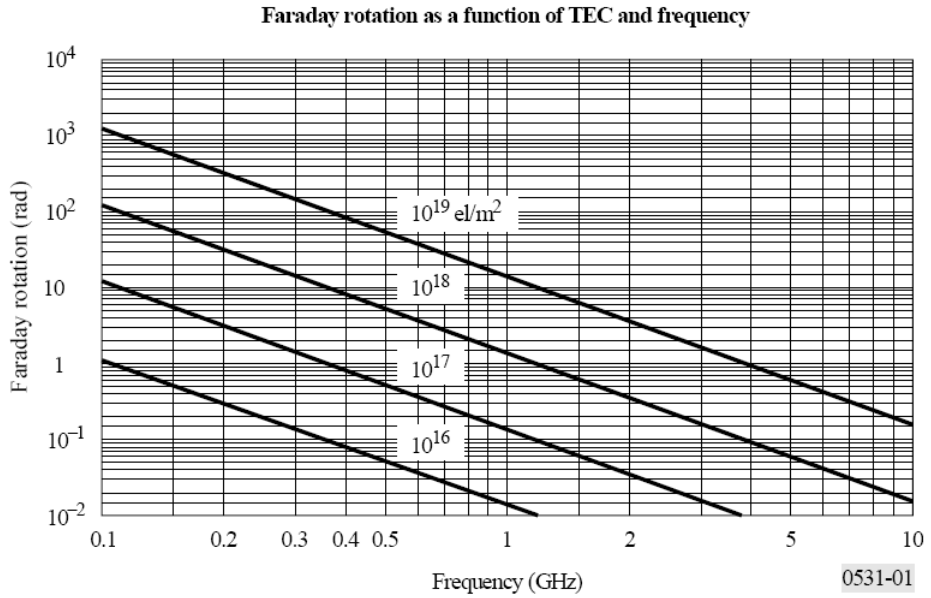

Figure 1.5:Typical values of Faraday rotation angle as a function of TEC and frequency, from(P.531-6 et al. 2001)

Figure 1.5 shows typical values of the Faraday rotation angle as a function of TEC and frequency. TEC is significantly affected by the solar radiation, and shows significant temporal and latitudinal variations; assuming low latitudes, the Faraday rotation angle at 1.4 GHz can be as low as 4^0 at night (TEC of 10^{16} electrons/m^2) and as high as 30^0 at noon (TEC of 10^{18} electrons/m2). This rotation may result in errors on the brightness temperatures of 1-10 K, which is sufficient to cause errors in the retrieval of the surface parameters (Yueh 2000). As it will be seen, an effective way to avoid this problem is to use the first Stokes parameter, which is invariant to rotations. See the Stokes parameters will be defined in Section 1.1.6. Fully polarimetric measurements are also useful since make it possible a compensation of the effect.

1.1.5.4 Space radiation

Microwave radiation from space reflects over the Earth's surface and is also received by the antenna. Three main space phenomena should be considered, and their contribution to the antenna temperature needs to be taken into account:

• The **cosmic radiation level**: It is fairly constant and low (~2.7 K) and, therefore, it does not significantly affect the quality of measurements.

• The **galactic noise**: It comes from the reflection over the Earth's surface of the pole or the center of the galaxy, and varies from 0.8 K to 40 K at 1.4 GHz (LeVine and Abraham 2002). It should be either avoided, by selecting a convenient orbit, or corrected through the use of existing galactic noise maps. However, the absolute accuracy of these maps is still questionable and the scattering models present errors.

• **Sun glint**: It is the most important noise source, the Sun brightness temperature value is higher than 100,000 K, and any reflection of Sun radiation collected by the antenna would seriously affect

measurements. Hence, direct reflections should be avoided by pointing the instrument to the shadow zone of a polar sun-synchronous orbit.

1.1.6 Polarization and Stokes parameters

The received field of an antenna is composed of electric and magnetic lines of forces. These lines of forces are always at right angle to each other. The electric field determines the direction of polarization of the wave.

The polarization of an electromagnetic wave can be completely described by the four Stokes parameters I, Q, U, V. The first Stokes parameter (I) describes the total intensity of electromagnetic emission and the second Stokes parameter (Q) is the difference between the intensity in two orthogonal directions in a given polarization frame, i.e. vertical and horizontal polarizations. The third (U) and fourth (V) Stokes parameters, respectively, represent the real and imaginary parts of the cross-correlation between these orthogonal polarizations (Randa 2008)

$$\begin{aligned} I &= \frac{\left\langle |E_v|^2 \right\rangle + \left\langle |E_h|^2 \right\rangle}{\eta_0}, \\ Q &= \frac{\left\langle |E_v|^2 \right\rangle + \left\langle |E_h|^2 \right\rangle}{\eta_0}, \\ U &= \frac{2R_e \left\langle E_v E_h^* \right\rangle}{\eta_0}, \\ V &= \frac{2I_m \left\langle E_v E_h^* \right\rangle}{\eta_0}, \end{aligned} \tag{1.17}$$

Where, E_v and E_h are the electric field components at vertical and horizontal polarizations, respectively, and η_o is the electromagnetic wave impedance of the medium ($120\pi\ \Omega$ in vacuum). In polarimetric remote sensing radiometry the Stokes parameters are conventionally expressed in terms of brightness temperature

$$\begin{aligned} T_I &= T_v + T_h = \frac{\lambda^2}{k_B.B_w}.I, \\ T_Q &= T_v - T_h = \frac{\lambda^2}{k_B.B_w}.Q, \\ T_U &= T_{45} - T_{-45} = \frac{\lambda^2}{k_B.B_w}.U, \\ T_V &= T_{lc} - T_{rc} = \frac{\lambda^2}{k_B.B_w}.V, \end{aligned} \tag{1.18}$$

where λ is the wavelength, and B_w is the noise-equivalent bandwidth. T_v and T_h are the vertical and horizontal brightness temperatures, T_{45} and T_{-45} represent orthogonal measurements skewed ±45◦ with respect to normal, and T_{lc} and T_{rc} refer to left-hand and right-hand circular polarized quantities.

Generally, the energy emitted from the Earth's surface is partly polarized, meaning that the vertical brightness temperature is different from the horizontal. Whereas conventional dual-polarization radiometers only measure vertical and horizontal polarized brightness temperatures, a polarimetric radiometer is capable of directly or indirectly measuring all four Stokes parameters, which provides a full characterization of the polarization properties of the emitted energy. Note that the Faraday rotation ϕ mixes the polarization as follows

$$\begin{aligned} E_v^{Faraday} &= E_v \cos\varphi + E_h \sin\varphi, \\ E_h^{Faraday} &= -E_v \sin\varphi + E_h \cos\varphi \end{aligned} \tag{1.19}$$

Hence, the first and fourth Stokes parameter are invariant to rotations, whereas the second and third Stokes parameter are not. In remote sensing, third and fourth Stokes parameters are primarily used for correcting polarization rotation (Yueh et al. 1995), (Mart´ın-Neira et al. 2002) or, in the case of the ocean for instance, to infer wind direction information (Brown et al. 2006).

1.1.7 Microwave electromagnetic spectrum

Electromagnetic waves are originator and carrier of information in earth observation. The information content of products delivered by a given type of system is essentially related to electromagnetic parameters (mainly frequency/ wavelength) and to the properties of the observed medium. . Frequency or wavelength of operation is mainly selected considering the kind, intensity and effectiveness of the interaction with the material to be observed and on the transmission of the atmosphere interposed between the sensor and the observed object. The wave interacts with different variety of materials, including natural or man-made solid, liquid and gaseous media. Because of the variety of obtainable information and the exploitability of various atmospheric windows, the portion of the electromagnetic spectrum over which the earth observation missions operate is wide, from low microwave frequency to the ultraviolet wavelengths. The choice of sensor, of frequency band is essentially driven by the kind of object user wish to observe and the type of parameters to be retrieved.

Microwaves are waves with wavelengths ranging from about one meter to about one millimeter, or equivalently, with frequencies between 300 MHz (0.3 GHz) and 300 GHz. The microwave spectrum is subdivided into bans, according to the IEEE definitions recalled in (Table 1.1)

Table 1.1: Microwave Electromagnetic Spectrum

IEEE Band	Frequency range (GHz)
P (UHF)	0.3 – 1.0
L	1.0 – 2.0
S	2.0 – 4.0
C	4.0 – 8.0
X	8.0 – 12.0
Ku	12.0 – 18.0
K	18.0 – 27.0
Ka	27.0 – 40.0

1.1.8 Microwave Radiometers

A radiometer is a receiver that measures the electromagnetic radiation emitted by an object in a given frequency band. This radiation, being basically thermal noise, has generally very low power.

1.1.8.1 Real Aperture Radiometers

Real aperture radiometers scan across the field of view to measure the T_B. Moreover, if they are flying at a height h the antenna size D required for a footprint d is D = ¸λh/d. For low-Earth orbit satellites operating at L-band, such as SMOS, an adequate ground resolution using real aperture radiometer implies an antenna size of several metres. This is impossible to implement for in-orbit sensors, but these radiometers are still being used (AMSR-E). The configurations and main characteristics of real aperture radiometers are briefly described hereafter. Further information may be found in ((Skou 1989) and (Ulaby et al. 1986b).

1.1.8.1.1 The Total Power Radiometer

The TPR is the simplest type of radiometer; Its block diagram is shown in Figure 1.6, on the left the functional blocks are shown, while the measured voltage and the signal spectrum are plotted in the center and on the right, respectively. The output

$$V_{0ut} = k\Delta f G(T_A + T_N) \tag{1.20}$$

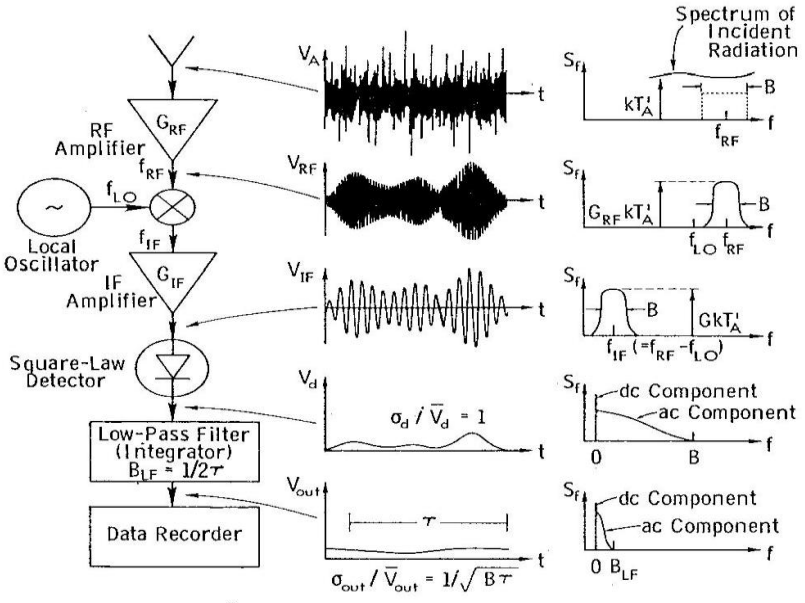

Figure 1.6: A Total Power radiometer block diagram. from (Ulaby et al. 1982)

is dependent on the radiometer gain *G* and noise temperature T_N. Gain variations are inherent to the performance of both gain and lossy microwave component, so TPR are not stable enough unless frequent calibrations are performed. The sensitivity of these radiometers is given by

$$\Delta T = \frac{T_A + T_N}{\sqrt{\Delta f \, \tau_r}} \tag{1.21}$$

being τ_r the integration time. It is the maximum than can be achieved if gain variations are neglected.

1.1.8.1.2 Dicke radiometer

The Dicke radiometer was proposed to solve the stability problems of total power radiometers. A Dicke radiometer views the scene during half the cycle and a matched load during the other half of the cycle. In this case, instead of the antenna temperature the difference between the antenna temperature and a known reference value T_R is measured:

$$V_{out} = c(T_A - T_R)G \tag{1.22}$$

Note that this radiometer is more stable than TPR since the output does not depend on T_N and the weight of G can be diminished by choosing T_R values in the range of T_N. However, neglecting the gain fluctuations, the sensitivity of this configuration is:

$$\Delta T = 2\frac{T_A + T_R}{\sqrt{\Delta f \, \tau_r}} \tag{1.23}$$

It is degraded by a factor of 2 as compared to total power radiometers. The 2 factor arises from the fact that the scene is measured only half of the time.

1.1.8.1.3 Noise Injection radiometer

Noise injection radiometers (NIR) are a modification of Dicke radiometers to obtain an output independent of G and T_N. As shown in Figure 1.7, the configuration uses as input to the Dicke radiometer the signal $T_{0A} = T_A + T_I = (T_R - T_I) + T_I = T_R$, where T_I is a variable noise temperature. Since T_{0A} has the same value as T_R, then the radiometer output is zero:

$$V_{out} = c(T_A^{'} - T_R)G = 0 \tag{1.24}$$

The sensitivity of noise injection radiometers is given by:

$$\Delta T = 2\frac{T_R + T_N}{\sqrt{\Delta f \, \tau_r}} \tag{1.25}$$

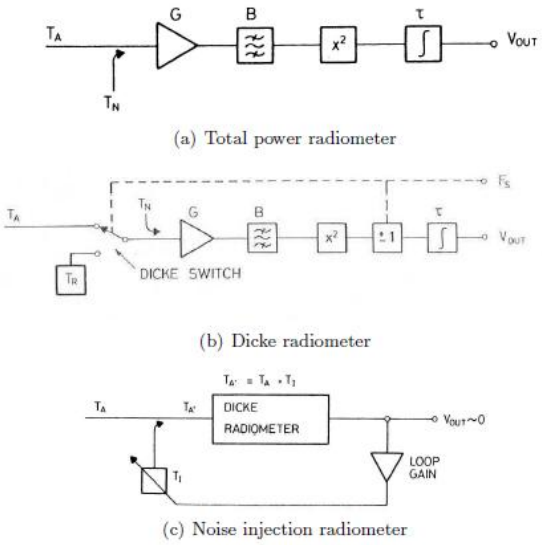

Figure 1.7: (a) total power, (b) Dicke, and (c) noise injection radiometer schematic (Skou 1989)

1.1.8.2 Synthetic Aperture Radiometers

Synthetic aperture technology was proposed to solve the antenna size problem of real aperture radiometers commented on the previous section (LeVine and Good 1983). The basic concept of interferometric radiometry is to synthesize a large aperture using a number of small antennas. A two-dimensional image of the observed scenario is obtained by the cross-correlation of every pair of antenna having an overlapping field of view. The output voltages of a pair of antennas (e.g. located at (X_1, Y_1) and (X_2, Y_2)) are cross-correlated to obtain the so- called “visibility samples", as expressed by the following equation

$$V(u,v) = \frac{1}{k_B\sqrt{B_1 B_2}\sqrt{G_1 G_2}}\frac{1}{2}\left\langle b_1(t)b_2^*(t)\right\rangle \tag{1.26}$$

where u and v are the spatial frequencies of visibility sample: (u, v) = (X_2 - X_1, Y_2 - Y_1) / λ = (Δx, Δy) / λ, k_B is the Boltzmann constant, B_1 and B_2 the receivers' noise bandwidths, G_1 and G_2 the avail- able power gains, $b_1(t)$ and $b_2(t)$ the complex signals measured by elements 1 and 2, respectively, and * is the complex conjugate operation. The complete set of the visibility samples is called a visibility map, and it is approximately the Fourier transform of the brightness temperature distribution of the scene.

To invert this process the inverse Fourier transform can be applied as a first approximation (Camps et al. 1997) or a more sophisticated G-matrix inversion (Anterrieu and Camps 2008), (Camps et al. 2008a)can be used. The result is a potential degradation of the radiometric sensitivity in terms of a higher rms noise, on the other hand a complete image is acquired in one snapshot, permitting to increase the integration time and improve the measurement sensitivity. Nevertheless, a further advantage of interferometric radiometry can be the multi-angular measurement: the output of an IFR is, in fact, an image; this permits having several views under different incidence angles of the same point on the Earth before it exits from the Field of View. For these reasons, interferometric radiometry has been preferred by ESA over real aperture radiometers, leading to the design and implementation of the MIRAS instrument aboard the SMOS mission. Details can be found in SMOS mission section (1.4.2). Further information may be found in (Camps 1996).

1.2 Applications

1.2.1 Soil Moisture Monitoring

Soil moisture patterns, both spatial and temporal, are the key to understand the spatial variability and scale problems that are of paramount importance in scientific hydrological, meteorological and climatological studies. Soil moisture not only controls the ratio of runoff and infiltration (Delworth and Manabe 1988; Wagner et al. 2003), decides the energy fluxes (Entekhabi and Rodriguez-Iturbe 1996; Prigent et al. 2005) but also influences vegetation development and through that the carbon cycle. It controls the exchange of water and heat energy between the land surface and the atmosphere through evaporation and plant transpiration. As a result, soil moisture plays an important role in the development of weather patterns and the production of precipitation. Simulations with numerical weather prediction models have shown that improved characterization of surface soil moisture, vegetation, and temperature can lead to significant forecast improvements. Soil moisture also strongly affects the amount of precipitation that runs off into nearby streams and rivers.

A long term soil moisture data set on a region scale therefore could provide valuable information for researches such as climate change and global warming (Seneviratne et al. 2006), and also improve the weather forecasting (Beljaars et al. 1996; Schar et al. 1999) and water resources management in more methodical manner.

Understanding of soil moisture is different in different disciplines. Soil Moisture for a farmer is different from that of a water resource manager or a weather forecaster. Generally, soil moisture is the water that is held in the spaces between soil particles. Usually surface soil moisture is the water that is in the upper 10 cm of soil, whereas root zone soil moisture is the water that is available to plants, which is generally considered to be in the upper 200 cm of soil.

Soil moisture profile can be observed at point scale by using gravimetric sampling or some automatic probes, such as Time Domain Reflectometry (TDR), Neutron Probe (NP), etc. These methods are commonly used to provide accurate and continuous soil moisture information and adopted by the meteorology, hydrology and agriculture stations. But these point information are not enough for the regional research and application, and are also not available in the remote areas where it is difficult to access and to maintain such stations. On the other hand, satellite remote sensing offers a possibility to measure surface soil moisture at regional, continental and even global scales.

Remote sensing of soil moisture from the vantage point of space is advantageous because of its spatial coverage and temporal continuity. Research in soil moisture remote sensing began in the mid 1970's shortly after the surge in satellite development. Although surface soil moisture can be estimated indirectly from visible/infrared remote sensing data (Verstraeten et al. 2006), it failed to produce routinely soil moisture map mainly due to factors inherent in optical remote sensing, such as atmosphere effects, cloud masking effects and vegetation cover masking effects. Subsequent research has occurred along many diverse paths. In general, quantitative measurements of soil moisture in the surface layer of soil have been most successful using passive remote sensing in the microwave region. It is so because, microwave remote sensing offers a possibility to observe area-averaged surface soil moisture regularly in the global scale, by directly measuring to the soil dielectric properties which are strongly related to the liquid moisture content (Hipp 1974).Moreover, extra advantages of microwave remote sensing include: (1) long wavelength in microwave region which enable the low frequency microwave signals to penetrate clouds

and to provide physical information of the land surface; and (2) independent of illumination source which enables the spaceborne sensors to observe earth all-day with all-weather coverage.

Many studies have shown the success of using passive microwave remote sensors to monitor surface soil moisture over land surfaces (Eagleman and Lin 1976; Ulaby et al. 1986b and Schmugge et al. 1994). As the moisture increases, the dielectric constant of the soil-water mixture increases and this change is detectable by microwave sensors (Njoku and Kong 1977). These sensors measure the intensity of microwave emission from the soil, which is proportional to the brightness temperature, a product of the surface temperature and emissivity. This observed emission is related to its moisture content, due to the large differences in the dielectric constant of dry soil and water (Moran et al. 2004)

Soil moisture remote sensing is fraught with challenges. Only the moisture in the top few centimeters of soil can be detected. Algorithm development is complicated by the need for surface roughness and vegetation corrections, which are based on empirical and model based relationships, but still of limited breadth. Extending ground-based techniques to space-based systems requires innovative antenna technology. In spite of these challenges, recent advances in aperture synthesis and thinned array technology applied at L band (section 1.4.2) have shown great promise for soil moisture mapping. The potential exists today to retrieve soil moisture estimates from space-based instruments at frequencies ranging from 36 GHz (Ka band) to the observations at frequencies between 1 and 3 GHz (L band) for detection of soil moisture from a deeper soil layer, even in presence vegetation.

1.2.2 Floods and Methods of its monitoring:

Flood is a natural event that can have far reaching effects on people and the environment. A sketch of flooding process is illustrated in Figure 1.8. It is an accumulation of too much water in too little time in an area where the land is normally dry. Floods are extremely common all over the world (they are the most common and widespread natural disaster except for fire), and are caused by a variety of reasons.. In some equatorial countries (viz., Bangladesh and India), the monsoon rains can cause bad flooding because the rain comes down fairly steadily for a long period of time. The water level in a certain area can rise extremely fast or slow, but generally, they develop over several days. Floods are most common near water, downstream from a dam, or in land that has a low elevation. There can exist regional floods, flash floods, ice-jam floods, storm surge floods, and debris landslide and mudflow floods.

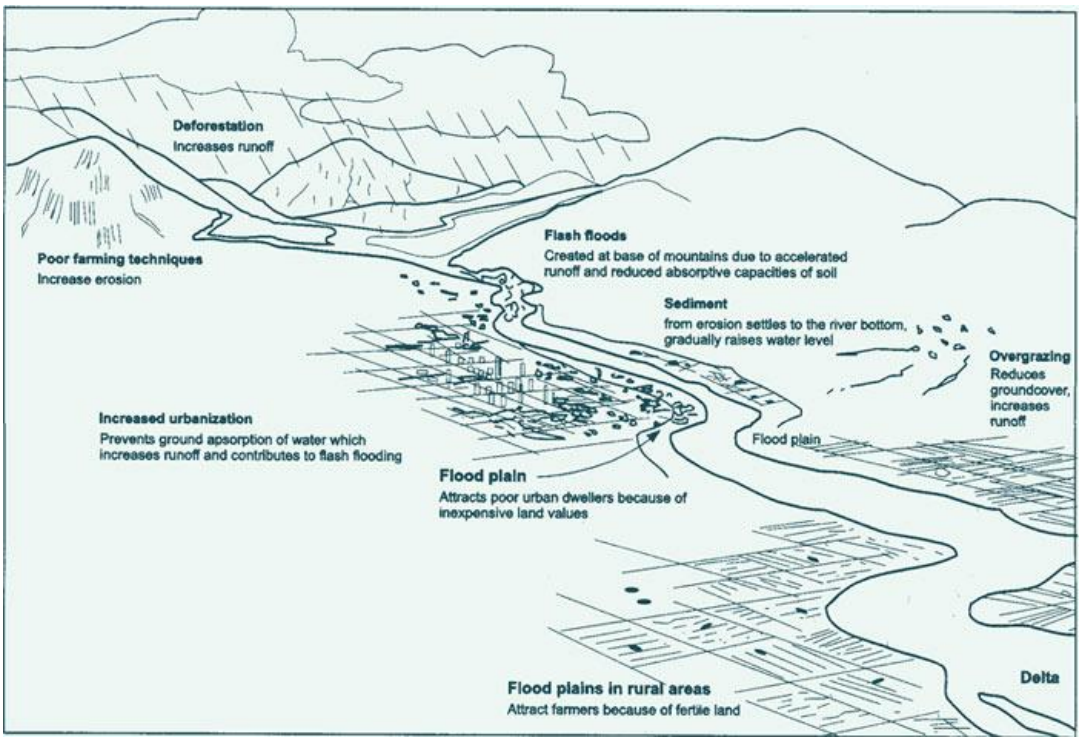

Figure1.8: Cause of floods (http://drace-project.org/index.php/floods/human factor)

Regional floods usually occur seasonally; rain from the winter and spring added to the melting snow fill the river basins with more water than they can hold and the banks overflow. If the ground is still frozen, less water can be absorbed into the soil, which increases the runoff. Long periods of time with excessive rain can also contribute to create a regional flood because all the rain saturates the soil so that any more that is accumulated runs into streams and rivers, and overflows the banks. Slow-moving, low pressure or frontal storm systems like hurricanes that are dying off, and tropical storms can contribute to create a regional flood.

Flashfloods can occur with very little, or no warning and they can easily become very strong in minutes. Large amounts of rain falling on a particular area in a short period of time is the main factor than triggers a flashflood, but characteristics like surface conditions, topography, and the slope of the land can make a

flashflood more likely in a certain area. Urban areas have a larger risk than other places because streets, roofs, and parking lots are a good place for water to runoff and gather. Mountainous areas also have a larger risk because the ground has a steep slope, and runoff water can go into a narrow canyon, and then the canyon can overflow. If you are standing below a flashflood when it starts, it will look like a wall of water is descending upon you.

Ice jam floods occur on rivers that are at least partially frozen. If the water level rises, the ice will break up and then pile together in shallow places to block other things that might be coming downstream, like logs. The combination of the ice, logs, and other debris will block the river and keep the water from flowing by. Eventually the natural dam will break and the water behind it will be released. With all this water being released at the same time, the flood becomes a flashflood with large ice chunks in it that can badly hurt people or other objects.

Storm surge flooding is caused by water pushed up on land that is usually dry by a storm surge. Dam and Levee (An embankment raised to prevent a river from overflowing) failure floods occur if more water piles up behind the dam or levee than the structure is built to hold. The water will spill over the dam, and most likely, the force of the water will break the dam, letting all the water inside pour out. In this case, the flood becomes a flash flood. Debris and landslide floods are created when debris, mud, rocks and maybe logs pile up over a river and form a temporary dam. As the water gathers behind the debris, a flood begins, and when the dam breaks and the water is released, it becomes a flashflood.

The use of remote sensing within the domain of natural hazards and disasters has become increasingly common, due in part to increased awareness of environmental issues such as climate change, but also to the increase in geospatial technologies and the ability to provide up-to-date imagery to the public through the media and internet. They enable the collection and monitoring of data about atmospheric conditions and characteristics of the Earth's surface leading to processes, which may bring about floods. Such information can be used to help determine appropriate actions to reduce the disastrous effects of these processes. It has been demonstrated that using satellite data for flood mapping becomes economically advantageous with respect to ground survey for areas larger than a couple of ten square kilometers.

Since the year 2000 there have been a number of space borne satellites and sensors that have changed the approach to managing the natural disasters. The increase in the satellite data acquisition rates, sensor resolution, improvement of change detection algorithms and integration of remote sensing systems has significantly improved the real-time assessment and management of natural hazards (Gillespie et al. 2007).

Earth observation satellite systems provide a high degree of detail and a wealth of information at a global level for early warning activities. This information includes two categories of data: first, numerical values of detected geophysical parameters or related measurements, and second, imaging data sensed in various electromagnetic bands. Many different space systems, with different characteristics related to Spatial distribution, Spatial resolution, Temporal resolution, Spectral resolution and Radiometric resolution, provide valuable data.

Both optical/infrared and microwave remote sensing instruments have been used for mapping surface water through time. Optical imagery operates in the visible portion of the wavelength spectrum, but also includes the infrared and thermal regions. Microwave imagery operates in the longer wavelengths from less than a centimeter up to a meter (or frequencies from 89 GHz to 0.3 GHz respectively).

Different wavelengths have different responses to water in the landscape. Much of the literature shows that for optical imagery the infrared wavelength, particularly around 1.5-1.7 micrometers performs well

for separating water from land (Overton et al. 2006) Instruments such as Landsat have a relatively high spatial resolution (30m pixels) allowing for the detection of fine water bodies. However such imagery is not routinely collected on a global scale through time, making regular monitoring of flooding events difficult.

Instruments such as the Advanced Very High Resolution Radiometer (AVHRR) and the more recent MODIS do collect data at daily/sub-daily intervals. Even with a poorer spatial resolution (1 km pixels), the AVHRR has been used to map water with reasonable success (Tanaka et al. 2003). The utility of AVHRR sensor was also realized by (Sandholt et al. 2003), who state that although the spatial resolution is coarser than many other satellite sensors the frequent revisit time offers a greater probability of obtaining cloud-free imagery. They used linear spectral unmixing with thermal imagery to determine inundated areas, but were faced with the difficulty of selecting pure end members. Alternatively, they also tested supervised maximum likelihood and ISODATA clustering classifications with the higher spatial resolution Landsat ETM+, concluding that no technique is necessarily better than the other, rather that each has its advantages and disadvantages depending on the flooding extent, cloud cover and temporal variability. The MODIS sensors have a higher spatial resolution ranging from 250m up to 1km with a twice daily overpass through much of the world, which has also been used to map surface water (Sakamoto et al. 2007). Potentially one of the most useful studies for rapid-response flood mapping was conducted to create on-board satellite processing algorithms for Hyperion imagery (Ip et al. 2006). The algorithm utilizes three narrow spectral bands for a classification and is then compared to a base scene to extract flood detail rather than just wet regions (eg, rivers, lakes). However, Hyperion has limited global coverage, and obtains imagery in relatively small segments that would be useful for localized flooding but not necessarily large events.

The extreme flooding events associated with several tropical storms in recent years (Hurricane Katrina, Cyclone Nargis) have been successfully and rapidly mapped using a variety of sensors to take advantage of differences in spatial and temporal resolution. Geoscience Australia is actively acquiring imagery of flooding events in Australia and attempting to develop semi-automated techniques for extracting inundated areas (Lymburner et al. 2008 and Thankappan et al. 2008)]. Flooding events of 2007 and 2008 were successfully mapped using Landsat-5 TM and ALOS AVNIR-2.

A major disadvantage in using optical imagery for flood mapping is that flood events are often associated with cloud cover. This is the main reason that scientists across the world started exploring microwave sensors for their potential to map surface water. For the active microwave case, the overall backscattering coefficient is essentially influenced by three processes: surface direct contribution, vegetation contribution and surface-vegetation double bounce. At lower frequencies (L, C and X Band) and angles higher than about 300, the three contributions behave and interact in a complex way. Surface backscattering increases with moisture and roughness. Vegetation attenuates surface backscattering and produces its own contribution, as well as double bounce. Flooding reduces the surface contribution, due to the decrease of roughness, and increases the double bounce effect in vegetated areas. At C Band, the overall effect produced by a moderate flooding is an increase of the backscattering coefficient due to an increase of the double bounce contribution. However, if the increase of water level submerges most of the vegetation cover, the overall effect is a decrease of backscattering coefficient. Therefore, the trend of the backscattering coefficient as a function of water level is not monotonic. These properties have been investigated for some cases of agricultural and natural vegetation, mostly at C and X Band, also with the aid of models (Le Toan et al. 1989; Caizzone et al. 2009 and Grings et al. 2005) The increase of the backscattering coefficient during flooding, related to double bounce, was detected also in forest cover areas, using L Band signatures (Wang et al. 1995) Synthetic Aperture Radar sensors have proven useful in mapping floods since the backscatter signature of water is so distinctive compared with that of vegetation (Alsdorf et al. 2007 and Lewis et al. 1998) but they are not routinely available at regional scales. (Smith

1997) suggested the use of Multi-frequency polarimetric SAR to classify different types of inundated terrain to an extent not possible with single-frequency SARs and visible/infrared sensors.

The use of passive microwave remote sensing data to monitor soil moisture, vegetation and in turn the flood events, has been the subject of several studies in recent decades. Passive microwave sensors acquire data at a high temporal frequency (1-2 times daily) on a near-global scale in comparison to active sensors. Several theoretical and experimental investigations has proved the sensitivity of passive microwave remote sensing measurements to soil and vegetation properties from the physical perspective. Researchers tried to exploit the polarization effect on the emissivity on different surfaces. For bare soil, the emissivity at vertical (V) polarization is higher than the one at horizontal (H) polarization. An increase of soil moisture produces a decrease of emissivity at both polarizations, and at all microwave frequencies. However, the effect is more important at H polarization and at the lower frequencies (Ulaby et al. 1986a; Paloscia et al. 1993; Kerr and Njoku 1990). On the other hand, a decrease of roughness produces effects which are similar to the ones produced by an increase of moisture. If the soil becomes smoother, a decrease of emissivity, which is more evident at polarization and at lower frequencies, is observed (Paloscia et al. 1993). In the presence of flooding events and/or strong rainstorms, the two effects can couple together to reduce the emissivity, since the soil becomes wet and smoother at the same time. Though on average, the vegetation growth produces a decrease of the difference between vertically polarized and horizontally polarized emission. Studies were also aimed at singling out vegetation effects from soil effects and it was found that the polarization difference at high frequencies (Ka band) was mostly related to vegetation emission, and showed a good correlation with vegetation indexes derived by optical instruments (Choudhury and Tucker 1987) further studies adopted lower frequencies, typically X band In order to eliminate the dependence on surface temperature, a normalized polarization index (Paloscia and Pampaloni 1988) was defined (details mentioned in section). A further parametric study, carried out by means of a discrete physical model, confirmed the main finding of experimental studies and pointed out that the same polarization index is also sensitive to soil moisture, at least at frequencies lower than 10 GHz (Ferrazzoli et al. 1992). In (Choudhury 1989), the absolute polarization difference at 37 GHz proved to be correlated to vegetation density and was sensitive to flooding effects occurred in the Amazon River. This last application was further exploited in (Sippel et al. 1994 and Sippel et al. 1998) and (Hamilton et al. 2002). A simple algorithm, based on the polarization difference at 37 GHz measured by SMMR, was adopted to estimate the fraction of flooded area during several events occurred in the Amazon river and in other large South American rivers floodplains.

The availability AMSR-E signatures offered new opportunities (Kawanishi et al. 2003) to understand soil moisture at different frequencies. This sensor spans a wide range of frequencies, from 6.925 GHz to 89.0 GHz, and the spatial resolution is substantially improved with respect to previous ones (details in section 1.4.1). Based on AMSR-E data, useful algorithms have been developed to retrieve soil moisture (Njoku et al. 2003 and Paloscia et al. 2006) and vegetation variables (Njoku and Chan 2006). In more recent studies, (Ferrazzoli et al. 2010) found that increase in the water level are associated with the increase in the polarization index. (Singh et al. 2012; Singh et al. 2012a and Singh et al. 2013) also found that At the X band, the water level was better correlated with the PI than with emissivity and fractional water surface. The correlation was good in cases of slow variation in WL. In cases of sudden variation in the river, the PI followed the variations with some time delay related to the propagation of water within the covered AMSR-E pixel.

One of the large challenges in using passive microwave to map surface water is its large spatial footprint (5km up to 70km). Mixed pixel analysis is often used to determine the proportion of water within each flooded pixel based on theoretical or empirical estimates of the proportion of wet and dry surfaces (Mialon et al. 2005). Daily river stage or discharge has been correlated to inundation area as derived from regularly acquired remote sensing imagery. Even without ground data, these correlations can still show the shape and timing of seasonal hydrographs, and with ground measurements the absolute discharge can

be estimated to within a factor of two (Smith 1997). For microwave data, (Choudhury 1989) achieved a linear correlation of R =0.8 while (Brakenridge et al. 2007a) used a fourth order polynomial with an AMSR-E 36.5 GHz horizontal ratio achieving good results. (Sippel et al. 1998) found mapped flooded area was correlated with river stage, using it to develop a predictive relationship for inundation patterns with historical stage records. Work by (Bindlish 2009) also demonstrated the role of passive microwave data for flood forecasting. Most of the work, however, has demonstrated the increased skill in runoff/rainfall partition modeling by using remotely sensed surface soil moisture (Pauwels et al. 2002; Jacobs et al. 2003 and Crow et al. 2005) as a tool for flood monitoring and assessment instead of for forecasting (Alsdorf et al. 2000; Brivio et al. 2002; Freeman et al. 2002 and Scofield et al. 1994). Making the transition between monitoring and forecasting requires direct observations of the hydrologic precursors to flooding events (e.g., elevated soil moisture conditions) and not simply the manifestation of the flood itself.

Many researchers also worked to combine of various data sources (optical, active and passive microwave data) for flood mapping. (Ticehurst et al. 2009) developed different ways of using optical (MODIS) and passive microwave remote sensing imagery (TRMM) for mapping floods to help reduce the effects of cloud contamination, and optimize the data's spatial resolution and temporal frequency to suit the size and duration of the flood events. (Salvia et al. 2011) presented a methodology to estimate the fraction of flooded area and the mean water level inside a wetland using both active and passive microwave orbital systems. The methodology is based on the quasi-simultaneous measurements of the radiometric polarization difference and the differences of the backscattering coefficient with respect to a reference image.

1.2.3 Forest monitoring

Forests cover about a third of the Earth's land surface, and they influence the exchange of gases and energy between the atmosphere and the surface. About 80% of the global biomass is contained in forests, and this forms the central component of the stocks and acquisition of carbon in the biosphere. The growth and distribution of forests has a critical impact on atmospheric carbon dioxide concentrations, a central issue in global change research. To meet the various information requirements in forest studies different data sources, like field survey, aerial photography and satellite imagery is used, depending on the level of detail required and the extension of the area under study.

Ground-based measurements allow us to evaluate in detail the influence of variables depending markedly on time, such as soil moisture and Leaf Area Index (LAI), but they cover only small forest plots. For the purpose of consistently and repeatedly monitor forests and their parameters over larger areas, it is preferable to use remote sensing data. Several types of remote sensing data, including aerial photography, multi-spectral scanner (MSS), Lidar (Light Detection and Ranging) laser, Active-Passive Microwave data and Videography data have been used by forest agencies to detect, identify, classify, evaluate and measure various forest cover types and their changes.

Over the past decades tremendous progress has been made in demonstrating the potentials and limitations for identifying and mapping various forest surface features using optical remote sensing data. Optical systems, although proved their effectiveness in sensing leaf parameters, are not able to sense the woody biomass. At microwave frequencies, remote-sensing research was mostly based on active systems. Radiometric forestry has received a much lower attention than radar forestry mainly due to poor spatial resolution of spaceborne radiometers. Nevertheless, important experiments about forest emissivity took place using ground-based, airborne, and spaceborne radiometers (Shutko and Chukhlantsev 1982b; Matzler 1994a; Wigneron et al. 1997; Kruopis et al. 1999; Hallikainen et al. 1988; Lang et al. 2000; Lang et al. 2001 and Macelloni et al. 2001). A review was given in (Pampaloni 2004).

Particularly, the capability of microwave radiometers to monitor soil moisture is a subject receiving attention Experiments using both ground based and airborne radiometers have provided an insight into the problem but only a limited number of forests have been observed. Some experimental investigations, carried out over coniferous forests, or deciduous forests in cold climates, indicate that the effects of soil moisture variations on radiometric signatures are very low, even at L band (Guglielmetti et al. 2008), (Grant et al. 2007). Other experiments in temperate climates indicate that a moderate sensitivity to variations of soil moisture exists, at least at L band (Rahmoune et al. 2010). These experimental efforts were aimed at evaluating the overall emissivity and appreciate the sensitivity of the emission process to forest variables, such as branch volume, LAI, and soil-moisture content (SMC).

More recently, studies about forest emission have been stimulated by the development of space projects, such as the Soil Moisture and Ocean Salinity of the European Space Agency, using lower microwave frequencies (L-band) for soil-moisture monitoring (Berger et al. 2003). Although field experiments are fundamental to investigate the potential of radiometers, theoretical simulations carried out using physical models, also add important information. Models allow us to extend the estimates to several cases of possible forest variables, single out all the contributions of forest components, and carry out parametric studies at various frequencies, angles, and polarizations. Theoretical efforts aimed at simulating the electromagnetic behavior of forests were mostly focused on radar applications (Ulaby et al. 1990; Chauhan et al. 1991; Karam 1997; Ferrazzoli and Guerriero 1995). However, physical models of forest emission are also available (Ferrazzoli and Guerriero 1996 and Karam 1997) The basic modeling approach is discrete and based on the radiative-transfer theory ($\tau - \omega$ model). At higher frequencies (C

band and above) there is a strong contribution of leaves to crown attenuation, but at lower frequency (L-band and below), leaves are almost transparent, attenuation is mostly due to branches, and soil contribution can be still appreciable, unless if the forest is dense.

It was found that a simple empirical approach, based on τ and ω parameters fitted over experimental data is not appropriate in the case of forests, due to very limited amount of experimental brightness data presently available at L band and the complexity of the emission/scattering processes, since trunks and branches are not small when compared to sensing wavelength. Therefore, in the algorithm developed to explit SMOS data over land, forests are modeled using a simple zero order RT model, but with τ and ω obtained by fitting the outputs of a theoretical discrete model developed at Tor Vergata University (Rahmoune et al. 2013). τ and ω represent, respectively, the vegetation attenuation properties and the scattering effects within the canopy layer. The algorithm compares the brightness temperatures measured by SMOS with those simulated by a zero order forward model, and starts an iterative procedure which minimizes the "cost function". Further using allometric equations and auxiliary information, the inputs required by the model are related to the maximum yearly value of Leaf Area Index (LAI). The retrieval algorithm estimates soil moisture and optical depth as outputs of the retrieval process. Several more efforts have been done to improve the performance of the forward model and the retrieval algorithm to improve the soil moisture retrieval performance, at least under moderately developed forests (Ferrazzoli et al. 2013 and Rahmoune et al. 2013a).

1.3 Historical notes about Microwave Passive Systems

Most of the instruments placed into the orbit for the study of the Earth's atmosphere and surface have been of the type passive sensors, imagers and sounders operating in visible, infrared and microwave spectral regions. Technology development over the past four decades have allowed then capabilities of the current generation passive sensors to advance far beyond those of the first instruments on Sputnik-1 and also the TV camera on TIROS-1.

As discussed in Section 2.1, a main application of microwave observations is soil moisture monitoring. There can be two approaches through which microwave remote sensing estimating surface soil moisture: active ways by Radar and/or Synthetic Aperture Radar (SAR) with high spatial resolution (in the order of ten to hundred meters) and long revisiting period (about 1 month), passive ways by radiometers with coarse resolution (~ order of tens of km) and frequent temporal coverage (daily or bi-daily). The spectral range of remotely sensed data was considerably enlarged by the use of passive radiometers in the microwave region (section 1.1.7).

Spaceborne microwave observations started Sep 23rd, 1968 with the launch of Cosmos 243 satellite, which carried a non-scanning, nadir viewing 4-channel radiometer with objective to estimate atmospheric water vapor, liquid water, ice cover and sea temperature. The same radiometer was also flown on Cosmos 384 with a lunch in 1970. But the first operational Radiometric imaging started since Oct 15th, 1972, when NOAA-2 S/C, which solely relied upon radiometric imaging to obtain cloud cover data.

Recent and near future spaceborne passive microwave sensors include the Scanning Multichannel Microwave Radiometer (SMMR; 6.6, 10.7, 18.0, 21 and 37 GHz) on board Nimbus-7 Pathfinder (Gloersen and Barath 1977), the Special Sensor Microwave Imager (SSM/I; 19.35, 22.2, 37.0 and 85.5 GHz) on board Defense Meteorological Satellite Program (DMSP) (Hollinger et al. 1990), MSMR (Mutlifrequency Scanning Microwave Radiometer) on IRS-P4 (ISRO), the Advanced Microwave Scanning Radiometer (AMSR-E; 6.925, 10.65, 18.7, 23.8, 36.5 and 89 GHz) of the Earth Observing System (EOS) on board Aqua (Kawanishi et al. 2003), AMSR on ADEOS-II (NASDA), the more recent and first of its kind spaceborne synthetic aperture radiometer with sparsely filled 2-D antenna design, soil moisture and ocean salinity (SMOS) mission by the European Space Agency (ESA), and the upcoming NASA Soil Moisture Active and Passive (SMAP) mission.

1.4 Recent Satellite Missions

1.4.1 Advanced Microwave Scanning Radiometer (AMSR-E)

The Advanced Microwave Scanning Radiometer for the Earth Observing System (AMSR-E) was developed and provided to the National Aeronautics and Space Administration's (NASA) EOS Aqua satellite by the National Space Development Agency of Japan (NASDA), as one of the indispensable instruments for Aqua's mission. AMSR-E is a modified version of AMSR. AMSR-E was launched December 2002 aboard the Advanced Earth Observing Satellite-II (ADEOS-II) (Nakajima et al. 1994), (Imaoka et al. 2002). It is a multichannel microwave radiometer that observes hydrological and geophysical parameters to understand the mechanism of global water and energy circulation. It uses one of the largest microwave radiometer antennas to observe global and continuous phenomena with finer spatial resolution, with respect to previous radiometers. In addition to the time-proven capabilities for observing such variables as water vapor, precipitation, and sea surface wind speed, novel geophysical parameters, including sea surface temperature (SST) and soil moisture, are retrieved by using microwave frequency channels. Near-real-time products are further used to investigate satellite data assimilation into weather forecasting models and to contribute to improved forecasting accuracy. AMSR-E aboard Aqua is a joint project between Japan and United States as well as an international activity in which scientists worldwide collaborate in algorithm development, data validation, and scientific research.

The mission aims at exploring the global hydrologic cycle and its role in the earth's climate system. AMSR-E plays an important role in the Aqua mission, by measuring geophysical parameters supporting several global change sciences and monitoring efforts, including precipitation, oceanic water vapor and cloud liquid water, sea surface wind speed, sea surface temperature, soil moisture, snow cover, and sea ice parameters.

In the AMSR-E instrument design, there are two major improvements over previous spaceborne microwave radiometers for earth imaging: the addition of 6.925-GHz channels and the largest main reflector of its kind, providing higher spatial resolution. The 6.925-GHz channels enable us to observe SST over the global oceans, while the TMI 10-GHz channels only appear to be sensitive to warmer SST above 10^0 C (Shibata et al. 1999). These channels are also useful to investigate soil moisture content. Although TMI realized the higher spatial resolution thanks to the lower orbit altitude of the TRMM, AMSR-E essentially improves the solution and extends its capability to global measurements.

On the afternoon orbit of the Aqua satellite, AMSR-E provides measurement at approximately 1:30 A.M. and 1:30 P.M. This observing local time is not covered by the previous measurements of SSM/I. Having AMSR-E therefore also helps in filling this gap of local observing time. More important is the combination of AMSR-E and AMSR onboard ADEOS-II. This system, combining microwave radiometers of the latest design in morning and afternoon orbits, helps in providing information on diurnal variability of most geophysical parameters necessary for process studies and frequent sampling of transient phenomena like severe tropical storms essential for improving data assimilation techniques.

1.4.1.1 Instrument design and performance

1.4.1.1.1 Overview

AMSR-E is a six-frequency total-power microwave radiometer system with dual polarization capability for all frequency bands. The frequency bands include 6.925, 10.65, 18.7, 23.8, 36.5, and 89.0 GHz.

Conical scanning at 40 r/min is employed to observe the earth's surface with a constant incidence angle of 550. Multifrequency measurement is carried out by the multiple feed-horn antennas mounted on the satellite. Calibration counts are obtained every scan by using the high-temperature noise source (HTS) around a temperature of 300 K, and the cold-sky mirror (CSM) to introduce the temperature of deep space. At the time of the launch the 1.6-m diameter offset parabolic antenna was the second largest spaceborne microwave radiometer antenna of its kind (the 2.0-m antenna of AMSR was the largest). The instrument consumes approximately 350 W of power in normal mode, and weighs 314 kg. Major performance and characteristics are summarized in (Table 1.2). A photograph of the AMSR-E undergoing antenna deployment testing at NASDA's Tsukuba Space Center is shown in Figure 1.9. Overview of the AMSR-E and Aqua spacecraft is shown in Figure 1.10.

Table 1.2: Summary of Major Performance and Characteristic of AMSR-E

Parameters	Performance and characteristics						
Center Frequency (GHz)	6.925	10.65	18.7	23.8	36.5	89.0 (A)	89.0 (B)
Bandwidth (MHz)	350	100	200	400	1000	3000	3000
Polarization	Vertical and Horizontal						
Dynamic range (K)	2.7 to 340						
Incidence angle (deg.)	55.0						54.5
Off-nadir angle (deg.)	47.5						47.0
Beam width (deg.)	2.2	1.5	0.8	0.92	0.42	0.19	0.18
IFOV (km) Cross-track x Along-track	43x75	29x51	16x27	18x32	8.2x14	3.7x6.5	3.5x5.9
Swath-width (km)	1450						
Integration time (msec)	2.5					1.2	

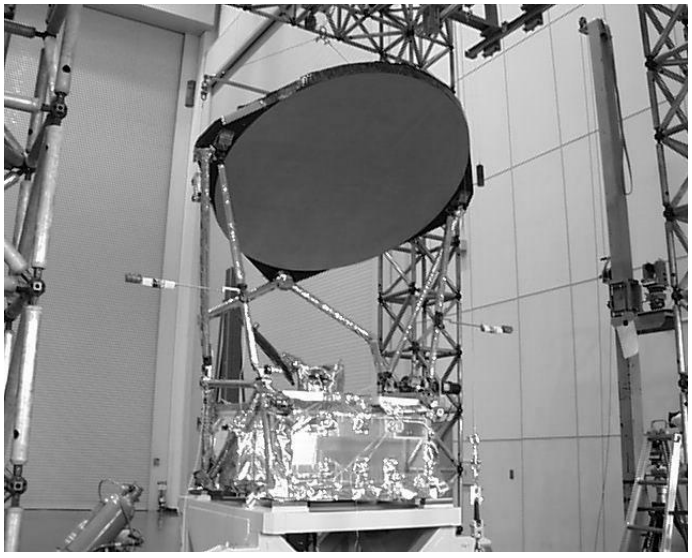

Figure 1.9: Photo of AMSR-E sensor unit during deployment testing at NASDA Tsukuba Space Center

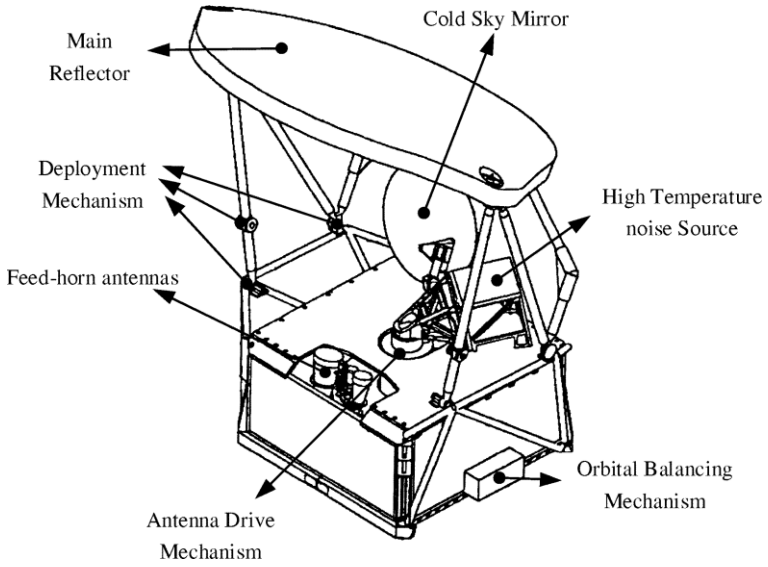

Figure 1.10: Overview of AMSR-E sensor unit

.

1.4.1.1.2 Frequency Bands

Many, but not all, of the bands were selected within the frequency range allocated for earth observation or radio astronomy by the International Telecommunication Union. The 6.925-GHz band is not primarily allocated for earth observation, but defined as the primary band for ground-to-ground and ground-to-satellite radio communications. Thus, there may be some radio-frequency interference (RFI). RFI was detected in brightness temperatures of SMMR 6.6-GHz channels over large cities, as well as in TMI 10-GHz channels over urban areas. However, the effect can be not so strong in remote areas over land and in open oceans far from land. The specific value of 6.925 GHz was chosen for AMSR on ADEOS-II in consideration of electromagnetic compatibility with the platform. To obtain the air temperature sounding channels of the Advanced Microwave Sounding Unit (AMSU) on Aqua is used (but not by conical scanning). For water vapor channels, 23.8 GHz was chosen as the hinge point on the higher frequency side of the water vapor absorption line at 22.235 GHz. This selection differs from that of SSM/I, as well as TMI.

1.4.1.1.3 Antenna Beam Characteristics

Covering a wide frequency range imposes two antithetical requirements on the reflector: large aperture size to achieve high spatial resolution in lower frequency channels and an accurate mirror surface to realize high main- beam efficiency, particularly in 89-GHz channels. The AMSR-E main reflector is an offset parabola, with a projected aperture size of 1.6 m along the beam direction and a focal length of 1.25 m. To reduce weight and minimize thermal deformation in orbit, the main reflector is composed of an aluminum honeycomb panel sandwiched by carbon-fiber-reinforced plastic plates. Six dual-mode feed-horn antennas illuminate the reflector for multifrequency observation. Figure 1.10 shows the array of feed horns. The 18.7- and 23.8-GHz radiometers share an identical feed horn, while two 89-GHz receivers (89A and 89B, two feed horns) are needed to maintain adequate spatial sampling in the along-track direction. The input power is divided into vertical and horizontal polarizations by orthogonal-mode transducers and fed to the subsequent receiver systems.

1.4.1.1.4 Receiver Characteristics

AMSR-E employs total-power radiometers to achieve higher sensitivity than Dicke-type radiometers. Compared to switching-type radiometers that measure reference inputs during some portion of their integration time, a total-power radiometer has the simplest configuration without any compensation mechanisms of gain fluctuation and utilizes "total" incident power on the antenna. The low-noise and high-gain amplifiers using high electron mobility transistor (HEMT) devices were newly developed to achieve enhanced sensitivity in the higher frequency bands (Nakahara et al. 1995). Except for the 6.925-GHz channels, the input radio frequency (RF) is converted to an intermediate frequency. The RF signal in the 6.925-GHz band is directly amplified and detected. To ensure a dynamic range from 2.7–340K, AMSR-E employs an automatic gain control (AGC). The AGC controls not only gains but also offset values of the dc-amplifier block to make calibration counts of HTS and CSM within the range of the output digital number (ten or 12 bits, depending on the frequency).

1.4.1.1.5 Scanning Geometry and Global Coverage

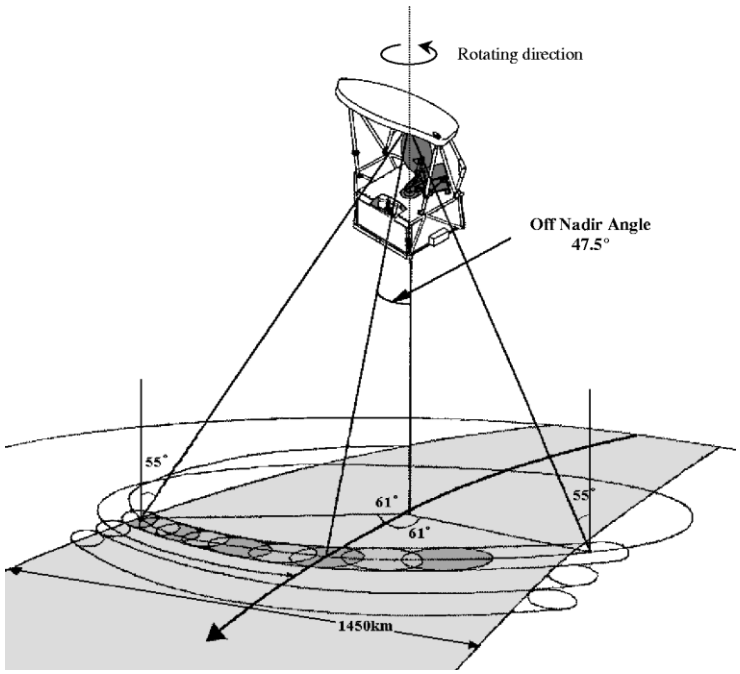

Figure 1.11: AMSR-E scanning geometry

The AMSR-E scan geometry is shown in Figure 1.11. The AMSR-E SU continuously rotates counterclockwise about an axis parallel to the geocentric direction, with an off-nadir angle of 47.5^0 (55^0 incidence angle on the equator). Therefore, the scan direction is from right to left when looking in the satellite traveling direction. Only ±610 (positive sense in a clockwise direction) is used in the forward direction to take effective data of the earth (low data contains ±750 of samples, but this is reduced by ground data processing), resulting in a swath width of approximately 1450 km. The effective observing angle for the 6.925-GHz channels is -610 to +580 due to possible interference in the main beam's field of view (exact angle range should be examined after launch). During each rotation (taking 1.5 s), the sub-satellite point advances a distance of 10.1 km. A sampling period of 2.6 ms corresponds to a cross-track sampling interval of 8.9 km, except for 89-GHz channels. For 89-GHz channels, the sampling period is 1.3 ms, resulting in sampling intervals of 4.5 km (89A) and 4.4 km (89B) on the ground. On each scan, 196 samples (392 samples for 89-GHz channels) are obtained within a $\pm 61^0$ scan angle.

The sampling geometry in the 89-GHz band is a little complicated. A different off-nadir angle of 47^0 is adopted for 89B, resulting in a difference of beam direction from 89A of 15 km in the along-track direction. Three successive scans can cover the earth's surface as shown in Figure 1.12. The distances between two adjacent scan lines differ for 89A to 89B (6.0 km) and 89B to 89A (4.1 km). However, this explanation is only valid for the center of scans. As the scanning proceeds from the center to the end, the two scans (89A to 89B) overlap, and their order is reversed.

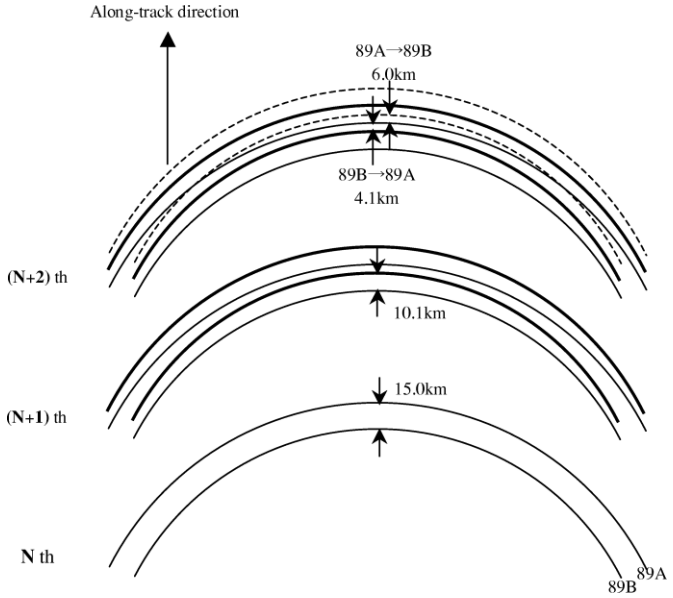

Figure 1.12: Schematic diagram of 89 GHz scan geometry. Beam centers of three successive scans are shown by solid (N), dotted (N+1), and thick-solid (N+2) lines.

The instantaneous field of view (IFOV) of each frequency is shown in Table 1.2. The concept of effective field of view (Kummerow et al. 2001) is not introduced here. In the lower frequency bands, the sampling intervals (10.1 km in along-track and 9.0 km in cross-track directions) are much smaller than the IFOV, so observed targets re heavily oversampled. Utilization of these oversampled data is up to data users. Selection of Aqua's orbit and the AMSR-E swath width of 1450 km enable us to cover the entire earth in two days using ascending or descending data only.

1.4.1.2 Ground data processing

1.4.1.2.1 Dataflow Overview

All science data from the Aqua satellite including AMSR-E are received by two ground stations, Alaska Ground Station (AGS) and Svalbard Ground Station (SGS), and are transferred to the EOS Data and Operations System (EDOS) at NASA Goddard Space Flight Center. The AMSR-E science data are processed into the Rate Buffered Data (RBD). Two RBDs [science RBD and Ground Based Attitude Determination (GBAD) RBD] are then transferred to the NASDA Earth Observation Center (EOC) in Japan for subsequent data processing. All the standard products, including Level 1A, Level 1B, Level 1B-Map, Level 2, Level 2-Map, and Level 3, are produced at EOC and made available for data users via the Earth observation Information System (EOIS) interfaces. Near-real-time products are immediately sent to operational users including the Japan Meteorological Agency (JMA) and the Japan Fishery Information Center. Those data are utilized for investigating practical applications, including satellite data assimilation

into numerical weather forecasting models and surveillance of fishing grounds. The data transmitted to the Earth Observation Research Center (EORC) are used for processing research products and calibrating and validating the standard products.

In parallel with the processing and distribution described above, the Level 1A data generated by NASDA are transmitted to the U.S. ground segments for the U.S. team's processing (Level 2 and above). Based on this product, geophysical products are then produced by the Science Investigator-led Processing System (SIPS) at the Global Hydrology and Climate Center (GHCC). The National Snow and Ice Data Center (NSIDC) DAAC is responsible for archiving and distributing the U.S. products. The AMSR-E real-time data are also downlinked to any ground station via the direct broadcasting capability of the Aqua satellite.

1.4.1.2.2 Data Products

All the data products are stored in the Hierarchical Data Format (HDF) developed at the National Center for Supercomputing Application (NCSA) to maintain minimum compatibility with NASA's HDF-EOS format.

1) Level 1A: The Level 1A product stores observed digital counts converted from instrument output voltages. Other necessary information for subsequent processing, including navigation and attitude information, latitude and longitude for each observed point, raw calibration counts and derived radiometric calibration coefficients for each scan, surface type information (land area percentages in a 3-dB footprint), and instrument monitoring data, is also retained. All the scan points within a 75 scan angle are retained. The data are not map-projected, but stored in the original swath format.

2) Level 1B: Although the Level 1B data structure is almost the same as that of Level 1A, it stores brightness temperatures instead of raw observation counts. First of all, antenna temperatures are derived by using the radiometric calibration coefficients contained in the Level 1A data. Brightness temperatures are then computed by a simple linear combination of vertically and horizontally polarized antenna temperatures and the cosmic background temperature. The number of samples in a scan is reduced in the Level 1B processing from 243 (486 for 89 GHz) to 196 (392 for 89 GHz), corresponding to the changes of valid scan angle from 75^0 to 61^0. The Level 1B Map is a map-projected regional subset product of brightness temperatures. The image size of 300 X 300 pixels, with approximately 10-km pixel spacing, results in map coverage of 3000 km X 3000 km.

3) Level 2: Through retrieval algorithms, eight geophysical parameters are computed by combining multifrequency dual polarized brightness temperatures. The geophysical parameters include integrated water vapor (total precipitable water), integrated cloud liquid water, precipitation (surface rain rate and accumulated amount), sea surface wind speed, sea surface temperature, sea ice concentration, snow water equivalent (or depth), and soil moisture content. The product is categorized into two groups: standard products and research products. The standard products are operationally processed at EOC by using standard algorithms that are relatively matured and well-validated. In contrast, the research products are beta versions of the standard products, or products based on completely new concepts. The Level 2 products are still swath-type data with the same sampling interval as that of lower frequency channels (approximately 10 km). Latitude and longitude for each footprint and ancillary information such as quality flags are appended, which includes air temperature and humidity profiles, are used in processing Level 2 products as ancillary information.

4) Level 3: The Level 3 products are daily and monthly grids of Level 1B and Level 2 products. Depending on the products, 0.25 X 0.25 grids and/or polar stereographic grids with 25-km resolution are used.

For the current study, we have used brightness temperature values, provided by level 2 product (AE_L2A.2 - AMSR-E/Aqua) global swath brightness temperatures, resampled at resolutions of 56 km, 38 km, 21 km, 12 km, and 5.4 km. Level 3 (AE_Land3.2 - AMSR-E/Aqua) level 3 global daily surface soil moisture with vegetation water content, surface temperature, & brightness temperature are generated on a nominal 25-km equal area earth grid by time-compositing the level 2B parameters separately for ascending and descending passes. This product was used to compare AMSR-E global soil moisture map with soil moisture obtained from other data products (SMOS).

1.4.2 Soil Moisture and Ocean Salinity (SMOS) Mission:

1.4.2.1 Mission objective and characteristics

The SMOS (Soil Moisture and Ocean Salinity) mission was approved by the European Space Agency (ESA) in May 1999. Its objective is to provide frequent global Soil Moisture and Sea Surface Salinity (SSS) maps. SMOS was launched on November 2, 2009, and after the first calibration and checkout period (the so-called Commissioning Phase), processed products started to be distributed.

The SMOS satellite, launched with a ROCKOT Breeze KM, is on a low Earth polar Sun- synchronous dawn-dusk orbit, at 763 km of altitude, covering a complete orbit around the Earth in approximately 100 minutes. It is characterized by a 3-day revisit time at the Equator and a spatial resolution ranging between 32 and 100 km.

The single payload of the SMOS mission is the Microwave Imaging Radiometer by Aperture Synthesis (MIRAS,(McMullan et al. 2008)); MIRAS is a 2D interferometric radiometer operating in the protected L-band with a nominal frequency of 1413.5 MHz and a bandwidth of 27 MHz. It consists of three deployable arms connected to a central hub (8-m diameter radiometer when completely deployed). The arms are equally spaced with an angular separation of 120^0. Each arm encompasses three segments, each one containing six L-band radiometers (Light-weight Cost-Effective Front-end, LICEF). Four more radiometers are situated in the central hub, for a total of 66 radiometers. In addition to that, there are three Noise Injection Radiometers (NIRs) located in the central hub, each of which consists of two LICEF receivers coupled to a single antenna. The total number of elements is therefore 69 antennas and 72 receivers, arranged as shown in Figure 1.13.

The integration time used in MIRAS is 0.158 s, with an interval between snapshots of 1.2 s, allowing a snapshot radiometric sensitivity of 3.5 - 5.8 K over land and 2.5 - 4.1 K over ocean. Every 1.2 seconds data provided by the Control and Monitoring Network (CMN), by the Noise Injection Radiometer (NIR), by the LICEF units, plus additional information from the platform (attitude information) are recorded in the Raw-Data product. Raw Data are downloaded through the X-band channel when a ground contact is established. MIRAS can operate according to two different observation modes:

Dual-Polarization mode: Brightness temperatures are alternately measured in each polarization every 1.2 s, and all the LICEFs measure the same polarization.

Full-Polarization mode: Brightness temperatures in H and V polarization as well as the third and fourth Stokes parameters are measured. Four consecutive integration times are used for each measurement.

During the first integration time, all receivers measure the X polarization and during the third integration time, the Y polarization. In the other two integration times the polarization of one arm is the opposite of the other two arms to perform measurements of the cross-polarization terms $T_{(XY/YX)}$. The arm in the alternative polarization rotates in a clockwise direction completing 4 rounds in each integration time.

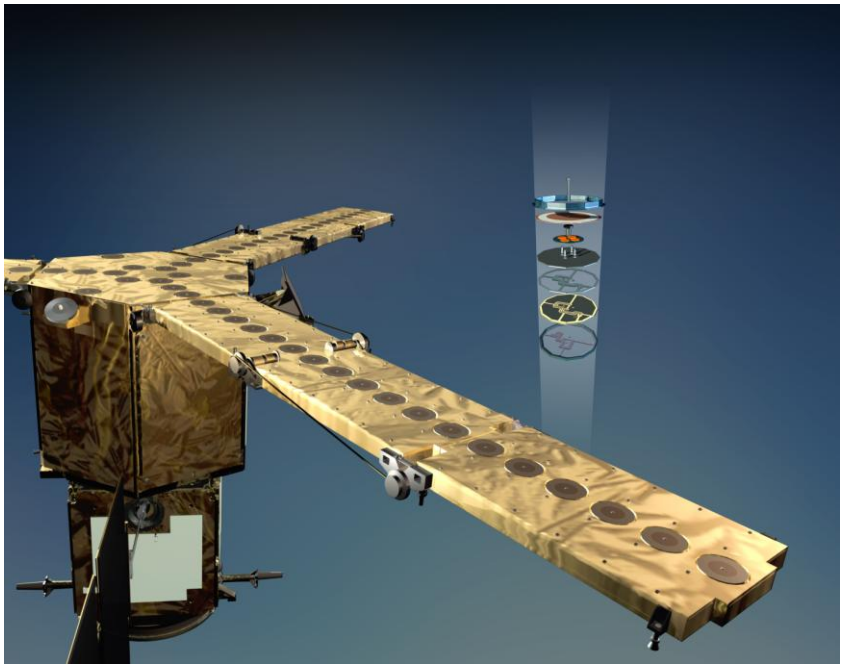

Figure 1.13: MIRAS arm and LICEF details. Courtesy ESA

Brightness temperatures are reconstructed in the director cosine domain (ξ, η) :

$$(\xi, \eta) = (\sin(\theta)\cos(\phi), \sin(\theta)\sin(\phi)) \tag{1.27}$$

where θ is the angle from the normal to the instrument plane ($0 \leq \theta \leq \pi/2$) and ϕ is the angle in the instrument plane ($0 \leq \phi \leq 2\pi$). Theoretically, the maximum visible space is the area inside the unit circle ($\xi^2 + \eta^2 = 1$) even though non-zero antenna pattern backlobes also contribute to the T_B image in the unit circle. Geometric conventions are sketched in Figure 1.14.

- visibility samples are measured and plotted as a function of the distance between antennas in the horizontal (u) and vertical (v) components;

- the visibility map is properly repeated to compute the Inverse Fourier Transformation (F^{-1}) leading to the brightness temperatures map (T_B) in the cosine domain, and finally

- the periodic extension is removed from the brightness temperature map.

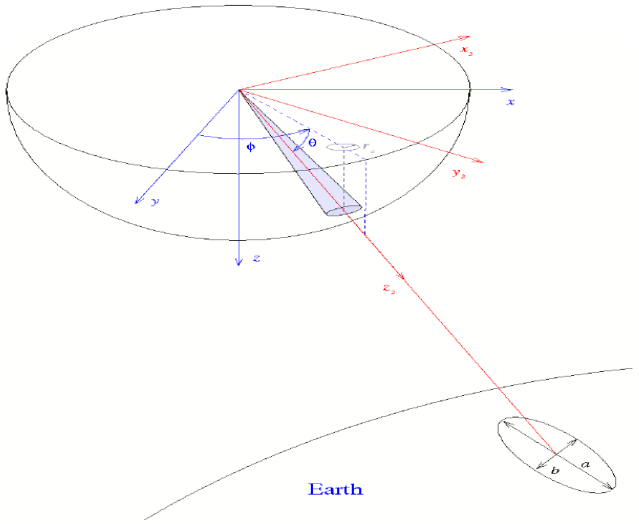

Figure 1.14 : Geometric concentions for the definition of the (ξ, η) coordinates.
Spatial resolution is defined as $\Delta x = \sqrt{a.b}$

According to the MIRAS instrument design the distance between antennas (d) does not satisfy the Nyquist criterion ($d \leq \lambda/3$) (Camps et al. 1997) so part of the Field of View (FOV) is affected by aliasing; the six closest aliases circles are shown in Figure 1.15, where the black dots stand for the theoretical maximum FOV, the red ones are the aliasing circle borders, and the central green zone is the Alias-Free Field of View (AF-FOV).

The AF-FOV can be extended considering that sky has low, stable, and known emission. This contribution can be modeled and its aliasing effects compensated, leading to the definition of the so-called Extended Alias-Free FOV (EAF-FOV). The black dots are the theoretical largest FOV, and the yellow zone in the center of the figure is the EAF-FOV.

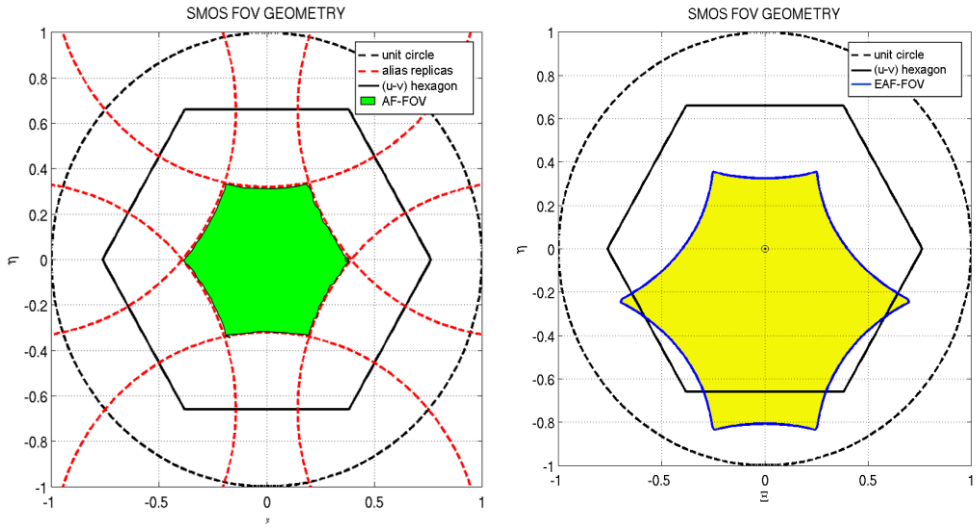

Figure 1.15 : SMOS (a) AF and (b) EAF-FOV in the cosine domain: (black) unit circle, (red) SMOS aliased zone borders, and (green) SMOS (a) AF-FOV and (b) EAF-FOV

Due to this particular feature and to the dimensions of the FOV (approximately 1000 x 1000 km) instrument parameters change according to their position in the FOV, among them the radiometric accuracy and sensitivity, the incidence angle, and spatial resolution Figure 1.16 (a). Namely radiometric accuracy and sensitivity ranges in the intervals 2.5 - 4 K and 3.5 - 7 K, respectively, while incidence angle can assume values between 0^0 and 60^0 giving a spatial resolution ($\Delta x = \sqrt{a.b}$) is bound between 32 and 100 km.
In Figure 1.16 (b) the geometric parameters incidence angle (blue line) and spatial resolution (red line) are presented.

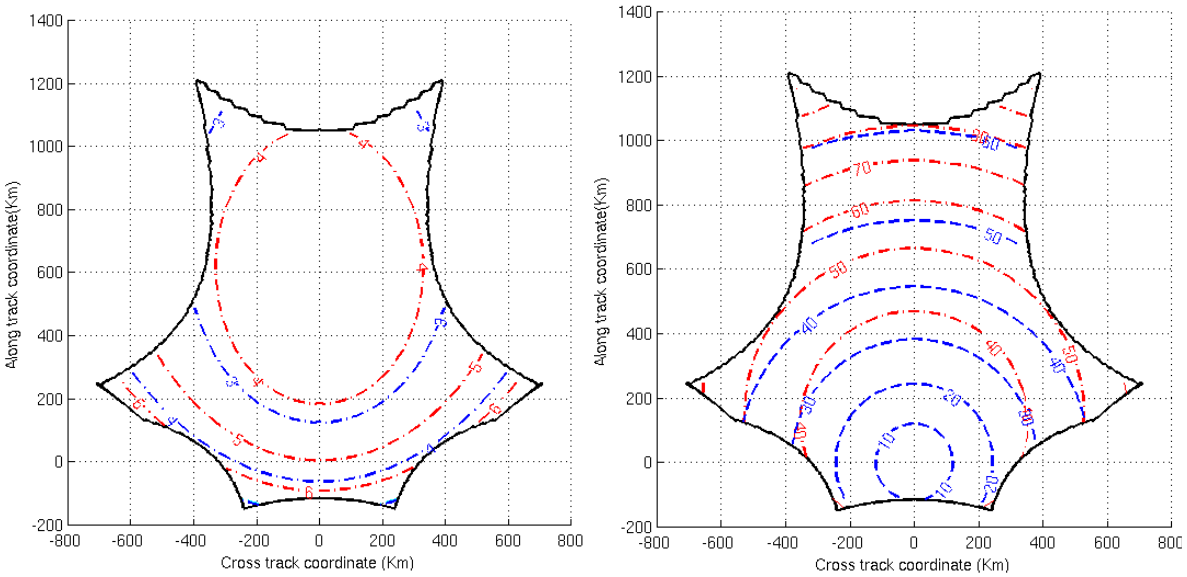

Figure 1.16: (a) Radiometric Radiometric (blue) Accuracy and (red) Sensitivity, and (b) (blue) Incidence Angle and (red) Spatial Resolution [calculated using SEPS].

1.4.2.2 ISEA grid

ISEA grids are simple in concept. Begin with a Snyder Equal Area projection to a regular icosahedron (see the stereo pairs in figure 17 (a)) inscribed in a sphere. In each of the 20 equilateral triangle faces of the icosahedrons inscribe a hexagon by dividing each triangle edge into thirds (see the large gray hexagon in figure 17 (b)). Then project the hexagon back onto the sphere using the Inverse Snyder Icosahedral equal area projection. This yields a coarse-resolution equal area grid called the resolution 1 grid. It consists of 20 hexagons on the surface of the sphere and 12 pentagons centered on the 12 vertices of the icosahedrons (Carr et al. 1997).

To form higher resolution grids, tessellate each equilateral triangle in the planar view with more hexagons and use the inverse projection back to the sphere. The details of the regular tessellation are as follows: Always center a hexagon about the center point of the equilateral triangle. For odd resolution grids, orient the hexagon so its base is parallel to the base of the triangle. For even resolution grids orient the hexagon so a vertex points at the base of the triangle. Figure 1.17 (a) shows the central hexagons for resolutions 1 and 2 in gray and black, respectively.) Select the edge length of a resolution n +1 hexagon so it is 1=p3 times the edge length of a resolution r hexagon. Thus, the area of a hexagon reduces by a factor of $1/\sqrt{3}$ with each increase in resolution. As the resolution increases by 1, the tessellation procedure produces a hexagon centered on each hexagon vertex and center point of the lower resolution tessellation. As

illustrated in Figure 1.17 (b), the procedure partitions a lower resolution hexagon cell into one central cell and six fractional (1/3) cells. This is not as simple as partitioning a large square into exactly four smaller squares.

While the merits of strictly nesting cells within cells depend on the context, one clear merit is aggregation simplicity. The ISEA fractional cells create aggregation and disaggregation problems that are currently under investigation. The orientation of the icosahedron relative to the globe is an important consideration. The selected orientation for the ISEA grid creates symmetry about the equator. This is desirable for numerical modeling purposes. There are always 12 pentagon cells about the vertices of the icosahedron. The selected orientation places 11 of the pentagon cells over water areas, so that most land mass views will be completely composed of hexagons.

The advantages of the ISEA grids are (1) they have irregularities (12 pentagon cells) that are minor nuisances rather than being pathological singularities, (2) they are suitable for modeling on all parts of the globe including the poles, (3) they preserve symmetry about the equator, (4) they provide an infinite nesting of equal area sub-grids, and (5) they provide a basis for uniform global density of sampling for data at all spatial resolutions. The grid facilitates comparisons between high and low latitude data and high and low spatial resolution data. The grid also improves the isotropy of finite-difference quantities compared to those calculated for rectangular grid schemes. For example (Fisch et al. 1986) note that two dimensional Navier-Stokes implementations are optimal with hexagons. Finally, no ambiguity exists about nearest neighbors as all nearest neighbor cells share an edge with a reference cell and their distances to the center of a reference cell are nearly equal.

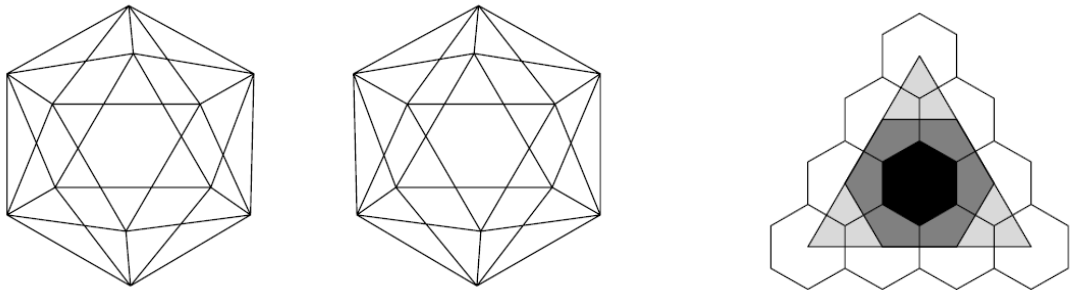

(a) (b)

Figure 1.17: (a) Stereo pairs of a regular icosahedron., (b) Subdividing the faces of a regular icosahedron: Gray and black regions represent the central hexagons for resolutions 1 and 2, respectively.

SMOS products (i.e. L1C brightness temperatures in X and Y pol., and L2 soil moisture) are defined on the ISEA 4H9 grid with a spatial resolution of 15 km. Each point (or node) of this grid is known as a DGG (Discrete Global Grid) that has fixed coordinates (i.e. Latitude, Longitude) and is assigned an identificator the "DGG Id". All the grid point information (DGG Id, Latitude, Longitude) has been gathered in an ascii file isea4h9.txt.gz.

It is worth mentioning that the grid of SMOS products is 15 km of spatial resolution and the radiometric resolution of the instrument is ~40 km.

1.4.2.3 Data Products

The following SMOS data products are available:

- Level 1A product: calibrated visibilities between receivers prior to applying image reconstruction.

- Level 1B product: output of the image reconstruction of the observations and comprising the Fourier component of the brightness temperature in the antenna polarization reference frame.

- Level 1C product: multi-angular brightness temperatures at the top of the atmosphere, geolocated in an equal-area grid system. Two different Level 1C products are generated according to the surface type: one containing only sea and the other only containing land pixels. Two sets of information are available: pixel-wise and snapshot-wise. For each Level 1C product there is also a browse product containing brightness temperatures for an incidence angle of 42.5°.

- Level 2 soil moisture product: containing not only the soil moisture retrieved, but also a series of ancillary data derived from the processing (nadir optical thickness, surface temperature, roughness parameter, dielectric constant and brightness temperature retrieved at top of atmosphere and on the surface) with the corresponding uncertainties.

- Level 2 ocean salinity product: containing three different ocean salinity values derived from retrieval algorithms using different assumptions for the surface roughness correction and the brightness temperature retrieved at the top of atmosphere and on the sea surface (with the corresponding uncertainties).

- Near-real time product: similar to the Level 1C product but adjusted to requirements of operational meteorological agencies such as ECMWF and Météo France, available 3 hours from sensing. It will contain brightness temperatures at the top of the atmosphere on an ISEA grid with reduced spatial resolution.

For the current study,L2 soil moisture data were used. The focus was on the forested area. The L2 SM retrieval algorithm used two types of auxiliary data files: static and dynamic. The static data do not vary over time or have slowly varying quantities. They include the soil texture maps from FAO (FAO 1988), the land use maps from ECOCLIMAP (Masson et al. 2003b) and MODIS, and the topography index (Mialon et al. 2008). The dynamic data provided time varying quantities (snow, freeze defreeze, rain, temperature) obtained from the European Centre for Medium Range Weather Forecasts (ECMWF) forecasts.

The algorithm is based on two main components. The first consists of a forward model, which estimates the brightness temperature emitted by land nodes of SMOS using a priori information (auxiliary data) about land cover, surface temperature, Leaf Area Index (LAI), etc., and initial estimates of soil moisture taken by the data base of the ECMWF data. The second consists of an inversion process, which estimates the actual soil moisture and optical depth by using Level 1C multiangular measurements, forward model outputs and a Cost Function. The radiative transfer parameters τ (optical depth) and ω (albedo) are estimated using the synthetic outputs of the theoretical model, according to the procedure which was further developed and described in further sections of the thesis.

1.5 Research objectives:

Estimation of soil moisture from radiometric measurements is not simple and direct since there are many soil and vegetation parameters affecting the land emission. The development of algorithms to compute bio/geophysical variables from brightness temperature measurements and the assessment of the impact of each of the involved parameters is crucial to have accurate soil moisture estimations. The radiometric measurements vary drastically over vegetative surfaces in different environments. An attempt is made to understand the behavior of soil moisture on different land surfaces when studied through radiometer at different frequencies.

The subject of the thesis is "MICROWAVE RADIOMETRY OF VEGETATED SURFACES IN DIFFERENT ENIRONMENTS ", with first part investigating flooding events in short vegetation at higher frequencies (C-band and above) and second part exploiting lower frequency (L-Band) over forests.

The first part of the PhD work discusses the use of multifrequency AMSR-E signatures in floods monitoring and shows tests over the part of Indian Brahmaputra basin (test sites at North Lakimpur district). The temporal evolution of parameters defined in the literature, such as FWS, and PI is analyzed, and results are compared against available ground measurements of river water level. Techniques aimed at eliminating images affected by heavy rainfalls are also investigated. Radiometric signatures of L-band could not be used in this area due to high Radio Frequency Interference (RFI) in Asian regions.

The second part of the research was carried out as part of the background research for the SMOS mission. At the spatial resolution of SMOS (~40Km), many pixels over land contain a certain percentage of forest cover. Forests usually consist of rather thick and dense vegetation layers. However modelling studies have shown that it might be possible to monitor soil moisture in moderately dense forests if forest emission can be modeled correctly. In this thesis, last results about the retrieved soil moisture are presented using both the presently available algorithm and a refined one, based on a revised forward model, which will be implemented in the next version of the processor.

Retrieved values of optical depth τ have been compared against tree height made available by NASA Earth Observatory. For both configurations, the retrieved soil moistures were compared against IN-SITU measurements of the SCAN/SNOTEL network which includes several forest sites in the US, for which multitemporal measurements of soil moisture and other environmental variables are available and RFI problems were moderate. By considering the multitemporal series, for each node we have compared the retrieved and the measured values of soil moisture for the various cases mentioned above. A further analysis using the soil moisture retrieved by the different algorithms exploiting the Advanced Microwave Scanning Radiometer for the Earth (AMSR-E) is also carried out and results were compared against the ones obtained by SMOS.

1.6 Organization of the Thesis

This Ph.D. Thesis focuses on understanding of microwave radiometer observations user different environmental conditions, and it is organized as follows:

Chapter 2 describes the variables influencing the microwave emission of land covers, as well as the basic models adopted to estimate the dielectric constant of soils, and revises the land emission models (including radiative transfer principles) which are used at present in soil moisture retrieval algorithms.

Chapter 3 describes the results of the tests performed using selected AMSR-E channels on the parts of Brahmaputra Basin, India for analyzing the inundated areas in both bare and vegetated land.

Chapter 4 investigates the capability of SMOS MIRAS radiometer to monitor soil moisture over forests of North America.

2 Microwave Emission of Land covers

Although there have been a number of space borne microwave instruments since the late 1970's, antenna technology and the need to accommodate requirements of the atmospheric and ocean sciences have resulted in these sensors operating at frequencies higher than what is deemed optimal for soil moisture estimation (6.9, 10, 19, 37, and 85 GHz). Research in soil moisture remote sensing began in the mid 1970's shortly after the surge in satellite development (Barton 1978; Eagleman and Lin 1976; Idso et al. 1975; Njoku and Kong 1977 and Schmugge et al. 1977). Theoretical and empirical evidence suggest that the 1400-1427 MHz region (L-band) is most suitable for soil moisture radiometry because long wavelengths penetrate soil and vegetation to a greater extent than higher frequencies (Jackson et al. 1993 and Njoku and Entekhabi 1996) and transmission is prohibited in the band by the Federal Communications Commission so that it remains suitable for radioastronomy observations (cosmic hydrogen absorption occurs at 1420 MHz).

At 1400 MHz, there is a large contrast between the dielectric properties of liquid water (~80) and dry soil (< 4). Several investigators (Wang and Schmugge 1980; Dobson et al. 1985 and Ulaby et al. 1986b) studied the dielectric properties of wet soil. As the moisture increases, the dielectric constant of the soil-water mixture increases and this change is detectable by microwave sensors (Njoku and Kong et al. 1977). The microwave brightness temperature of an emitter of microwave radiation is related to the physical temperature of the source through the emissivity as mentioned in section (1.1.3). The depth through which energy is emitted and sensed by microwave radiometers has been the subject of research and discussion for many years, but it varies, depending on the frequencies we are studying, viz., for L-Band, it is on the order of about 5 cm.

This chapter describes the properties of soils and vegetation, and revises the land emission models which are used at present in soil moisture retrieval algorithms from microwave remote sensing data.

2.1 Bare Soils

2.1.1 Physical properties of soils

An accurate estimation of spatially variable soil media properties is necessary to develop reliable models of flow and transport throughout the soil-plant-atmosphere continuum, for efficient management of resources, and for maintenance of environmental quality. Soils consist of a mix of air, water, organic matter, and mineral particles. According to (Jenny 1994), soils result from the combination of climate, organisms, relief, parent material, and time. Further information on soil properties is reported, among others, in (Brady and Weil 2003 and Behari 2005). Next sections briefly summarize the main soil physical properties.

2.1.1.1 Texture

The size distribution of primary mineral particles, called soil texture, has a strong influence on the properties of a soil. It usually ranges from below 0.002 mm to above 2 mm in diameter. The fraction above 2 mm is classed as gravel, and the fractions below 2 mm are classed as clay, silt, or sand as is indicated in Table 2.1. The relative proportions of clay, silt, and sand determine the soil texture. The three fundamental groups of soil are sands, loams, and clays, but there are many other types named according to the USDA soil classification triangle shown in Figure 2.1.

Texture affects other soil properties as shown in Table 2.2 Fine-textured soils (clays) hold more water than coarse-textured soils (sands), and thus different soils will have a different dielectric constant behavior (0) which will impact the intensity of the soil emission.

Table 2.1: Classification of soil particles as a function of their diameter (in mm)

Sand					Silt	Clay
Very Course	Coarse	Medium	Fine	Very fine		
2.0 to 1.0	1.0 to 0.5	0.5 to 0.25	0.25 to 0.10	0.10 to 0.05	0.05 to 0.002	<0.002

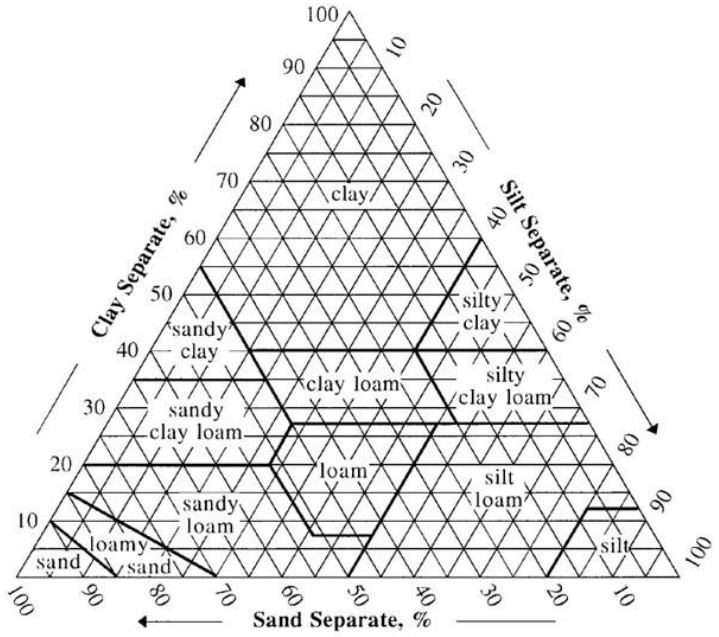

Figure 2.1: USDA Soil classification traingle

Table 2.2: Properties of Soil as a function of Texture

	Sand	Silt	Clay
Permeability	rapid	low to moderate	slow
Porosity	large pores	small pores	small pores
Water holding capacity	limited	medium	very large

2.1.1.2 Bulk and solid phase density

Soil is a typical heterogeneous multiphasic porous system which, in its general form, contains three natural phases: (1) the solid phase or the soil matrix (formed by mineral particles and solid organic materials); (2) the liquid phase, which is often represented by water and which could more properly be called the soil solution; and (3) the gaseous phase, which contains air and other gases.

Soil bulk density ρ_b [g/cm3] is defined as the ratio of the mass of dry solids to the bulk volume of the soil occupied by those dry solids:

$$\rho_b = \frac{Massofdrysoil}{Volumeofbulksoil} = \rho_p \frac{c_s A_s}{D_s A_s} = \rho_p \frac{c_s}{D_s} \tag{2.1}$$

being ρ_p the soil phase density, A_s the area, c_s the equivalent depth filled with solid, and D_s the total equivalent density of the soil made up of solids, water, and air. The density of the solid phase is constant for a soil type, and varies from 1.3 to 2.1 g/cm3 in sands, from 1.2 to 2.6 g/cm3 in clays, and from 0.8 to 1.6 g/cm3 in loams (Chukhlantsev 2006). On the contrary, the bulk density has not a unique value since depends on compaction, swelling, etc. Porous soils have low ρ_b and those compact have higher values. The range of possible values varies from 1 to 1.6 g/cm3 for clay, clay loam, and silt loam soils, and from 1.2 to 1.8 g/cm3 in sands and sandy loams.

2.1.1.3 Pore space or porosity

Pores are the void spaces between soil particles. Pore spaces of dry soils are mostly filled with air, while water fills the pores of wet soils. Processes such as infiltration, ground-water movement, and storage occur in these void spaces. Porosity is in turn affected by texture, soil structure, compaction, and organic matter. The porosity is determined from the bulk density ρ_b and particle density ρ_p (see section 2.1.1.2) as,

$$P_s = 1 - \frac{\rho_b}{\rho_p} \tag{2.2}$$

Pores in a soil have a large variability in arrangement, size, and shape. Sands have very few small pores which hold water, while clays have many large pores which are needed for the rapid water intake and distribution of water. Typical values of the porosity range from 25-50% in sands, from 35-50% in loams, and from 33-60% in clays (Fetter 2001).

2.1.1.4 Permeability and water holding capacity

Permeability is the rate at which fluid can flow through the soil pores, while water-holding capacity is the ability of soils to hold water for plant use. Both parameters are a function of soil structure, porosity, and texture as summarized in Table 2.2.

2.1.1.5 Structure

Soil structure refers to the way sand, silt, and clay particles are arranged into clumps or aggregates. The aggregates are bound together by clay and organic matter. Structure affects drainage, root growth, infiltration, germination, and aeration.

2.1.1.6 Temperature

Soil temperature determines the chemical reaction within a soil and, thus, plants growth, water movement and availability of nutrients. Soil temperature depends on meteorological and physical soil properties such as color, surface roughness, and water content. For instance, dark soils absorb more heat than smooth light-colored ones and thus warm faster. On its part, soil moisture affects the rate of temperature change:

more heat is needed to warm a wet soil than a dry one. The temperature of soils follows the temperature of the air, but with a time lag. This effect diminishes with soil depth.

2.1.1.7 Water in soils

Water content is one of the most variable characteristics of soil. Although there is not a unique classification of water in soils, the common classification divides it into bound and free water. Bound water is the water adsorbed by the surface of soil particles, while free water is the liquid water located in the pore spaces. Bound water depends on soil texture and takes the minimum values (2-3%) in sands, and the maximum (20-40%) in clays. The soil moisture, or water in a soil, is usually determined in two ways:

Gravimetric soil moisture w_g, which depends on the wet and dry weights of the soil sample (w_w and w_d respectively),

$$w_g = \frac{w_w - w_d}{w_d} \tag{2.3}$$

Volumetric soil moisture m_v, which depends on the volume of water V_w, the volume of the soil sample V_s, the soil bulk density ρ_b, and the density of wet soil ρ_{ws} and water ρ_w,

$$w_s = \frac{V_w}{V_s} = w_g \frac{\rho_{ws}}{\rho_w} = m \frac{\rho_b}{\rho_w} \tag{2.4}$$

The field capacity and wilting pointing are, among other hydrological parameters, involved in the dielectric constant models. The field capacity (FC) is the maximum amount of water held in a soil against gravity or amount of water held in soil after excess water has drained away. Physically, it is the water held at a soil at a tension of 1/3 bar. The field capacity can be estimated from the volumetric soil moisture and the weight fractions (in %) of sand S and clay C as (Wang and Schmugge 1980)

$$FC = 0.3 - 0.25S + 0.5C \tag{2.5}$$

The wilting point (*WP*) is the level of soil moisture below which plants wilt, and is usually taken as the soil moisture at a tension of 15 bar. The wilting point is estimated from the textural composition as (Wang and Schmugge 1980),

$$WP = 0.06774 - 0.00064S + 0.00478C \tag{2.6}$$

The difference between field capacity and wilting point is the available water content.

Last but not least, organic litter layers on top of soils as well as the organic matter content intermixed in mineral soils are very important properties (Bot and Bernites 2005): Plant residues that cover the soil surface protect the soil from sealing and crusting by raindrop impact, thereby enhancing rainwater infiltration and reducing runoff. Organic matter affects both the chemical and physical properties of the soil and its overall health. It influences soil structure by an enhanced stability of soil aggregates and pores through bonding/adhesion of particles and increases diversity and activity of soil organisms, and nutrient availability. Furthermore, and very importantly, organic matter increases the soil moisture holding capacity by increasing the soil porosity as well as (like in case of clay minerals) through high water-binding capacities of humic substances. (Miller 1977) stated that typically 1-3 kg/m^2 of liquid water are stored in a medium dense forest vegetation, and a like amount can be retained on the forest floor. Helvey

and Patric (1965), reported that the water storage capacity of the forest floor can be 135-170% of the weight of the forest floor litter.

2.1.2 Dielectric constant of soils

The dielectric constant of the soil is a measure of the response of the soil to an incident electromagnetic wave. This response is composed of two parts (real and imaginary), which determine the wave velocity and energy losses respectively. In a non-homogeneous medium such as the soil, the dielectric properties have a strong impact on its microwave emission. However, the relationship between the soil dielectric constant $\varepsilon_s = \varepsilon_s^{'} + j\varepsilon_s^{"}$, and the soil physical properties is not straightforward, rather it is combination is individual dielectric constants of its complements (i.e., air, water, dry soil etc). From the measured value of dielectric constant, the emissivity of the soil at a given frequency can be calculated. The physical explanation is based on the large permanent dipole of water (displacement of positive and negative molecular charge due to the position of the hydrogen atoms in relation to the oxygen atom), resulting in a significantly higher dielectric constant (relative permittivity) compared to most other natural materials. Therefore, the proportion of water strongly affects the measured permittivity of a soil. Permittivity of terrain typically increases slowly with increasing moisture content, then, beyond a threshold value, increases steeply with moisture content (Solimini 2013). Figure 2.2, shows real and imaginary parts of permittivity at L and C bands of two different soil types at L and C band vs Volumetric water content (Wang and Schmugge 1980). Permittivity results from a complex contribution of the soil's components, air, solid particles and water, and several so-called dielectric mixing models exist to estimate soil moisture from it.

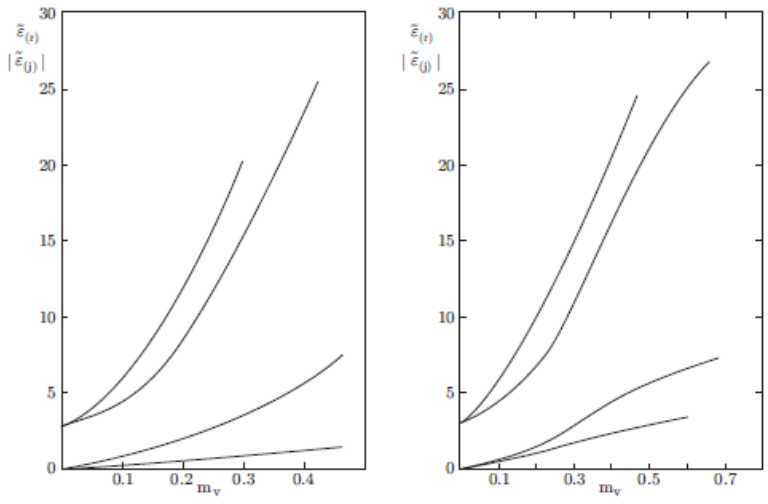

Figure 2.2: Relative real (upper curves) and imaginary (lower curves) parts of permittivity of two different soil types at f = 1.4 GHz (left) and f = 5.0 GHz (right) vs. volumetric water content m_v (m^3/m^3). (Solimini 2013)

A large number of studies have been performed during the last decades to find out this relationship since it plays an important part in the soil moisture retrieval algorithms from remote sensing data (Birchak et al. 1974; Hipp 1974; Wang and Schmugge 1980; Topp et al. 1980; Hallikainen et al. 1985; Dobson et al. 1985; Shutko and Rentov 1982a; Mironov et al. 2004; Roth et al. 1992; Peplinsky et al. 1995; Curtis 2001 and Calvet et al. 1995). Some of these models are simple empirical models in which data is fitted by a curve unique for all soils; others propose semi-empirical approaches which take into account some soil

physical properties. The dielectric constant of dry soils is almost independent of temperature (Topp et al. 1980) and frequency. On the contrary, wet soils show a complex behavior depending on the interaction between soil, water, and air particles. (Hallikainen et al. 1985) performed a series of dielectric constant measurements of five soils with different texture composition at frequencies between 1.4 and 18 GHz and found out that texture has a strong effect on the dielectric behavior which is especially pronounced at frequencies below 5 GHz. In the dielectric-mixing model by (Roth et al. 1992), differences in soil texture and bound water and free water are ignored altogether. Next sections review some of the most commonly used dielectric constant models relevant to the thesis work. More information can be found in (Behari 2005 and Chukhlantsev 2006). A thorough review on soil moisture measurements is presented by (Robinson et al. 2008).

2.1.2.1 Empirical approach

In this approach, mathematical expressions are simply fitted to the observed data. This approach does not take soil physics into account. This is, for instance, the approach followed by in (Topp et al. 1980), where the dielectric constant of mineral soils ε is related to the volumetric moisture content measured using TDR techniques w_s by a third order polynomial:

$$w_s = 4.3.10^{-6}\varepsilon_s^3 - 5.5.10^{-4}\varepsilon_s^2 + 2.92.10^{-2}\varepsilon_s - 5.3.10^{-2} \tag{2.7}$$

This equation has been successfully used by many authors over different soils and even ice, although others have found out that soil moisture content was under- or overestimated. (Ledieu et al. 1986) presented an even simpler empirical relation, by fitting a linear relation between dielectric constant and volumetric moisture content. (Noboroi et al. 2001) offers a complete reference of these studies.

2.1.2.2 Semi-empirical approach

Other models use a semi-empirical (SEM) approach that contains a model of the complex dielectric constant and the volume fraction of each of the soil components. This kind of approach was used by (Wang and Schmugge 1980; Dobson et al. 1985 and Roth et al. 1992). In most cases, the starting point is the dielectric mixing model by (Birchak et al. 1974):

$$\varepsilon_s^\alpha = V_{sp}\varepsilon_{sp}^\alpha + V_a\varepsilon_a^\alpha + V_{fw}\varepsilon_{fw}^\alpha + V_{bw}\varepsilon_{bw}^\alpha \tag{2.8}$$

Where, V_{sp} (ε_{sp}), V_a (ε_a), V_{fw} (ε_{fw}) and V_{bw} (ε_{bw}) are the volume fraction (dielectric constant) of solid phase, air, free water, and bound water in the soil, respectively. The expression in (2.8) can be rewritten as a function of the bulk density and the volumetric moisture as

$$\varepsilon_s^\alpha = 1 + \frac{\rho_b}{\rho_s}(\varepsilon_{sp}^\alpha - 1) + V_{fw}\varepsilon_{fw}^\alpha + V_{bw}\varepsilon_{bw}^\alpha - w_s \tag{2.9}$$

If $\alpha = 0.5$ the model in equation 2.9 is known as refractive model.

The Wang and Schmugge model and the Mironov model consider the effect of bound water on the dielectric constant. They are limited to rather short frequencies of 1-5 GHz and 1-10 GHz, respectively. The Dobson model is valid for a larger range of frequency (1-18 GHz) but it does not differentiate between bound water and free water.

2.1.2.2.1 Dobson et al. model

The semi-empirical mixing dielectric model (SMDM) was developed by Dobson et al. (1985) on the bases of dielectric data covering five soil types, a wide range of moisture conditions, and two frequency ranges extending from 0.3 to 1.3 GHz and from 1.4 to 18 GHz. The SMDM has the following form:

$$\varepsilon_m^{'} = [1 + \frac{\rho_b}{\rho_s}(\varepsilon_s^{'\alpha} - 1) + m_v^{\beta'}\varepsilon_{fw}^{'\alpha} - m_v]^{1/\alpha}, and$$
$$\varepsilon_m^{"} = [m_v^{\beta"}\varepsilon_{fw}^{"\alpha}]^{1/\alpha} \quad (2.10)$$

where $\varepsilon_m^{'}$ and $\varepsilon_m^{"}$ are respectively the real and imaginary parts of dielectric constant of moist soil, $\varepsilon_s^{'}$ is the real dielectric constant of soil solids, m_v is the volumetric moisture content, ρ_b is the bulk density in g/cm3, ρ_s is the specific density of the soil solids. The quantities $\varepsilon_{fw}^{'}$ and $\varepsilon_{fw}^{"}$ are the real and imaginary parts of dielectric constant of free water, which can be calculated with the Debye like dielectric relaxation formulas. The values α = 0:65, $\beta^{'}$, and $\beta^{"}$ are empirically determined constant. To account for moist soil conductivity, the dielectric relaxation formulas were taken in the form

$$\varepsilon_{fw}^{'} = \varepsilon_{w\infty} + \frac{\varepsilon_{w0} - \varepsilon_{w\infty}}{1 + (2\pi f \tau_w)^2}, and$$
$$\varepsilon_{fw}^{"} = \frac{2\pi f \tau_w(\varepsilon_{w0} - \varepsilon_{w\infty})}{1 + (2\pi f \tau_w)^2} + \frac{\sigma_{eff}(\rho_s - \rho_b)}{2\pi\varepsilon_0 f \rho_s m_v} \quad (2.11)$$

where ε_0 = 8.854 * 10^{-12} F/m is the permittivity of free space, *f* is the frequency in Hz, ε_{w0} and $\varepsilon_{w\infty}$ = 4:9 are the low and high frequency limits for the free water dielectric constants, respectively, τ_w is the relaxation time for free water, σ_{eff} is the effective conductivity parameter. Expressions for ε_{w0} and τ_w are given as a function of temperature by Ulaby et al. (1986b). At room temperature (20^0C), $2\pi\tau_w$ = 0.58 * 10^{-10} s and ε_{w0} = 80.1.

All the parameters in equation (2.10) and (2.11), which were empirically determined in (Dobson et al. 1985 and Peplinsky et al. 1995), are presented in the table 2.3, S and C represents in percentage the mass fraction of sand and clay, respectively

Table 2.3: Details of parameters empirically determined by Dobson et al. (1985)

α =0.65	$\varepsilon_s^{'}$ =(1.01 + 0.44 ρ_s)^2 - 0.062	$\beta^{'}$ = (1.275 – 0.519S – 0.152C	$\beta^{"}$ = 1.338 -0.603S – 0.166C
0.3 < f < 1.3GHz	σ_{eff} = 0.0467 + 0.2204 ρ_b - 0.4111S + 0.6614C		
1.4 < f < 18GHz	σ_{eff} = -1.645 + 1.939 ρ_b - 2.25622S + 1.594C		

It is worth noticing that all the SMDM input parameters relating to a given soil type are available from the soil granulometric mineralogy data, which can be borrowed from soil databases. This is a major advantage of the SMDM over many other models, resulting in a wide employment of this model in microwave remote sensing.

2.1.2.2.2 Mironov et al. model

The SEM proposed by (Dobson et al. 1985) has become an effective means to relate soil moisture and microwave dielectric properties (De Roo et al. 2001; Galantowicz et al. 2000 and Jackson et al. 1999). In order to provide for frequency dispersion of the soil dielectric properties, the Debye relaxation formula for the complex dielectric constant (CDC) related to the out-of-soil water is extensively employed in the SEM. At the same time, soil moisture is known to have biphasic dielectric properties (Ulaby et al. 1986b), which usually are correlated to the bound soil water (BSW) and free soil water (FSW). Apparently, the SEM does not account for the dielectric dissimilarities between the BSW and FSW components. Therefore, it appeared not to be applicable to the soils studied in (Sabburg et al. 1997) and (Or and Wraith 1999)1, and the problem of determination of the BSW dielectric properties is still important for the development of moist soil dielectric models.

The first study of the BSW dielectric properties was undertaken in (Wang and Schmugge 1980). Subsequently, CDCs of the BSW and FSW fractions as the separate components of moist soil were obtained in (Mironov et al. 1995 and Mironov et al. 1997). The approach employed was based on the refractive mixing dielectric model (RMDM), initially proposed and validated in (Birchak et al. 1974). At the same time, the RMDM is only capable of making prediction of the soil CDC as a function of moisture for the frequency, for which soil dielectric measurements were carried out.

In contrast to the SMDM, exclusively employing dielectric relaxation spectrum valid for the water located out of soil, the GRMDM suggested in (Mironov et al. 2004) employs the dielectric spectra explicitly related to either bound or free soil water. The description of this concept is given below.

The real and imaginary parts, $\varepsilon_m^{'}$ $\varepsilon_m^{"}$, as a function of volumetric moisture m_v, can be represented in the form of RMDM:

$$\varepsilon_m^{'} = n_m^2 - \kappa_m^2, \varepsilon_m^{'} = 2n_m\kappa_m \tag{2.12}$$

$$\begin{aligned} &n_m = n_d + (n_b - 1)m_v, m_v \le m_{vt} \\ &n_m = n_d + (n_b - 1)m_{vt} + (n_u - 1)(m_v - m_{vt}), m_v \ge m_{vt} \\ &\textit{and} \\ &\kappa_m = \kappa_d + \kappa_b m_v, m_v \le m_{vt} \\ &\kappa_m = \kappa_b m_{vt} + \kappa_u (m_v - m_{vt}), m_v \ge m_{vt} \end{aligned} \tag{2.13}$$

Where n_m, n_d, n_b, n_u and κ_m, κ_d, κ_b, κ_u are the values of refractive index and normalized attenuation coefficient, which is understood here as a proportion of the standard attenuation coefficient to the free space propagation constant. The subscripts *m, d, b* and *u* in (2.12), (2.13) and further on stand for moist soil, dry soil, bound soil water (BSW), and free soil water (FSW), respectively, and m_{vt} is a value of the maximum bound water fraction (MBWF) in a given type of the soil. The latter depends on the soil

mineral contents. The real and imaginary parts for bound, $\varepsilon_b^{'}$ $\varepsilon_b^{"}$,and $\varepsilon_u^{'}$ $\varepsilon_u^{"}$, water components are presented with the Debye relaxation equations

$$\varepsilon_{b,u}^{'} = \varepsilon_{\infty} + \frac{\varepsilon_{b0,u0} - \varepsilon_{\infty}}{1+(2\pi f \tau_{b,u})^2},$$
$$\varepsilon_{b,u}^{"} = \frac{\varepsilon_{b0,u0} - \varepsilon_{\infty}}{1+(2\pi f \tau_{b,u})^2} 2\pi f \tau_{b,u} + \frac{\sigma_{b,u}}{2\pi\varepsilon_0 f} \quad (2.14)$$

In formula (2.14), the value f designates the frequency, while the values $\sigma_{b,u}$, $\tau_{b,u}$ and $\varepsilon_{0b,u}$ are conductivity , relaxation time and low frequency limit dielectric constants, relating to either BWS or FWS components. The value ε_0 is the DC for free space, while ε_{∞} = 4.9 represents the DC in the high-frequency limit for both types of soil water. As can be seen from Equations (39 - 41), a certain type of moist soil, in terms of its dielectric spectra, can be completely determined via a set of the following spectroscopic parameters: $\varepsilon_d^{'}$ and $\varepsilon_d^{"}$, for dry soil; value of maximum bound water fraction, m_{vt}; low frequency limit dielectric constants, ε_{b0} and ε_{u0}, for bound and free soil water; relaxation times, τ_b and τ_u, for bound and free soil water; conductivities, σ_b and σ_u, for bound and free soil water.

The Mironov model for moist soils attained features of physical law and ensured more accurate dielectric predictions, with the soil clay content being an intrinsic texture parameter of the soil.

2.1.3 Soil surface roughness

The effect of soil surface roughness on the brightness temperature has been an issue widely addressed in the literature (Choudhury et al. 1979; Wang and Choudhury 1981; Mo and Schmugge 1987; Wang 1983; Schneeberger et al. 2004; Escorihuela et al. 2007; Wegmüller and Mätzler 1999 and Wigneron et al. 2001). Fung (1994), proposed a theoretical physical model based on surface characteristics derived from the measured soil height profile. A simple empirical roughness model which takes into account only the coherent term of the scattering was reported in (Choudhury et al. 1979).

$$\Gamma_{sp} = \Gamma_{op} \exp(-4k^2\sigma_s^2 \cos^2(\theta)) \quad (2.15)$$

Where, Γ_{op} is the reflectivity at p-polarization (p = v or h) of a smooth surface given by, k = 2π/λ, is the electromagnetic wave number, σ_s is the standard deviation of the surface height, and θ is the incidence angle. This model was reviewed, and another formulation was proposed in (Wang and Choudhury1981)

$$\Gamma_{sp}(\theta) = [(1-Q_s)\Gamma_{op}(\theta) + Q_s\Gamma_{oq}(\theta)]\exp(-h_s \cos^n \theta) \quad (2.16)$$

In this case, two semi-empirical parameters were included to model the effects of the polarization mixing (Q_s), and surface roughness (h_s and n). The dependence of these parameters on surface properties such as correlation length (l_c) or standard deviation of height (σ_s) is not yet clear. (Mo and Schmugge 1987) and (Wigneron et al. 2001) conclude that the n = 2 dependence proposed in (Choudhury et al. 1979) is too strong for L-band. A value of n = 0 at both polarizations was found to be consistent with measurements in

(Wigneron et al. 2001), while Escorihuela et al. (2007) distinguishes n values for both polarizations (1 at horizontal and -1 at vertical).

Similarly, there are discrepancies on the value of the roughness parameter h_s. Some authors obtain h_s from experimental data by best-fit (Wigneron et al. 2001) while others propose expressions for h_s as a function of geophysical parameters. Mo and Schmugge (1987) obtained good results with two parameterizations of h_s as a function of σ^s and l_c.

Finally, there is a general agreement on the value of the cross-polarization parameter Q_s, which has been found to be very small (0 to 0.12) at L-band (Mo and Schmugge 1987 and Wigneron et al. 2001). Apart from these considerations, the effects of frequency and incidence angle on the roughness parameters have not been studied thoroughly. Mo and Schmugge (1987) and Shi et al. (2002) pointed out that the roughness effects depend on both of the frequency and the incidence angle.

Shi et al. (2002) suggested a parameterization of the surface reflectivity derived from data simulated for a wide range of soil water content and roughness properties using the integral equation model (Fung 1994). The surface reflectivity model of Shi et al. (2002) was tested in Schneeberger et al. (2004) and found, not capable of explaining discrepancies between the ground truth and remotely sensed data.

2.1.4 Soil effective temperature

Soil microwave brightness temperature depends on soil emission and on the soil effective temperature, T_{eff} (Ulaby et al. 1986b). The theoretical effective temperature of a soil profile can be estimated as,

$$T_{eff} = \int_0^{\infty} T(z)\alpha(z)\exp[-\int_0^{x} \alpha(z')dz']dz \tag{2.17}$$

Where, T is the thermodynamic temperature, and α is the attenuation coefficient at a depth z. The attenuation is a function of the soil dielectric constant (0), and of the microwave emission wavelength :

$$\alpha(z) = \frac{4\pi}{\lambda}\frac{\varepsilon_s^{"}(z)}{2\sqrt{\varepsilon_s^{'}}(z)} \tag{2.18}$$

Several simple formulations have been developed to estimate the soil effective temperature from soil properties, and soil moisture and temperature profiles. Choudhury et al. (1982) proposed a parameterization of T_{eff} based on the soil temperature at deep soil (T_{∞}) corresponding to a depth between 50 cm and 1 m, and on a ‘’surface" temperature (T_{surf}) corresponding to a depth of 0-5 cm:

$$T_{eff} = T_{\infty} + C_s(T_{surf} - T_{\infty}) \tag{2.19}$$

The coefficient C_s was considered constant for a given frequency, and equal to 0.246 at L-band. On the other hand, Chanzy et al. (1997) presented a model for the soil effective temperature at L- and C-bands based on the air temperature, a deep soil temperature, and the brightness temperature measured at X-band and V-pol.

Wigneron et al. (2001) proposed a parameterization based on equation 2.19, but with a coefficient C_s dependent on the volumetric water content w_s, and two semi-empirical parameters (w_0 and b_{w0}):

$$T_{eff} = T_{\infty} + (T_{surf} - T_{\infty})(\frac{w_s}{w_0})^{b_{w0}} \quad (2.20)$$

Another formulation using the soil dielectric constant instead of the volumetric water content was proposed by Holmes et al. (2006). The performance of equation 2,19 and 2.20, if soil properties such as texture and density were accounted for in the determination of the Cs parameter, is analyzed in Wigneron et al. (2008).

2.1.5 Microwave Emission Models

Charged particles in matter, being in an accelerated motion caused by collisions, can originate electromagnetic radiation. The emission process is reciprocal of absorption. As outlined in (Solimini 2013), this latter consists in the conversion of electromagnetic energy into thermal energy through particle collision. In the reverse sense, a charge accelerated by a collision converts part of its kinetic energy into electromagnetic energy. Microwave remote sensing is based on the measurement of the thermal radiation or brightness temperature of a target, which is determined by its physical temperature and emissivity (1.1.3). The emissivity of land covers depends on soil moisture, but also on soil temperature (Choudhury et al. 1982; Wigneron et al. 2001 and Holmes et al. 2006), soil surface roughness (Mo and Schmugge 1987; Wigneron et al. 2001 and Escorihuela et al. 2007), vegetation canopy (Brunfeldt and Ulaby 1984; Jackson and Schmugge 1991; Ferrazzoli et al. 2002 and Della Vecchia et al. 2006), snow cover (Schwank et al. 2004), relief (Mätlzler and Standley 2000 and Talone et al. 2007), etc.

The emissivity was defined in (1.11). It is the parameter that characterizes the ability of a body to originate electromagnetic radiation by spontaneous emission and that provides important information on the observed surface.

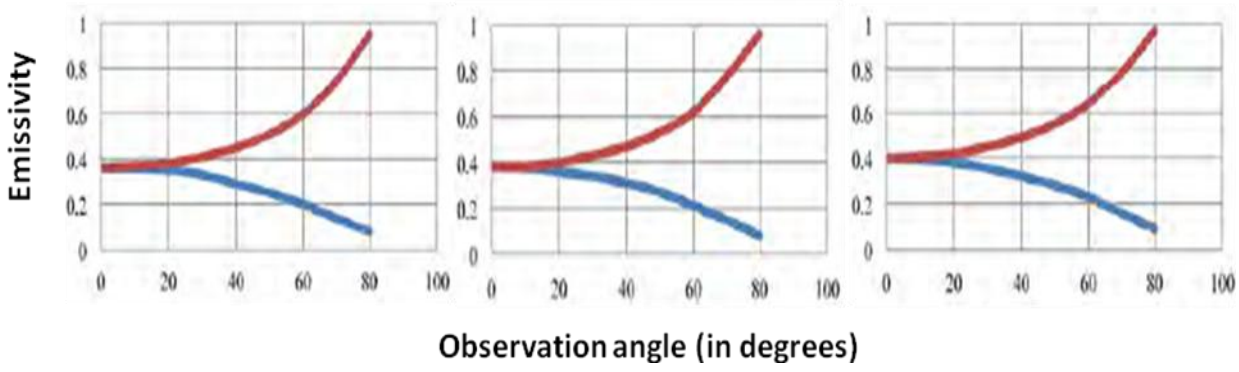

Figure 2.3 : Microwave emissivity of a fresh water at surface at L- (left), C- (middle) and X-band (right). Red curve, v polarization; blue, h polarization

The figures from 2.3 to 2.5, display the microwave emissivities of water and of terrain with ideally smooth surfaces obtained from the simulations (Solimini 2013). These graphs are obtained by data, which was carried out by simply implementing the formula for the reflection coefficient of the half-space with the permittivity of water. These results are approximate, but useful to explain the trend. Although a more precise computation is questionable, since actual data may be changed by

surface roughness. The red curves refer to vertical polarization, while the blue ones are for the horizontal. All diagrams highlight the divarication of the emissivities at vertical and horizontal polarizations as the observation direction departs from the normal to the surface. Figure 2.3, shows that little variations of the emissivity of a smooth water surface can be expected with the frequency, atleast in the range from L- to X-band has. The following figures refer to soil with different moisture contents.

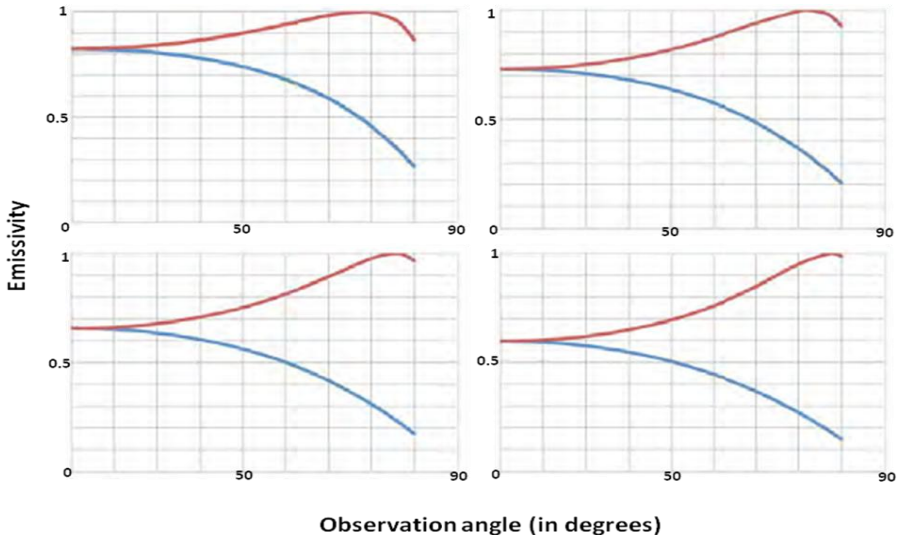

Figure 2.4: C-band emissivity of ideal flat-surface terrain: top left, dry (m_v = 12%); top right, moist (m_v = 21%); bottom left, wet (m_v = 31%); bottom right, very wet (m_v = 35%). Red curves refer to v polarization and the blue curves to h polarization.

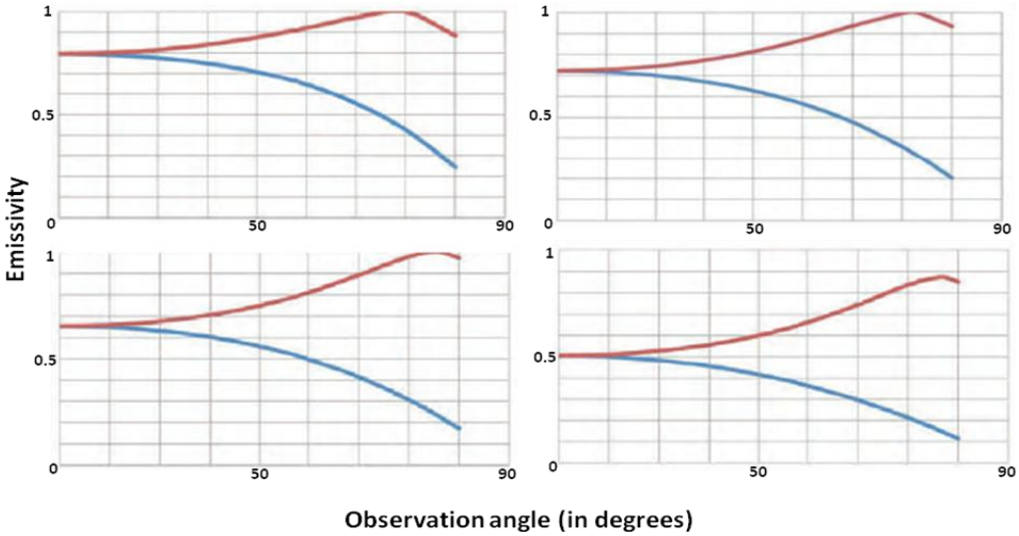

Figure 2.5: L-band emissivity of ideal at-surface terrain: top left, dry (m_v = 12%); top right, moist (m_v = 21%); bottom left, wet (m_v = 31%); bottom right, very wet (m_v = 35%). Red curves refer to vertical polarization, the blue curves to horizontal polarization. Note that $e_v < 1$ at the pseudo-Brewster angle for the wettest soil (bottom right).

Figure 2.4, shows how the C-band emissivity decreases with increasing soil moisture content. The pseudo-Brewster angle, at which the emissivity on vertical polarization is almost unitary, is identified. The angle displaces towards higher values as the moisture content, and hence the permittivity increase.

The decrease of the L-band emissivity with increasing soil moisture shown by the diagrams of Figure 2.5 is more observable than at C-band, because of the slightly larger sensitivity of the permittivity to the amount of water (1.1.5.1). The displacement of the pseudo-Brewster angle is also apparent, as well as the decrease of the maximum emissivity below one for the wettest terrain. Emission from different surface are mentioned in the below sections.

The emissivity of bare soils is given by

$$e_s = 1 - \Gamma_s \tag{2.21}$$

where, Γ_s is the total reflectivity. The rough surface reflectivity consists of a coherent component and an incoherent component.

$$\Gamma_s = \Gamma_{coh}(\theta,\phi) + \Gamma_{inc}(\theta,\phi) \tag{2.22}$$

Γ_{coh} is obtained using formulas of equation (2.21) or (2.22), while Γ_{inc} can be obtained from the integration of the bistatic scattering coefficients of the rough surface. If the roughness of the surface is characterized by the two parameters: the surface height standard deviation σ and the correlation length l_c, then the two components or reflectivity can be written as:

$$\Gamma_{s,p}(\theta_i,\phi_i) = \Gamma_{op}\exp[-h\cos^2(\theta_i)] + \frac{1}{4\pi\cos(\theta_i)}\cdot\sum_{q=H,V}\int_{hemisphere}\sigma^s_{qp}(\theta_i,\phi_i,\theta_r,\phi_r)d\Omega_r \tag{2.23}$$

$h=4k^2\sigma^2$ (k is the wavenumber) and Γ_{op} is the reflectivity of a smooth surface, given by the Fresnel formulation:

$$\Gamma_{oh} = \left|\frac{\cos\theta - \sqrt{\varepsilon_s - \sin^2\theta}}{\cos\theta + \sqrt{\varepsilon_s - \sin^2\theta}}\right|^2,$$
$$\Gamma_{ov} = \left|\frac{\varepsilon_s\cos\theta - \sqrt{\varepsilon_s - \sin^2\theta}}{\varepsilon_s\cos\theta + \sqrt{\varepsilon_s - \sin^2\theta}}\right|^2 \tag{2.24}$$

ε_s is the dielectric constant of soils, which is estimated using a model such as those summarized in Section 2.1.2.

The quantity $\sigma^s_{qp}(\theta_i,\phi_i,\theta_r,\phi_r)$ is the incoherent bistatic scattering coefficient for a wave of polarization p from the incidence direction (θ_i,ϕ_i) scattered into the outgoing direction (θ_r,ϕ_r) with polarization q.

The integration over the entire half space and errors in the modeling of the bistatic scattering coefficients make the computation of equation (2.23) unfeasible or prone to errors. For this reason, the second term is often neglected, and compensated by an adjustment of h parameter.

2.2 Vegetative Soil

If the remote sensor is placed above a canopy looking downwards, the measured brightness temperature will contain not only information on the soil, but also on vegetation, since vegetation radiates its own energy and, moreover, attenuates and scatters the soil radiation The common practice is to use approximate formulas or semi-empirical models in which the different components of the brightness temperature could be differentiated. The emissivity of a soil covered by vegetation is usually estimated as the contribution of three terms: (i) the radiation from the soil that is attenuated by the overlying vegetation, (ii) the upward radiation from the vegetation, and (iii) the downward radiation from the vegetation, reflected by the soil, and attenuated by the canopy (Ulaby et al. 1986b)

$$T_{Bp}^{model} = (1+\frac{1-e_{bs}}{L_{veg}})(1-\frac{1}{L_{veg}})(1-\omega)T_{veg} + \frac{e_{bs}}{L_{veg}}T_{soil} \quad (2.25)$$

where e_{bs} is the emissivity of a bare soil, T_{veg} and T_{soil} are the physical temperatures of the vegetation and soil, respectively, $L_{veg} = \exp(\tau \sec \theta)$ is the attenuation due to the vegetation cover. τ is the optical thickness of the standing vegetation cover, which includes both green and senescent vegetation materials. τ is usually found to be correlated to Volumetric Water Content (VWC), but it is difficult to provide estimate of this latter variable at global scale. In some semiempirical models, the optical thickness is expressed by a simple formula, such as, $\tau = b.VWC$, b is a coefficient (Van de Griend and Wigneron 2004), and VWC is the vegetation water content. ω is the single scattering albedo. This formulation is based on the single scattering approach proposed in Kirdiashev et al. (1979). The b coefficient depends on the polarization and the frequency. The single scattering albedo describes the scattering of the emitted radiation by the vegetation and is a function of frequency and plant geometry. Equation (2.25) is a simplified version of the general Radiative Transfer Equation, which is summarized in Appendix A.

In the SMOS forest algorithm, τ is parameterized as a function of the Leaf Area Index (LAI). There are two main reasons for this: (i) it is much easier to build global maps of LAI from spaceborne remote sensing observations in the optical domain or from modeling with interactive vegetation (Wigneron et al. 2002) than maps of VWC; (ii) several recent studies have also found good correlation between τ and LAI (Saleh et al. 2005) over a fallow and over several crops. It is likely the parameterization of τ from LAI, rather than from VWC, will be rather efficient as long as the vegetation is green (in particular during the vegetation growth). This parameterization might be less accurate during the senescence phase (during which τ might be underestimated from low LAI values over some vegetation types). And so the correct value of LAI is essential for the model.

2.3 Soil moisture retrieval algorithms

The PhD thesis focus on identifying the inundated areas using measurements of T_B obtained from AMSR-E mission and improving soil moisture retrieval algorithm over forests within the SMOS mission. The brightness temperature of land covers is influenced by many variables, the most important being soil moisture and temperature, and vegetation characteristics. The challenge is to reconstruct the environmental parameters from the measured signal by using a minimum of ancillary data. To do this, different soil moisture retrieval algorithms have been developed. Some of them were summarized in the review by Wagner et al. (2003). Broadly it can be put into three major groups. The first one is based on

the experimental relationship between the geophysical variables and the radiative transfer equation using a regression technique. This approach has limited applicability, since often the regression is valid only for the test sites where they were obtained. The second approach is based on the use of neural networks. These algorithms have been used with satisfactory results in the retrieval of agricultural parameters from radiometric data (Del Frate and Wang 2001 and Del Frate et al. 2003), but need a training phase that is not always feasible. And the third type of algorithms, which is more widely used, is based on the inversion of radiative transfer models. The soil moisture models are used as forward models, and the geophysical variables are retrieved by minimization of a cost function (Parde et al. 2004 and Saleh et al. 2006a). This approach has also some disadvantages, since errors of the model can lead to errors in the retrieval. The expression of the Cost Function is:

$$F = \sum_{0} \frac{(T_{Bh} - T_{Bh}^{meas})^2 + (T_{Bv} - T_{Bv}^{meas})^2}{\sigma_{T_B}^2} + \sum_{n} \frac{(P_n^{ini} - P_n)^2}{\sigma_{P_n}^2} \tag{2.26}$$

Where the simulated brightness temperature T_{Bp} is computed using a land emission model. T_{Bh}^{meas} is the measured brightness temperature, and P_n is any of the parameters on which T_{Bp} depends. A first-guess value of the parameters P_n (P_n^{ini}) with associated standard deviation σ_{P_n} can be also considered in the cost function. Estimates can be constrained to be close to the initial value by choosing low σ_{P_n} values, or they can be left as a free parameter by selecting σ_{P_n} >>1.

Algorithms considering various other factors have also been proposed to retrieve soil moisture content from passive microwave remote sensed data. (Jackson et al. 1993), developed a so-called single channel algorithm (SCA), in which the brightness temperature of the 6.9 GHz horizontal polarization channel was used. In this algorithm, ancillary data such as air temperature, land cover, Normalized Difference Vegetation Index (NDVI), surface roughness, and soil texture and porosity are needed. The algorithm of Njoku and Entekhabi (1996) and Njoku et al. (2003), is a multiple channel iterative retrieval algorithm. It uses the brightness temperature observed by the lowest six channels of AMSR-E. Using this algorithm, the surface temperature, the vegetation opacity and the soil moisture are estimated simultaneously. The algorithm proposed by Paloscia et al. (2006), is an experiment-based linear regression retrieval, in which soil moisture is estimated by using both 10.7GHz and 6.9GHz channels.

After more than 20 years effort, good results were obtained and several global and continental scale soil moisture datasets (Njoku et al. 2003 and Owe et al. 2008) were generated. But both the quality and the spatial extension of these algorithms must be further improved. For example, Shibata et al. (2003) pointed out that the soil moisture in desert regions retrieved from AMSR-E soil moisture algorithms indicate very wet areas. To solve such problem, the Radiative Transfer Model (RTM) should be improved firstly.

3 Flood Monitoring using Microwave Passive Remote Sensing (AMSR-E) in part of Brahmaputra basin, India

3.1 Introduction

Floods are one of the most recurring, widespread and disastrous hazards of the world, both natural and man-made in origin. On the world flood map, India is only preceded by Bangladesh and among the major rivers basins of India, Brahmaputra basin and floods are almost synonymous to the world. Every year thousands of acres of land remain under water for most part of the year in this region. One of the important causes for frequent occurrence of flood in this region is the extremely dynamic monsoon rainfall regime in the backdrop of the unique physiographic setting. Also, the water yield of the Brahmaputra is among the highest in the world. These factors, together with high sediment yield, limited width of the valley and the abruptly flattened gradient, leads to tremendous drainage congestion and resultant flooding. The scenario is further exacerbated by a myriad of social, economic and environmental factors causing increased vulnerability of people to the flood hazard

Monitoring of global phenomenon such as flood using satellite data is important for assessing the damage caused by flood. Also it can lead to a better understanding of the global water cycle and its role in climate change. Over the past decade, several flood monitoring/forecast methodologies, based on remote sensing data, have been proposed as described in Section 1.2.2. Among them, the ones based on microwave observations have a better success rate since large flood events and intense cloud covers are often encountered simultaneously. Furthermore, since flood events are dynamic processes, higher temporal resolutions are required even if this leads to lower spatial resolutions. Therefore, passive microwaves are often exploited. This is particularly true in the case of large river basins, where extreme flood events compromise thousands of square kilometres in a matter of few hours.

Earlier work carried out by Singh et al. (2008) and Dutta et al. (2010) has also discussed the necessity of flood mapping and a detailed hydrodynamic investigation to simulate the flood behaviour and the flood propagation in the low lying flood plain in the proposed study area.

Rainfall measurement over land is another crucial element for understanding the water cycle exchange between land and atmosphere. Precipitation has a very high correlation with the soil moisture. However it is very difficult to find a direct way to study these two variables with respect to each other as rainfall is the main source of uncertainty in retrieval of soil moisture (Jin et al. 2006). In fact, the microwave signals gets highly affected when they pass through a raining atmosphere, which results in incorrect estimation of soil moisture in the footprint of the satellite. For global rain identification, (Grody 1991) developed a set of rules to separate rain from snow and deserts. Ferraro and Marks (1994) expanded on those ideas and developed a more expansive set of screens to be used for rainfall retrievals that included separate indices for land and ocean, improved screens for semi-arid land, coastlines, and sea ice, as well as some discussion on the uncertainties related to each screen.

As stated in Section 1.4.1, the Advanced Microwave Scanning Radiometer (AMSR-E) of the Earth Observing System (EOS), developed by the National Space Development Agency of Japan (NASDA) and provided to the U.S. National Aeronautics and Space Administration (NASA) for launch on its Aqua satellite, can be a valid instrument for flood monitoring. The AMSR-E instrument operates at multiple frequencies, ranging from 6.9 GHz – 89.0 GHz. The antenna scans conically at a fixed incidence angle of

55^0 across a 1445 km swath, providing near-global coverage in two days or less.

In this Chapter, the use of multifrequency AMSR-E signatures in floods monitoring is tested over the Indian Brahmaputra basin. The temporal evolution of parameters defined in the literature, such as F_{WS}, and PI is analyzed, and results are compared against available ground measurements of river water level. Techniques aimed at eliminating images affected by heavy rainfalls are also investigated.

The proposed monitoring techniques can be extensively tested and exploited in the future years. Although AMSR-E automatically spun down in Oct 2011, AMSR2 sensor, a slightly modified and improved version of AMSR-E, mounted on Japan's GCOM-W satellite (Imaoka et al. 2010), is already providing data. TRMM data which acquires data through multi-channel passive microwave radiometer including the one at 19 GHz, can also be exploited to understand the effect of heavy rainfall on the brightness temperature (T_B) values. The current study will also add upon the existing operational Global Disaster Alert and Coordination System (GDACS) web site for flood mapping even during high rain storms.

3.2 Study Area

3.2.1 General properties

In this work, critical sites in and around Lakhimpur District in Assam, falling within the Brahmaputra basin, often characterized by high frequency of flooding events, were considered. A map of the area is shown in Figure 3.1**.** It is bounded between 26°48' and 27°53' northern latitude, and 93°42' and 94°20' eastern longitude. The sites are mostly agricultural with paddy fields. One site falls on the River Subansiri, whereas the other two fall on the Brahmaputra. The total area is around 2277 km^2 out of which, 2257 km^2 is rural and 20 km^2 is under urban area. Agriculture is the mainstay of the district's economy. Almost 67% of the Gross Cropped Area (GCA) is covered by paddy crop. Livelihood of more than 80% people is solely dependent on agriculture. Major part of GCA is covered by Kharif season crops (May-August), followed by Rabi season crops (December-February). Rice, jute, mustard, wheat, pulses are the principal field crops in the district. Fruits and vegetables also constitute an important part of the agriculture produce in the district. Detailed information is made available by Govt. of India (2004).

Timely information about floods provide strong indicators of a forthcoming disaster, but owing to the unpredictability of the behaviour of the Brahmaputra River and with increased incidences of anthropogenic activities on it, real time estimations of the aftermath will help to reduce, manage and control the increasing extent of the disaster. Also, a major pool of both finance and research are being channelled towards forecasting floods in this valley with little or few results towards actually monitoring and managing the floods and its repercussions. This calls for a different approach to handle such a natural disaster. Hence real-time monitoring and analysis of such a recurring and phenomenal hazard is essential.

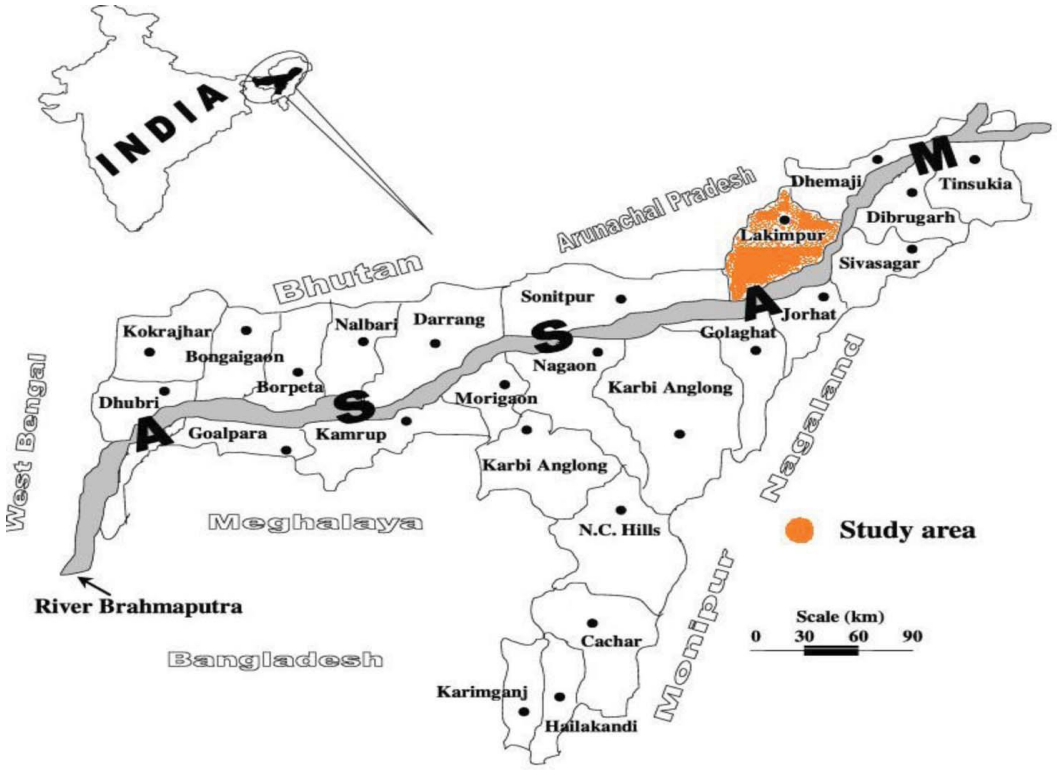

Figure 3.1: Study area: Lakhimpur District, Assam, India

3.2.2 Regional Hydrology

3.2.2.1 The River System

The Brahmaputra: Undoubtedly the most dynamic and awe-inspiring rivers of India, Brahmaputra, has a few unique characteristics. It is fed by numerous tributaries, rivulets and streams. Added to all these are the wide and divergent braids of the Brahmaputra and meanders which issue from it, resulting into an intricate maze of water bodies spread not merely across the valley, but also enclosing it. The Brahmaputra is fed on its course through the valley by no less than 57 tributaries on its North bank and 33 on its South. Out of the total Northeast region area of 2.25×10^6 km^2 the Brahmaputra drainage system covers an area of a massive 1.75×10^6 km^2. Most of its 1.75×10^6 km^2 area receives an average annual rainfall of nearly 200 cm. The maximum discharge of the river at Dhubri (from where it enters Bangladesh) is 19821 m^3 s^{-1}.

The Brahmaputra River is the southern boundary of North Lakhimpur district and touches all along the southern and southeastern boundary. The Brahmaputra behaves as a braided channel near Lakhimpur and the adjoining Dhemaji district. The alluvial deposits within the main channel lead to sideward migration of the banks. Therefore, besides the flood problem of the Brahmaputra, intensive bank erosion is another problem during floods in these areas (Govt. Of India 2012)

The Subansiri: The Subansiri is the largest tributary of the Brahmaputra and originates in the south of Po Rom peak (5059 m) and enters Assam through Arunachal Pradesh. Its total length is 520 km and it drains a basin of 37,000 km^2. The river maintains an almost stable course but becomes unstable as soon as it enters the alluvial plains of Assam in North Lakhimpur. In the10 km reach from the foothills near Gerukamukh to Chauldhuaghat, the riverbed is composed of sand mixed with pebbles and boulders.

Further downstream, it is mostly composed of sand. The average slope of the river bed from the foothills to Chauldhuaghat and to the confluence of Ranga River is about 24 cm km^{-1} (0.00024). The river banks from the foothills to Chauldhuaghat are composed mostly of sand, gravel and silt, beyond which they are composed almost exclusively of alluvial silt.

The mean daily discharge of Subansiri at Gerukamukh is 138842 m^3 s^{-1} (Govt. Of India 2012). The average annual sediment yield at Chauldhuaghat is 94.83×10^6 kg (WAPCOS 1993). No significant anthropogenic effect has been identified on the sediment or channel of the main river. The river discharges 5936 m^3 s^{-1} of water at Bhimpara Ghat.

The Ranganadi: The River originates from the Dafla hills of Arunachal Pradesh. The total length of the river is 145 km and total catchment area is 2173 km^2 in Arunachal Pradesh and 767 km^2 in Assam. It discharges 496 m^3 s^{-1} water at 3.2 km upstream of National Highway 52.

The Dikrong: The Dikrong also has its origins from the Dafla Hills of Arunachal Pradesh. In Arunachal Pradesh it is known as Par Nadi. It enters the plains near Harmutty Tea Estate and runs 40 km to join the Brahmaputra at Badati. It discharges 566 m^3 s^{-1} of water at 1.6 km downstream of National Highway 52. The catchment area of the river is 1326 km^2 in Arunachal Pradesh and 262 km^2 in Assam.

The causes of flood in Lakhimpur District can be attributed to excessive rainfalls in Assam and Arunachal Pradesh, melting of snow at Tibet and bursting of natural dams formed by the landslides on the rivers flowing from Arunachal Pradesh. During flood the river gets charged with enormous quantity of silt and in their movement of the river alters the conditions of flow and sometimes changes the river course causing havoc in its low-lying basin.

3.3 AMSR-E Observations

AMSR-E/Aqua global swath brightness temperatures (L2A) data was used in this study for obtaining the brightness temperature (T_B) and the Polarization Index (PI). The resolution of the AMSR-E data at C band, X band and K_a bands is (43 × 75 km), (29 × 51 km) and (8 × 14 km) respectively. In this work, for each band the product with the best available resolution was selected. Data was interpolated at each band to resample it at same interval. The interpolation interval was taken as half a minute of degree. Radiometric signatures were aggregated at the 6 × 6 km resolution on the EASE-Grid geographical projection. The data was captured for three specific sites within the study area viz., Dhalghat (27°06' and 27°18' , 94°06' and 94°18'), Ghansari (26°48' and 27°00' , 94°06' and 94°18') and Jamugurihat (26°30' and 26°42' , 92°42' and 92°54'). Dhalghat and Jamugurihat sites falls within the Lakhimpur District, where as Ghansari falls in Jorhat District. For each site, the mean value of the above interpolated data within a box of the 12' by 12' (sampling interval in minute) has been considered.

3.3.1 Dynamic ranges of emissivity at vertical and horizontal polarization

The emissivity at Horizontal (*H*) and Vertical (*V*) polarization was derived from the T_B measured by AMSR-E and the ground surface temperature provided by Indian Meteorological Department (IMD). Separately, emissivity was calculated for 10.65, 18.7 and 36.5 GHz frequencies at both polarizations. These three frequencies behave differently when interacted with the atmosphere, clouds and vegetation. Comparative analysis was carried out to find the relationship between vertical and horizontal emissivity at 10.65, 18.7 and 36.5 GHz. Dhalghat site was chosen and the year 2007 was selected. Results are shown in Figure 3.2. The regression equations between horizontal and vertical polarization at the three frequencies are:

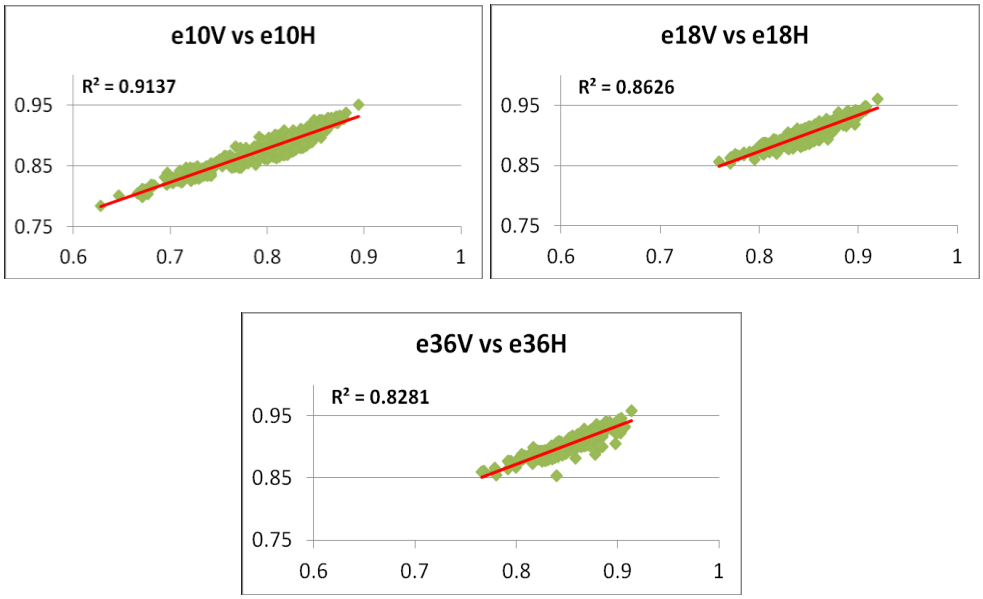

Figure 3.2: Relationship between emissivities at $H(e_H)$ and $V(e_V)$ polarization at 10.65, 18.7 and 36.5 GHz for Dhalghat Site (2007)

$$\begin{aligned} 10GHz: e_{10V} &= 0.556 \times e_{10H} + 0.4345, R^2 = 0.9137 \\ 18GHz: e_{18V} &= 0.6018 \times e_{18H} + 0.3919, R^2 = 0.8626 \\ 36GHz: e_{36V} &= 0.6123 \times e_{36H} + 0.3824, R^2 = 0.8281 \end{aligned} \quad (3.1)$$

where, e_{10V} (H), e_{18V} (H) and e_{36V} (H) are the emissivities at 10.65, 18.7 and 36.5 GHz , and at vertical (V) and horizontal (H) polarization, respectively. Almost similar results are obtained at Ghansari and Jamugurihat sites in the study area. Since the data samples consist of the whole year data, which includes the monsoon season data as well, we can consider that the variation in the emissivity ranges from pixels with high flood effect to pixels with little or no flooding. The equation (3.1) relationships are similar to the ones found by Fily et al. (2003), who obtained

$$\begin{aligned} e_{19V} &= 0.562 \times e_{19H} + 0.434, and \\ e_{37V} &= 0.502 \times e_{37H} + 0.484 \end{aligned} \quad (3.2)$$

in his study over North America. Matzler, (1994), obtained

$$e_{10.4V} = 0.46 \times e_{10.4H} + 0.52 \quad (3.3)$$

from ground measurement in the Alps. Goita and Royer (2002), who found,

$$\begin{aligned} e_{19V} &= 0.560 \times e_{19H} + 0.428, and \\ e_{37V} &= 0.597 \times e_{37H} + 0.401 \end{aligned} \quad (3.4)$$

using satellite data over northern Quebec in Canada. Other studies also found that emissivity variations

are related to various changes of surface properties. Basist et al. (1998) found that the variation in the emissivity at horizontal polarization is mainly due to the presence of water in the pixel, when T_B is computed in the microwave range. Other studies (Griddings and Choudhury 1989 and Sippel et al. 1998) also suggest that the microwave emissivity is strongly affected by the percentage of water bodies in the observed pixels even in vegetative areas. The emissivity of water is low when compared to the other objects existing on the earth surface (Prigent et al. 1997). The emissivity is also affected by the soil moisture effect for few centimeters inside the surface (Owe et al. 1999 and Vinnikov et al. 1999)) and by the vegetation (Prigent et al. 2001). Brakenridge et al. (2007b), proposed a "discharge estimator" based on K_a band AMSR-E data, which was successfully tested over several rivers worldwide. The high frequency channel was selected for spatial resolution issues, and vegetation effects were considered negligible in the selected sites.

In our case, since the surface was covered by permanently flooded paddy fields, the dynamic range of emissivity is mostly due to variations of water level within the fields, partially correlated with variation in water level of the river. The diagrams of Figure 3.3 indicate that 10.65 GHz has better dynamic range of emissivity at both *H* and *V* polarization compared with 18.7 and 36.5 GHz. This last frequency shows further limitations, related to raindrop effects, as will be shown in next Sections. In agreement with previous studies, *H* polarization shows a better dynamic range, at all frequencies.

Lower frequency channels at C and X bands can suffer from radio frequency interference (RFI). But after applying algorithm of spectral difference indices (Njoku et al. 2005), for the year 2007, we found that our study area was not affected by RFI at X band.

3.3.2 Polarization Index

Fresnel equations and energy conservation law were introduced in section 2. According with these principles, the microwave emission from a homogeneous medium with a smooth surface observed at off-nadir angle is partially polarized, since the vertical component of T_B is higher than the horizontal one. The polarization difference T_{BV}-T_{BH} depends on the permittivity of the medium and is maximum at Brewster angle. It is reduced if the soil is dry, or rough, or is covered by vegetation. The emission from a terrain depends on surface temperature, but the polarization property of the emitted radiation is independent from it. This property can be exploited by normalizing the polarization difference to the average value of T_B at *V* and *H* polarization. The polarization Index PI is defined as (Paloscia and Pampaloni 1988):

$$PI = \frac{T_{BV} - T_{BH}}{0.5(T_{BV} + T_{BH})} \tag{3.5}$$

where, T_{BV} and T_{BH} are the brightness temperature at vertical and horizontal polarizations, respectively. Due to the normalization, the change in the value of PI can be attributed to the surface features. The results were evaluated at C, X and K_a bands of AMSR-E. PI multitemporal trends were compared against variations of water level (WL) within the river. The data for WL was provided by the State Water Resource Department, Lakhimpur, Assam, India. They collected WL at Dhalghat (DG), Ghansarai (GH) and Jamugurihat (JG) sites. DG readings were measured on Subansiri River, which is also a major tributary of River Brahmaputra, where as GH and JG readings are taken on Brahmaputra River itself. For each day, three water level values were measured (morning, noon and evening). Depending on the pass of AMSR-E data, WL values were taken viz., morning WL value for ascending pass and evening value for descending pass. Geographically, DG is at a higher slope compared to GH and JG. Figure 3.3, shows the variation of PI over the whole Julian days of 2007 at different frequencies on all the three sites. Baring few exceptions at JG, on all the sites, the values of PI at X band is observed to be lower from January till

early April and then from November till December end whereas, from mid June till late September, the PI values are at the higher side, which coincides with the monsoon period in the region. The observation at C and K_a band basically follow the same pattern, but they also show irregular variations which may be due to the effects of radio frequency interferences (RFI) at C band and rain drop effect, at K_a band.

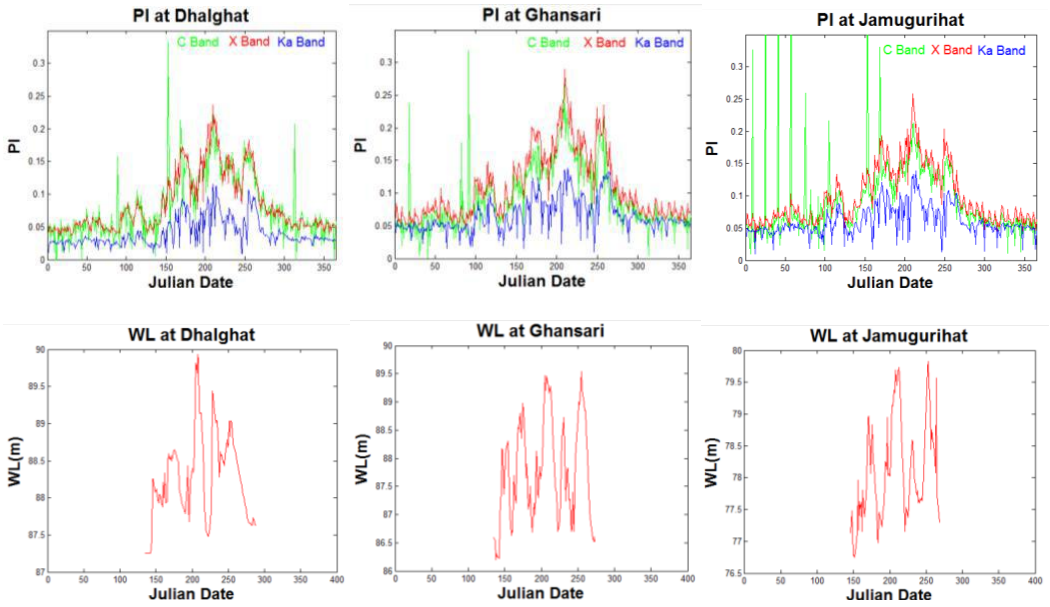

Figure 3.3: Upper figures: PI (C, X and Ka band) vs Julian Date of 2007 for Dhalgat, Ghansari and Jamugurihat sites. Lower figures: corresponding trends of Water Level (WL).

Some specific days from pre-monsoon to monsoon and post-monsoon seasons for the year 2007 were also analyzed. The analysis was carried out for DG site. Maximum and minimum values of the emissivity (within the box) and average PI are reported in Table 3.1 for X and K_a band. The selection of the days was based on their variability in terms of rain fall and flood conditions viz., 29/06/2007 (no rains but flood), 15/07/2007 (Rains but no flood), 31/07/2007 (Rains and flood), 25/08/2007 (No rain but flood) and 10/09/2007 (very slight rain but flooded) (Table 3.2). It can be observed that there is rise in the PI with the increase in the WL at both bands, but on a high rain fall day (viz., 15/06/2007) the PI value at 36.5 GHz is dropped significantly. The rain drops effect on PI values has been discussed in detail in section 3.5 of the paper.

Table 3.1: Minimum and maximum values of emissivities, and average PI values, on selected dates at X and Ka bands.

Date	Freq (GHz)	WL(m)	Rain(mm)	e_V mean	e_H mean	PI
29/06/2007	10	88.5	0	0.8477	0.7647	0.1030
	36			0.8907	0.8358	0.0636
15/07/2007	10	87.68	67	0.8542	0.7820	0.0882
	36			0.8496	0.8437	0.0069
31/07/2007	10	89.16	10	0.8235	0.7190	0.1354
	36			0.8883	0.8077	0.0951
25/08/2007	10	88.4	0	0.8680	0.7973	0.0849
	36			0.9007	0.8519	0.0557
10/09/2007	10	89.15	07	0.8345	0.7344	0.1275
	36			0.8933	0.8232	0.0817

Table 3.2: Cumulative distribution of F_{WS} calculated at specific days using X band T_B values and surface temperature data provided by IMD.

Date	90%	80%	70%	60%	50%
15/07/2007	5.319149	17.02128	26.06383	36.17021	47.34043
31/07/2007	13.29787	22.87234	30.31915	38.29787	47.87234
25/08/2007	12.79621	21.80095	29.85782	38.38863	42.18009
10/09/2007	10	19.04762	25.2381	30	38.09524

3.3.3 Fractional Water Surface

To a first-order approximation, the satellite measured T_B over land is a product between the emissivity and the surface temperature, and is given in 1.1.3.

$$T_{BP} = e_P \times T_S \tag{3.6}$$

e_P is the emissivity at P (vertical or horizontal) polarization, T_{BP} is brightness temperature at P polarization and T_S is the surface temperature. This formula neglects atmospheric contributions. Over land the T_B variations observed by the AMSR-E sensor in the frequency range of 6–37 GHz are primarily controlled by the underlying surface, except when precipitating clouds are present. This is due to the rather high emissivity of the land surface, and the transparency of clear atmosphere in most microwave bands. Although the atmosphere contributes to the satellite-measured T_B, its contributions are generally lower than 10% of the observed variability in the absence of precipitation at all frequencies, except the absorption lines of water vapor and oxygen (National Research Council 1999 and Ferraro et al. 1998).As recalled in 3.3.1, when the frequency increases, the dynamic range of T_B decreases. The T_{BP} obtained from AMSR-E data is used to find the emissivity e_P, as the surface temperature is known from IMD data. IMD provided hourly T_S data needed to obtain emissivity on the surface during both ascending and descending passes of the AMSR-E. The obtained emissivity is used to find out the fractional water surface F_{WS} (Fily et al. 2003), defined as

$$F_{WSP} = \frac{(e_P - e_{Pdry})}{(e_{PW} - e_{Pdry})} \tag{3.7}$$

e_{Pdry} is the emissivity of dry surface and e_{PW} is emissivity of water. Multitemporal trends of F_{WSH} and F_{WSV} at X and K_a band obtained over DG site are shown in Figure 3.4. The trends indicate that the horizontally polarized emissivity is slightly more sensitive to surface effects than the vertically polarized emissivity. Moreover, it can be observed that the dynamic range of emissivity in case of lower frequencies is wider compared to the higher ones. This result is expected, since vegetation attenuation increases with frequency.

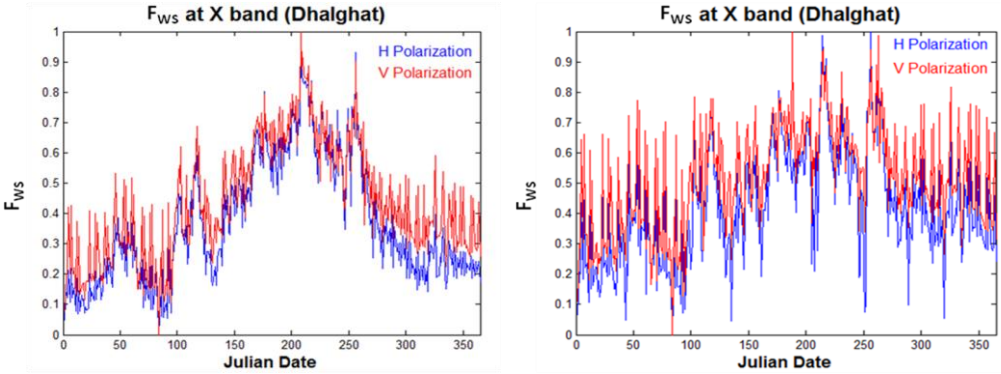

Figure 3.4: Temporal trend of F_{WS} at *H* and *V* Polarization as a function of Julian Date of 2007. Left: X band. Right: K_a band.

The entire basin was also considered and the cumulative distribution was computed. Results are shown in Table 3.2. The probability to have $F_{WS} \geq 0.9$ changes from 5% on 15/07/2007 (before Monsoon) to 13% on 31/07/2007 (during Monsoon). To interpret the results, we must consider that the study area also comprises of rivers, lakes ponds and wetlands/marshy lands, which in total account for nearly 5% of the total area. If that is considered as a benchmark, we can conclude that the increase in the percentage of F_{WS} for the values above 0.9 may be due to the flooding in the region. The average of WL data collected from three sites falling at three locations in the area shows a general correlation with F_{WS}. In general F_{WS} is found to be a useful indicator in flood monitoring as it depicts the variation of flooded areas in both space and time.

It can be also observed that with the increase in the WL the cumulative distribution of F_{WS} shifts towards higher values, but the decrease in WL does not decrease the F_{WS} in the same ratio. This is due to the fact that the flooding in the area is mostly due to breaching of the embankment made along the river and not just due to increase of WL in the main river. Due to this, even after the decrease in WL in the river, water gets blocked due to the remaining embankment height and as such it remains in the area for long.

3.4 Correlations with ground truth

3.4.1 General considerations

F_{WS} is a useful parameter to monitor variations of soil moisture associated to flooding. In the area of this experiment, the land was mostly covered by permanently flooded paddy fields, so that variations of emission properties were related to vegetation submerging, rather than soil moisture variations. So, as such the representation of F_{WS} is not the best suited one to monitor the flood effects in the area. This reflected in the figures and correlation obtained by comparisons with ground data in the sections below. F_{WS} was calculated only at DG site, for which Surface Temperature data was available.

3.4.2 Fractional Water Surface FWS vs Water Level WL

F_{WS} at both polarizations was calculated and compared with the WL at DG site. At 10.65 GHz, the horizontal polarization shows a better correlation with the WL as compared to the vertical polarization, but both correlation coefficients are lower than 0.4. The results are poor for 36.5 GHz at both polarizations (correlation coefficients less than 0.1).

3.4.3 Polarization Index (PI) vs Water Level (WL)

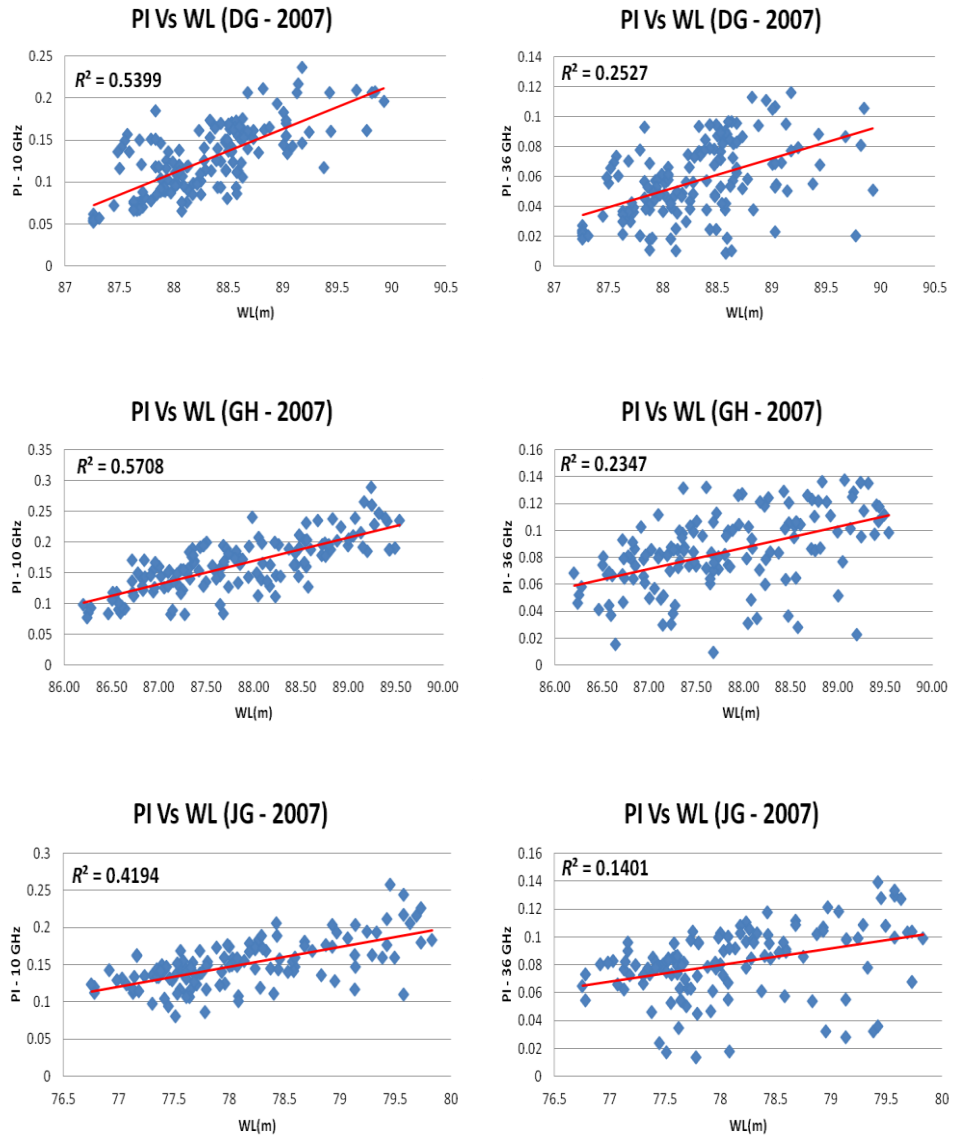

Figure 3.5: Scatterplots of Polarization Index (PI) vs. Water Level (WL) for Dhalgat, Ghansari and Jamugurihat sites. Left: 10.65 GHz. Right: 36.5 GHz.

In order to evaluate more specifically the trends of PI as a function of WL, the three locations have been considered. The trends of PI vs. WL, at X and K_a band, are shown in Figure 3.5. 36.5 GHz is affected by raindrop effects, during rainfalls, and high vegetation attenuation, which even reduces the dynamic range. PI is better correlated with variations of water level, with respect to F_{WS}. This result finds explanation in the particular characteristics of the considered sites. They are dominated by paddy fields. A moderate flooding produces an increase of soil moisture, while intense flooding produces a reduction in the emerged height of vegetation. As demonstrated by previous studies (see, e.g. Paloscia and Pampaloni (1988), the PI at X band is sensitive to both effects. Therefore, it is an effective indicator of both moderate and intense flooding for regions dominated by paddy vegetation.

3.5 Effect of falling raindrops

As mentioned in section 3.2, there was a significant drop in the PI value on the day when a high rain fall was recorded. It was confirmed by the precipitation data (see Table 3.1). To get an insight into this effect, further comparisons were made between rainfall data and PI. Multitemporal trends of rainfall, water level and PI are reported in Figure 3.6. At K_a band, on some days in which there was heavy rain fall, there is sudden drop in the values of PI (see, e.g. Julian days 151, 159, 167, 190, 197, 208, 206, 229, 246, 253 in Figure 3.6 (a), whereas on a rain free days the PI basically follows the WL trends. The drops are often observed even at X band, although to a lesser extent (Figure 3.6 (b)). In figure 3.6 (c), it can be seen that WL increases with the increase in precipitation.

In order to evaluate the performance of the algorithm proposed by (Ferraro et al.1998) in this basin, results of specific days were investigated. Subsequently, identification and elimination of rain affected samples was applied using 23.8 GHz and 89.0 GHz channels of AMSR-E data. Examples of images not affected and affected by raindrops are reported in Figure 3.7 (a) and (b), respectively. F_{WSH}, F_{WSV} and PI are mapped at both X and K_a band for two specific dates: Day 179 (29/06/2007, without rain) and Day 196 (15/07/2007, with rain). The area was bounded in a 26°30' and 27°42', 93°30' and 94°42' box. Data was interpolated in same way to resample it at equal interval, 12' by 12' (sampling interval in minute). In absence of rain (Figure 3.7 (a)) the maps are consistent. Higher values of both F_{WSH}, F_{WSV}, and PI are observed along the river at both frequencies, although with different extent. In the rainy day (Figure 3.7 (b)), the spatial patterns at 36.5 GHz show anomalies, particularly for F_{WSH} and F_{WSV}. The selection of dates was made based on similarity in flooding condition over the area. The anomalies are due to the high sensitivity of K_a band to raindrops effects, with respect to X band.

3.6 Rain pixels elimination

To get over from the rain drop problems, the screening method proposed by (Ferraro et al. 1998) was used. Due to different climatic conditions, the current algorithm used slightly different threshold values for AMSR-E channels, based on the plot showing the difference between T_{BV} at 23.8 GHz and T_{BV} at 89.0 GHz vs. T_{BV} at 89.0 GHz.

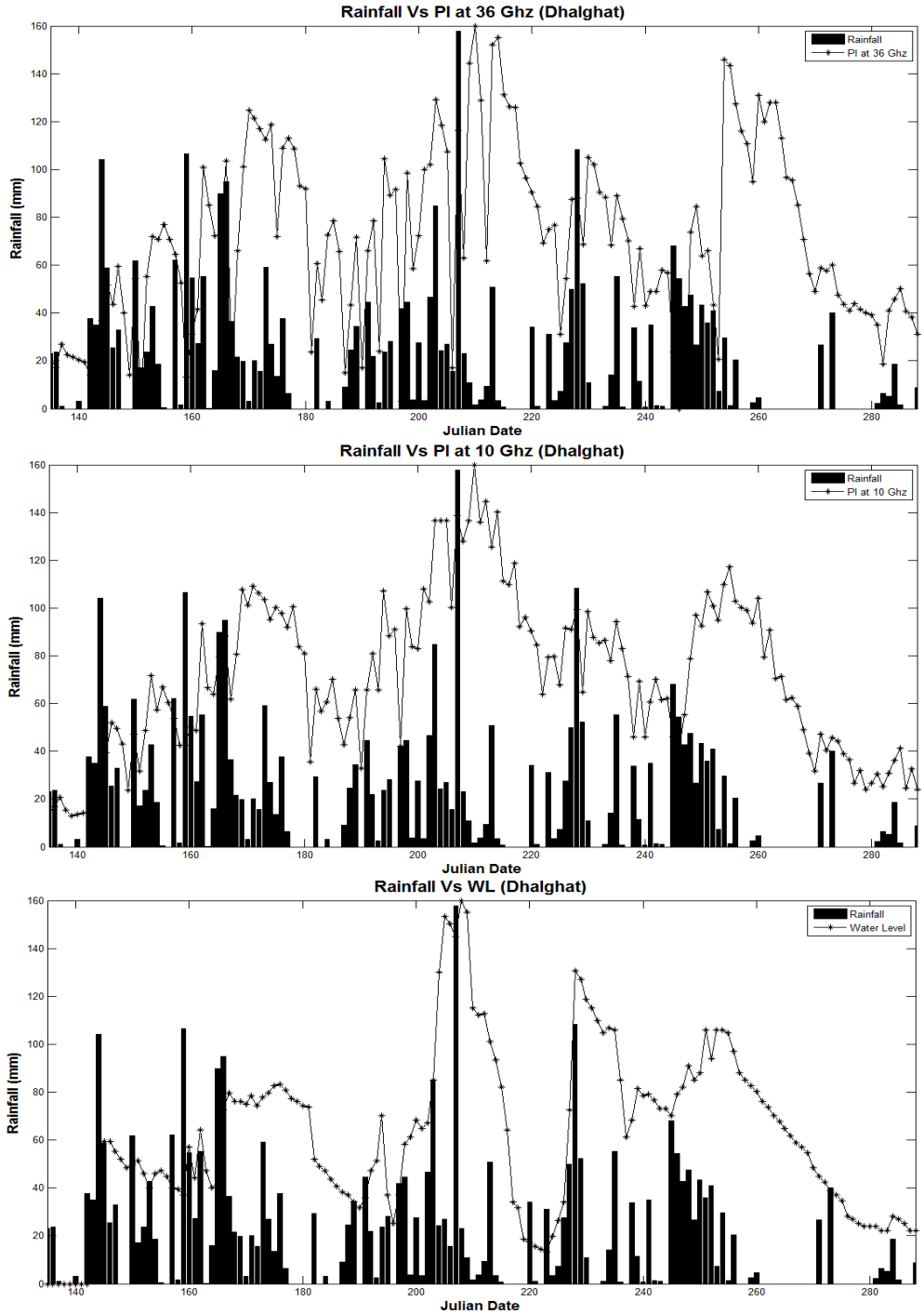

Figure 3.6: Multitemporal trends. a) PI at 36.5 GHz, b) PI at 10.65 GHz and c) Water Level. Rainfall measurements are reported for comparison.

Plots of T_{BV} at 89.0 GHz as a function of the difference T_{BV} (23.8 GHz)-T_{BV} (89.0 GHz) generated over all samples on the site on 29/06/2007 (Day 179) and 15/07/2007 (Day 186) are shown in Figure 3.8. Precipitation data provided by IMD confirm that rainfall did not occur on the first day and occurred on the second day (see Table 3.1). By applying the algorithm, we established that the samples, at which (T_{BV} (23.8 GHz) -T_{BV} (89.0 GHz) > 35K and T_{BV} (89.0 GHz) < 240K) are rain affected pixels. The values so

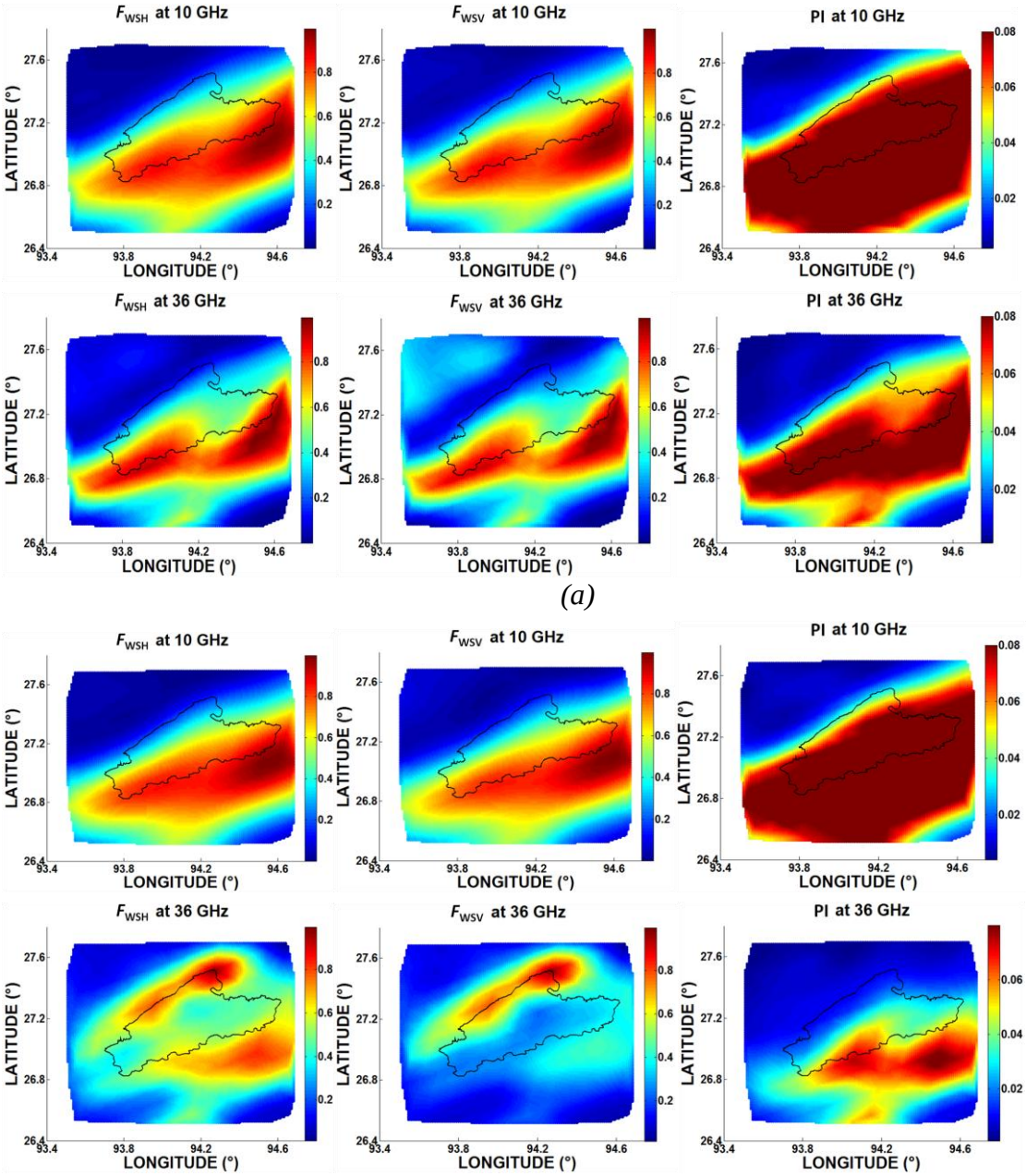

Figure.3.7: (a) Maps of F_{WSH}, F_{WSV} and PI at 10.65 GHz and 36.5 GHz on 29/06/2007, without rain (b): Maps of F_{WSH}, F_{WSV} and PI at 10.65 GHz and 36.5 GHz on 15/07/2007 with rain

Obtained for threshold however, were slightly different from the one obtained by Jin et al. (2006), mainly due to the fact that here the study area is not that dry as in west central Africa. Data were analyzed for two dates and the threshold was decided based on the scatter plot obtained.

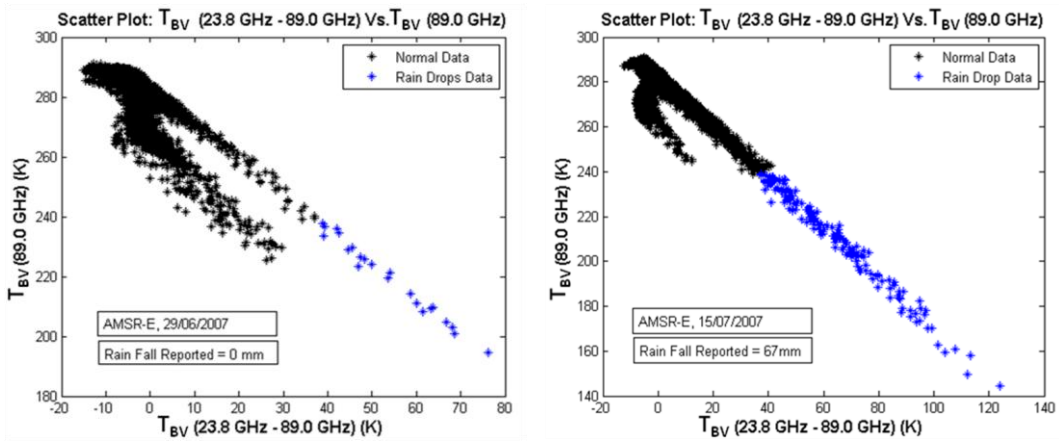

Figure 3.8: Scatterplots of T_{BV} at 89.0 GHz vs. the difference T_{BV} (23 GHz – 89.0 GHz). Left: June 29 (no rain). Right: July 15 (rain)

The trends of PI as a function of Water Level were plotted again after removing all the samples which resulted affected by rain according to the algorithm. Results are shown in Figure 3.9. The samples affected by rain are indicated by red dots. The correlation coefficient is improved by a significant amount in all the three sites (Figure 3.9).

3.7 Possible use of PI to generate flood maps

A detailed analysis over three areas showed that the PI at X band has a good potential to monitor the extension of flooding. The analysis was extended to a wide ($1.4^0 \times 1.4^0$) area, including the basin. Results are shown in the form of PI maps in Figure 3.10. Maps show PI values on three dates of 2007: 18/03/2007 (before flood), 10/09/2007 (during flood) and 13/11/2007 (after flood). Difference maps are also reported. Dates were selected keeping in mind the ground conditions tallied with IMD and WL data. The maps were obtained by using same interpolation techniques keeping half a minute interval at X band. On both sides of the river, flooding produces evident effects over large areas, confirming the potential of the instrument (particularly using PI at X band) to be used as an operational tool. It was noticed that the increase of *PI* during monsoon is mostly attributed to vegetation submerging.

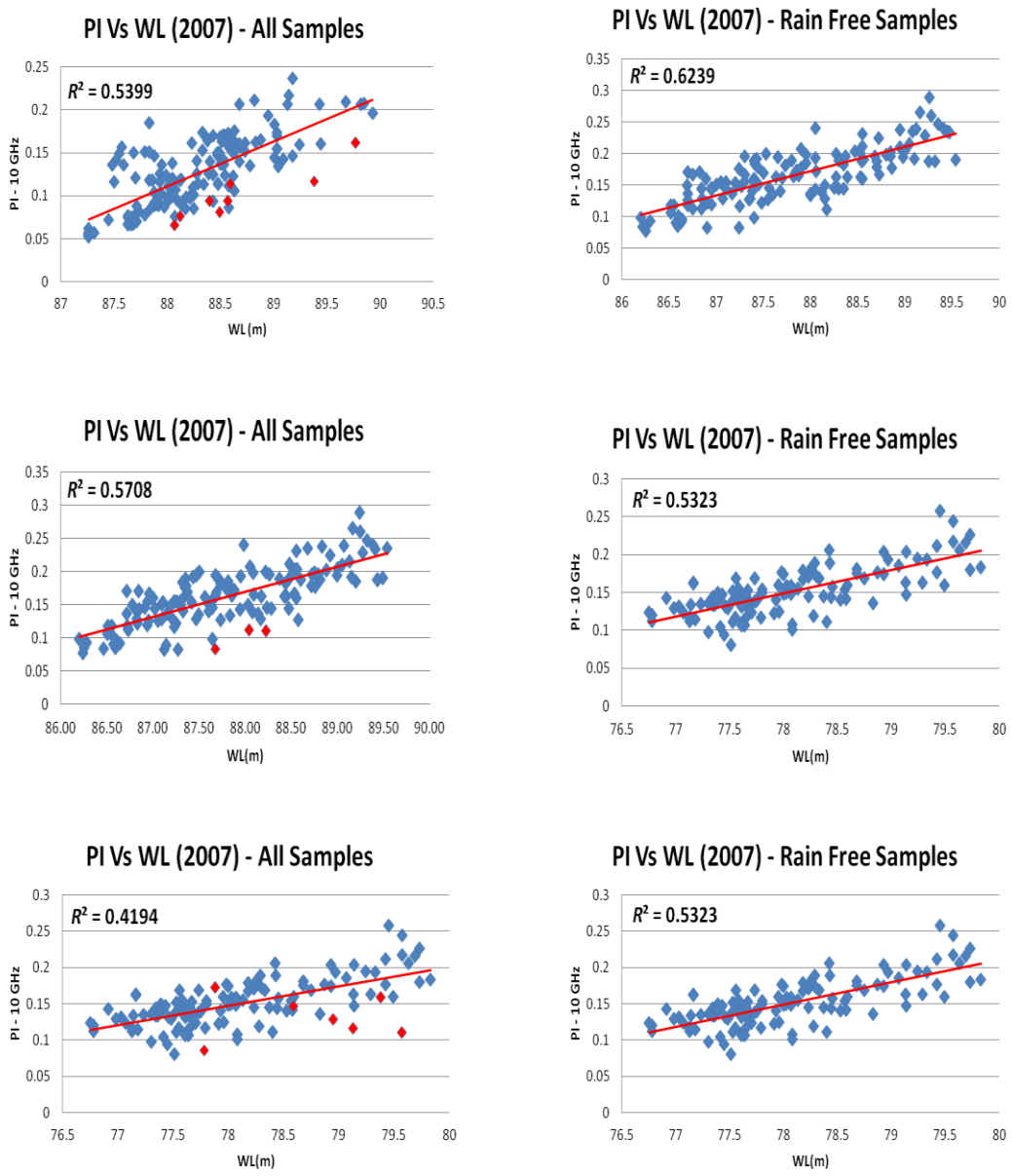

Figure 3.9: Scatterplots of Polarization Index (PI) at X band vs. Water Level for Dhalgat, Ghansari and Jamugurihat sites. Left: All samples, red dots indicate samples affected by rain. Right: Only rain free samples.

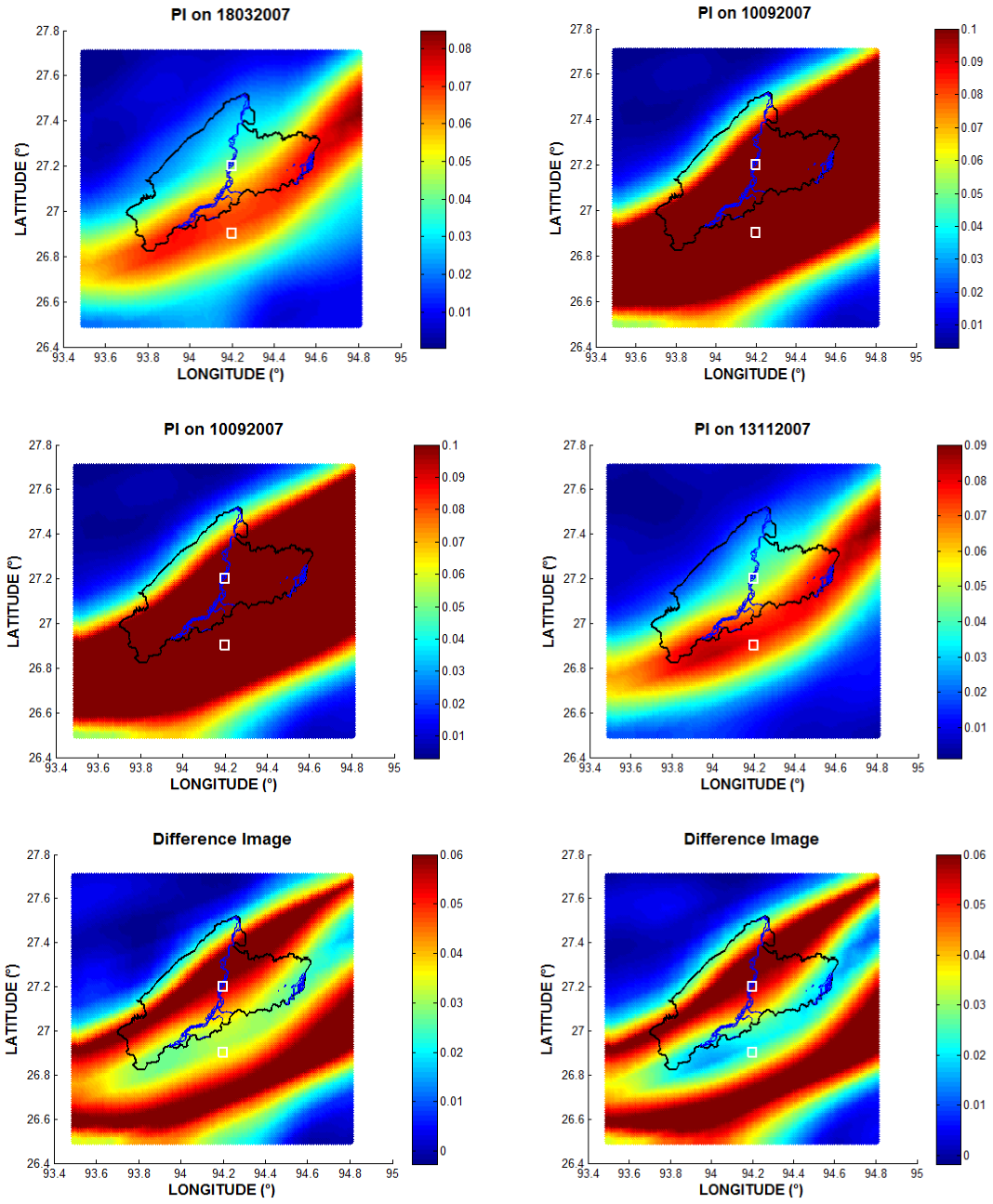

Figure 3.10: Maps of PI at X band of Lakhimpur District and neighboring areas, in 2007. Left hand side, top to bottom: March 18th (before flood), September 10th (during flood) and difference image. Right had side, top to bottom: September 10th (during flood), November 13th (after flood) and the difference image. White squares indicate the locations of water level stations and the blue line represents the main rivers.

3.8 Conclusion

The capability of AMSR-E signatures to monitor floods has been tested over the Indian Brahmaputra basin, which suffers intense flood effects related to periodic Monsoon. The lowest AMSR-E frequency (C band) suffers limitations due to coarse resolution, and is affected by RFI. At the higher frequencies (e.g. K_a band) limitations are related to raindrop interactions and high vegetation attenuation. X band

demonstrated to have a good trade-off between spatial resolution and sensitivity requirements. Therefore, it proves to be particularly useful when the site is characterized by wide vegetation covers and high recurrence of rainstorms. The performances of different parameters defined in the literature, such as Polarization Index (PI) and Fractional Water Surface (F_{WS}) have been investigated. PI proved to have the best correlation with water level measurements in the river. This result is related to the particular properties of the site, which is mostly covered by paddy fields. Flooding effects on PI are related both to an increase of soil moisture and to a decrease of emerged vegetation height. While correlation between PI and WL is good when WL increases, it is reduced when it decreases, since the water remains in the large AMSR-E pixels, and subsides with some delay with respect to the river. At X band, a significant improvement in the correlation between PI and WL is obtained after eliminating samples affected by raindrop interactions. To this aim, a technique based on AMSR-E data collected at 23.8 GHz and 89.0 GHz, was applied. The PhD work proposal also included development of a flood response system. The plan was to generate a network-enabled GIS based solution, to be developed using open source tools, to assess post flood damage with the help of query based modules, with outputs in the form of both maps and statistical database. This resultant data and information generated would have been useful for planning, designing and executing the emergency response measures in an effective manner. But the resolution of AMSRE data was not optimum to map the accurate extent of flood for a better post-flood disaster management analysis at smaller scales. Due to this reason, this implementation could not be attempted. But such system could be of great benefit to the society, even if it just displays the flood maps derived from AMSRE data (without details query) on GIS background (village boundary), for a operators to assess the condition of a village during flood.

4 Retrieving soil moisture over Forests : SMOS results and comparison with ground observation, other algorithms and independent observations

4.1 Introduction

As discussed in chapter 1.2.1, soil moisture (SM) is an important parameter in weather, hydrologic, climatologic and atmospheric models because of its influence on evaporation, infiltration, runoff and uptake of water by vegetation. Because of its variability in time and place, however, creating a database of the entire earth based on field measurements would be extremely time- and labor-intensive. A solution to this is satellite imagery. Satellite imagery can give information on SM on a global scale, potentially at intervals of at most a couple of days.

For this purpose, the European Space Agency (ESA) has developed the Soil Moisture and Ocean Salinity (SMOS) satellite to retrieve soil moisture over several kinds of land cover, including low vegetation and forests (see section 1.4.2). This satellite measures brightness temperature (T_B) at L-band. From these measurements SM in the top five centimeters of the soil can be determined. The resolution is in a range of 30-50Km but, the data grid is approximately 15 by 15 km.

It is well established that soil moisture retrieval is difficult under forest cover (Grant et al. 2007; Guglielmetti et al. 2008 and Kurum et al. 2012). In fact the attenuation related to the high wood biomass reduces the contribution of the soil surface to the overall emission, thus reducing the sensitivity to variations of soil moisture. A further reduction of sensitivity is associated to litter cover (Grant et al. 2007; Kurum et al. 2012 and Grant et al. 2009). At C band and higher frequencies, crown attenuation makes soil moisture retrieval very difficult in most of the cases. At L band some sensitivity to soil moisture is expected, since crown attenuation is lower than that at the higher frequencies, however establishing quantitative models is not that simple.

Hence taking the above factors into consideration, developing a reliable forward model and a valid retrieval algorithm for forests is essential to analyze SMOS data more efficiently.

First of all, forest cover dominates several SMOS pixels. Moreover there are mixed pixels, and even when other land covers (e.g. agricultural fields, grass) are dominant, a correct characterization of forest emission improves the retrieval accuracy (Van de Griend et al. 2003).

To provide an insight into this problem important ground-based and airborne experiments have been undertaken over the years. Multitemporal measurements of brightness temperature were carried out over coniferous and broadleaf forests using L-band radiometers mounted on a tower (Grant et al. 2007; Guglielmetti et al. 2008; Kurum et al. 2012; Grant et al. 2008; Guglielmetti et al. 2007; Santi et al. 2009 and Kurum et al. 2011), and were accompanied by detailed measurements of ground variables, such as soil moisture, wood biomass, and forest geometrical properties. In some cases, outputs were used to test theoretical models (Kurum et al. 2011 and Kurum et al. 2012), or fit the parameters of semi-empirical models (Grant et al. 2008 and Santi et al. 2009). Upward looking radiometric data were also collected in some forests (Grant et al. 2008 and Santi et al. 2009). Moreover, airborne campaigns have provided useful data for investigating the relationship between emissivity and forest biomass (Lang et al. 2000; Saleh et al. 2004 and Macelloni et al. 2001), and soil conditions (Grant et al. 2010). Although these efforts are

very important, they are not yet sufficient to reach a complete understanding of the forest emission problem, and to draw conclusive considerations. While some studies indicate the radiometric sensitivity to variations of soil moisture to be poor in developed forests (Grant et al. 2007; Guglielmetti et al. 2008 and Kurum et al. 2012), others over moderately dense forests with thin litter show the sensitivity to be appreciable (Guglielmetti et al. 2007; Santi et al. 2009 and Grant et al. 2010), although still lower than over low vegetation. Moreover, further efforts are required to establish if the sensitivity to soil moisture is mostly reduced by crown attenuation or by litter cover. Spaceborne monitoring can substantially help to investigate these problems.

Details about SMOS measurements have been given in Section 1.4.2 and the basic concepts underlying the algorithms adopted to retrieve soil moisture have been given in Section 2. The SMOS retrieval algorithm (Kerr et al., 2012) is based on two main components. The first consists of a forward model, which estimates the T_B emitted by land nodes of SMOS using a priori information (from auxiliary data) about land cover, surface temperature, Leaf Area Index (LAI), and initial estimates of soil moisture taken by the data base of the European Centre for Medium-Range Weather Forecasts (ECMWF). The second consists of an inversion process, which estimates the actual soil moisture and optical depth by using multiangular measurements, forward model outputs and a Cost Function (Kerr et al. 2012). The algorithm follows an iterative approach which aims at minimizing a cost function whose main component is the sum of the squared weighted differences between measured and modeled T_B data, for a collection of incidence angles. This is achieved by finding the best-suited set of parameters, which drive the direct T_B model, e.g., SM and vegetation characteristics.

For all SMOS nodes classified as soil covered by vegetation, the T_B is estimated by a simple first order radiative transfer model (Grant et al. 2007) as described in section 2.2. At the SMOS scale, pixels are not uniform and may have a variety of surface types. In such cases, the total T_B comes from several classes of emitters. This composite T_B is obtained through an aggregated forward model which combines each class of emitting sources weighted by their intra-pixel cover fractions. In order to keep the algorithm consistent, and to consider the case of mixed pixels, the same approach is kept for both low vegetation and forests (Kerr et al. 2012). For the case of forests, the radiative transfer parameters τ (optical depth) and ω (albedo) are estimated using the synthetic outputs of the theoretical model described in Ferrazzoli and Guerriero (1996), according to the procedure which was further developed in Ferrazzoli et al. (2002). The theoretical model was tested and revised using sets of ground based and airborne measurements carried out over various forests in different environments (Della Vecchia et al. 2007; Della Vecchia et al. 2010 and Rahmoune et al. 2010).

The choice of the operating wavelength for SMOS is determined by the increase in sensitivity of the brightness temperature to soil moisture (ground) with the decrease in the observation frequency. The 1400–1427 MHz band (L-Band) is used because it is the lowest passive frequency band allocated to the Earth Exploration Satellite Service (EESS) (Kerr 2001). But the microwave radiometers receive emissions at very low levels compared to those generally handled by other radio communications services; these sensors are therefore generally more susceptible to Radio Frequency Interference (RFI) originated from man-made emitters on the ground, on aircraft or space borne systems.

The issue of RFI within this passive band, especially due to the presence of long-range air surveillance radar systems in nearby bands, has been identified as a key concern by Committee On Scientific Use Of The Radio Spectrum (2010). Observations already performed using airborne campaigns have shown clear instances of RFI signals (Zribi 2011). Unwanted emissions arising from radars within the adjacent Earth Exploration-Satellite Service (EESS) band within the radiometer antenna footprint can easily exceed the maximum emission level allowed. The experience obtained during the operations of SMOS satellite is also showing that the presence of radio-links in nearby bands and unauthorized transmissions within passive band are also a common source of interference for the radiometer (Daganzo 2010).

The RFI problem is not due to inadequate filtering in the SMOS receiver (which is using less than the allocated frequency band and which boasts of very high performance), but is due to two specific problems: i) Unauthorized emissions within the protected passive band coming from active sources, ii) Unwanted emissions from active services operating in neighboring bands.

In this chapter results obtained by a prototype version of SMOS SM retrieval algorithm are shown. The basic algorithm is described in the Algorithm Theoretical Baseline Document (ATBD) (Kerr et al. 2010 and Kerr et al. 2012), while details about forest cover are given by Rahmoune et al. (2013). The prototype version of the algorithm here adopted is flexible and it can run with different sources of auxiliary data. In particular the Leaf Area Index, which is an input to the forward model, can be extracted by the ECOCLIMAP database (Masson et al. 2003b) or by the MODIS database (Knyazikhin et al. 1998a).

In this chapter, first of all, the specific aspects of the algorithm for forests will be described, followed with the details about the selected test sites used for validation of the results. Then some results about retrieved optical depth will be discussed..This is an important aspect, since a correct retrieval of optical depth is fundamental in order to correctly retrieve soil moisture. Finally, soil moisture retrieval results will be presented. Different approaches to make comparisons with available ground measurements and filtered data were used, and relevant results were presented. Initially, for the selected nodes of the available ground networks, averaging was done among SM outputs obtained by the retrieval algorithm in all SMOS nodes with a center falling within the buffer of 15 Km distance from the ground observation. This first analysis was done by using both ECOCLIMAP and MODIS as input data sets for the LAI of the forward model, and results were presented. Then, other comparisons with ground measurements were shown, done using ECOCLIMAP as input data set, and taking just the SMOS node with a center having the closest position with respect to the considered network node. This analysis was repeated under different conditions imposed to RFI filtering and location of SMOS nodes with respect to the swath axis. Finally, SM data obtained by SMOS and results obtained by the Advanced Microwave Scanning Radiometer - Earth Observing System (AMSR-E) were compared with respect to the ground observation to analyze the SM output derived from different data products. In this study, two algorithms were considered, which were developed to determine SM from AMSR-E measurements, namely that of the National Snow and Ice Data Centre (NSIDC) and the Vrije Universiteit Amsterdam (VUA) in combination with NASA.

4.2 SMOS Algorithm

4.2.1 General properties of SMOS Algorithm over forests

4.2.1.1 The forward model

As stated in Section 4.1, a simple radiative transfer equation of zero order RT0 (see Sections 2.1.5 and 2.2) is used as forward model in order to estimate the brightness temperatures which are compared against SMOS measurements. For forests, the initial values of ω and τ (see equation 2.25) were estimated by fitting the outputs of a theoretical model, which is based on the radiative transfer theory and adopts a discrete approach (Ferrazzoli and Guerriero 1996). In that model, trunks and branches are represented as dielectric objects with the shape of cylinders, while leaves are represented as needles or disks. The bistatic scattering cross sections and extinction cross sections are computed by using suitable electromagnetic approximations. The bistatic scattering coefficient of the soil is computed by using the Integral Equation Model, in its bistatic version (Fung 1994). Single contributions are combined by using the matrix doubling algorithm, which allows us to compute the overall bistatic scattering coefficient in all directions,

including multiple scattering effects. The overall reflectivity is computed using formulas of Section 2.1.5, where the incoherent component is obtained by integration over the upper half space and the emissivity is finally obtained by the energy conservation law. Details about the electromagnetic model are given in Ferrazzoli and Guerriero (1996). For litter, the model published in Della Vecchia et al. (2007), which considers the litter as a dielectric layer over the soil, was applied.

This theoretical forest model was previously tested against ground based and airborne measurements (Della Vecchia et al., 2007; Della Vecchia et al., 2010; Rahmoune et al., 2010). RMS errors were in the range of 2.5 K – 4.0 K.

As discussed in (Rahmoune et al., 2013), for estimating the input variables and parameters, the procedure assumes to know, besides soil variables, the following inputs:

- Leaf Area Index contributed by forest leaves LAI_F
- Leaf Area Index contributed by herbaceous vegetation LAI_V
- Distribution of trunk diameters at breast height *dbh* [cm]: *p(dbh)*
- Moisture [g/g] and dry matter density ρD [g/cm^3] of trunks, branches and leaves.

Using allometric equations, simplifying approximations and the theoretical model, the emissivity was computed at both V and H polarizations, at all angles in the range of 20°-50° and for soil moisture values in a range of 0.05-04.

The simulation outputs were used to fit the equivalent parameters τ_F (forest optical depth) and ω_F (forest albedo), contributed by arboreous vegetation and assumed to be independent of polarization, of the RT0 forest model. The RT0 model was run for the same conditions as the theoretical model, and ω_F and τ_F were selected in order to yield the minimum root mean square (rms) difference between T_B (K) outputs of the two models.

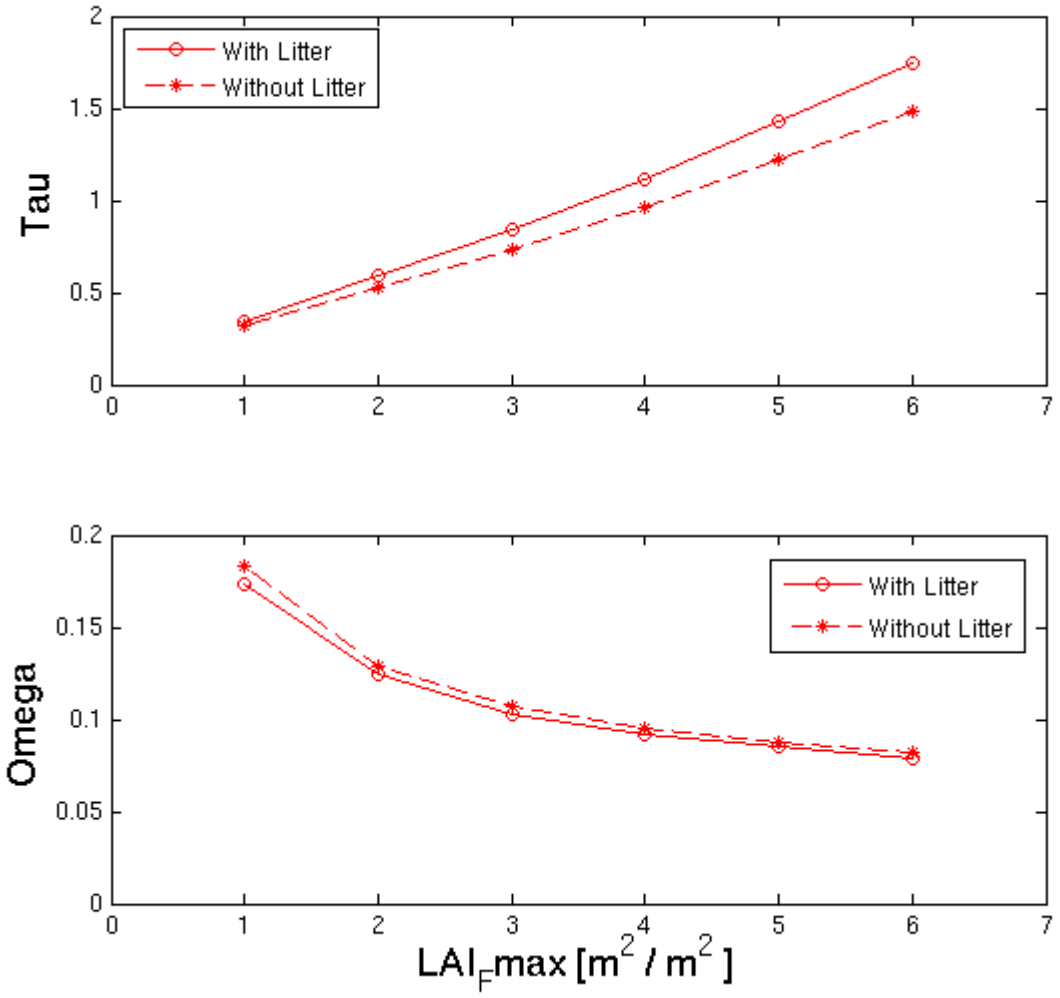

Figure 4.1: Trends of fitted radiative transfer parameters τ_F and ω_F as a function of maximum yearly value of forest LAI,for broadleaf forests (Rahmoune 2013).

A key variable is the actual maximum yearly value of Leaf Area Index contributed by forest leaves (LAI_{Fmax}). The trends of τ_F and ω_F as a function of LAI_{Fmax} , for the case of broadleaf forests, are shown in Figure 4.1. Values of τ_F lower than about 0.6 are achieved for sparse forests with $LAI_{Fmax} < 2$. The albedo ω_F shows a decreasing trend vs. LAI_{Fmax} .

A linear regression was then applied to the relationship between the optical depth and LAI_{Fmax}, in order to compute the coefficients of a linear relationship such as:

$$\tau_F = b_F LAI_{F\max} \tag{4.1}$$

The resulting coefficients are:

$b_F = 0.29$ for broadleaf forests.

$b_F = 0.36$ for coniferous forests.

Equation (4.1) gives the maximum yearly value of τ_F, which is achieved in full leaf development. If the forest is deciduous, τ_F decreases in late autumn and winter due to the absence of leaves. Further model simulations, not shown here, indicated that the corresponding decrease of b_F coefficient is 0.03 units. Therefore, a general expression is:

$$\tau_F = b_F LAI_{F\max} - 0.03(LAI_{F\max} - LAI_F) \tag{4.2}$$

The total optical depth, including contributions of both forest vegetation and herbaceous vegetation is given by:

$$\tau = \tau_F + b_V LAI_V \tag{4.3}$$

The b_V coefficient is set equal to 0.06, which is the value adopted by the ATBD for low vegetation (Kerr et al., 2010).

Then, we assumed:

$LAI_F = f_F \ LAI$

$LAI_V = f_V \ LAI$

LAI is the total Leaf Area Index, available by ECOCLIMAP data base (Masson et al., 2003b).

f_F and f_V represented the fractions of LAI contributed by arboreous leaves and herbaceous vegetation, respectively. Some data are available in the literature, showing some dispersion. In order to simplify the initial guess of τ we made an assumption which was verified in some broadleaf and coniferous forests (Peduzzi et al., 2010 and Blanken et al., 1997). : $f_F = 0.6$, $f_V = 0.4$

For the albedo, the value achieved fitting the outputs of the theoretical model (as described above) for the dense forest (higher values of LAIFmax in Figure 4.1) is used:

$\omega_F = 0.08$

This value represented a good fit for both broadleaf and coniferous forests.

The roughness parameter h of Equation (2.23) has been set equal to 0.3. This value corresponds to a height standard.of about 1.0 cm, which is quite realistic.

The procedure described in this Section leads to compution of the optical depth and the albedo of the RT0 forest model

4.2.1.2 The retrieval procedure

Using brightness temperatures simulated by the forward model and measured over SMOS grid nodes, SM and optical depth are determined. The calculated T_B is used in an iterative procedure which minimizes a "cost function" in order to get the retrieved SM and τ. The cost function subtracts measured multiangular brightness temperatures (L1C data), measured by the satellite to the T_B's simulated by the model. SM and τ , which are parameters in the equations for T_B (see Section 2, eq. 2.25), are kept free in the function in order to determine the best fit of measured and theoretical T_B.

In this process, the algorithm uses initial values of soil moisture predicted by ECMWF and the optical depth predicted by the procedure illustrated in section 4.2.1.1.

4.3 AMSRE Algorithm

As specified in Section 4.1, soil moistures retrieved by SMOS will be compared with the outputs of two algorithms exploiting AMSR-E data. Some information about the two algorithms is summarized here. The AMSR-E satellite has a morning (descending) and evening (ascending) overpass (see Section 1.4.1). Two different SM datasets derived from the AMSR-E satellite, NSIDC and VUA, have been considered. The difference between NSIDC and UVA SM product lies in the algorithm used. The details are explained in the next paragraph. For both the cases, SM is determined for approximately the first centimeter of soil. Both datasets have a resolution of 0.25 by 0.25 decimal degrees.

NSIDC SM data is determined using X-band (10.65 GHz) and Ku-band (18.7 GHz) channels. The algorithm uses two low frequency dual polarized channels to optimize SM, vegetation optical depth and effective soil temperature simultaneously. The SM algorithm uses the Polarization ratio (PR). PR is the difference between the vertical and horizontal T_B at a given frequency divided by their sum. This effectively eliminates or reduces surface temperature effects, which is necessary since no dynamic ancillary surface temperature is used as input to the algorithm. The algorithm first calculates a vegetation/roughness parameter, g using PR at 10.7 GHz and PR at 18.7 GHz, plus three empirical coefficients. SM is then computed using departures of PR at 10.7 GHz from a baseline value, plus four additional coefficients. The baseline values for PR at 10.7 GHz are based on monthly minima at each grid cell over annual cycle. The parameter g incorporates effects of vegetation and roughness together and is interpreted as an equivalent vegetation water content. It uses average values of optical depth and temporal variations for calculating SM. The input T_B data corresponds to 38 Km mean spatial resolution, and are resampled to a global cylindrical 25 km EASE- Grid cell spacing. The effective spatial resolution is thus slightly higher than the inherent 38 km resolution.

VUA data is derived according to the Land Surface Parameter Model (LPRM) (Owe et al. 2007). The LPRM is a three-parameter retrieval model for passive microwave data and is based on a microwave radiative transfer model that links surface geophysical variables (i.e., SM, optical depth, and soil/canopy temperature). The model uses dual polarized channel (either 6.925 or 10.65 GHz) and retrieves both SM and optical depth. The SM retrieval methodology uses a nonlinear iterative procedure in a forward modeling approach, into its primary source components, i.e. the soil emission and the canopy emission, and then optimizes on the canopy optical depth and the soil dielectric constant. Once convergence between the calculated and observed T_B is achieved, the model uses global database of physical properties (Rodell et al. 2004) together with a soil dielectric mixing model (Wang and Schmugge 1980) to derive surface SM. The model is largely physically-based with no regional dependence since no field observations of SM, canopy biophysical properties, or other observations are used for calibration purposes.

For both the products, descending data was used, as it was falling close to the timing of SMOS SM measurement and Ground SM observations.

4.4 Test Sites

4.4.1 SCAN/SNOTEL Nodes

The SCAN from the National Soil Survey Center (NRCS), USDA, gives free access near real time (NRT) with hourly sampling access to climatic station data across the U.S. (http://www.wcc.nrcs.usda.gov) (Schaefer et al. 2007). The stations are equipped with a multitude of sensors (air temperature, relative humidity, soil moisture at different depths, soil temperature at different depths, solar radiation, wind speed, precipitation, etc.). The most important sensors for this study are the soil moisture at 2 in (~5 cm), soil temperature at 2 in, and precipitation. The soil moisture instrument is the Hydra Probe (Stevens). The original objective of the SCAN network was to improve decision making in agriculture, but the network has been extensively used in research activities. Several investigations (Sahoo et al. 2008; De Lannoy et al. 2007; Jackson et al. 2010 and De Lannoy et al. 2011) used the SCAN site data combined with other data sources for validation of soil moisture products.

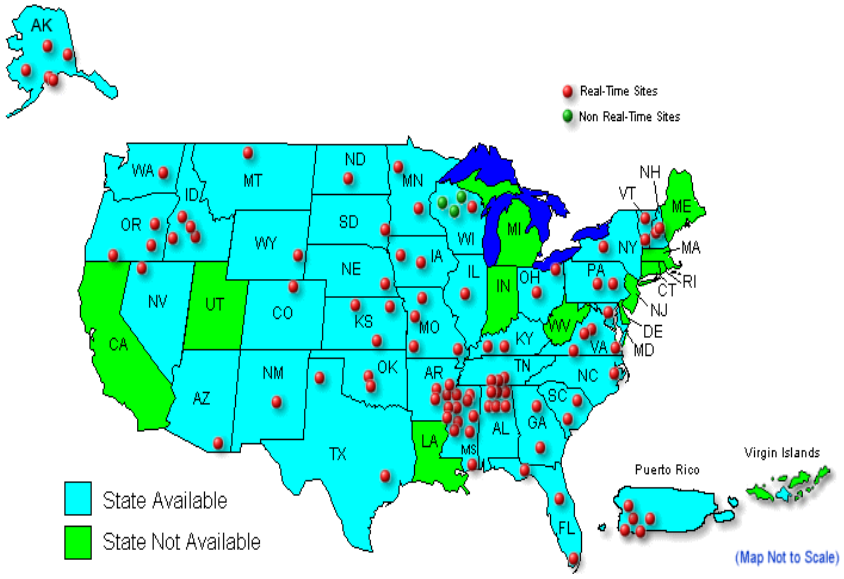

Figure 4.2: SCAN network

The network has a low density compared to the heterogeneity of soil moisture over the SMOS footprint but covers a wide variety of soil types and climates over continental U.S. (See map in Figure 4.2). The NRT data are provided after screened sensor limits, and no additional processing or quality check is provided.

The NRCS also gives NRT access to the SNOTEL network. This network covers the Western U.S. and Alaska. SNOTEL stations are, in majority, installed over mountainous regions (Rocky Mountains, Colorado) with forests. In many SNOTEL sites, a soil moisture Hydra Probe is installed. Both SNOTEL and SCAN data collection systems use meteor burst communication techniques to obtain near real-time data from remote sites (http://www.wcc.nrcs.usda.gov/ftpref/downloads/factpub/soils/SNOTEL-SCAN.pdf).

4.4.2 BERMS (CANADA)

BERMS is located in the southern boreal forest in north central Saskatchewan, Canada. The BERMS research effort is a collaborative project with EC and other government agencies and universities (http://berms.ccrp.ec.gc.ca/Overview/e-overview-brochure.htm). The project began in 1996 following the

end of the BOReal Ecosystem and Atmosphere Study (BOREAS). While BOREAS was an episodic research project that took place in 1994 and 1996, the BERMS project is continuous.

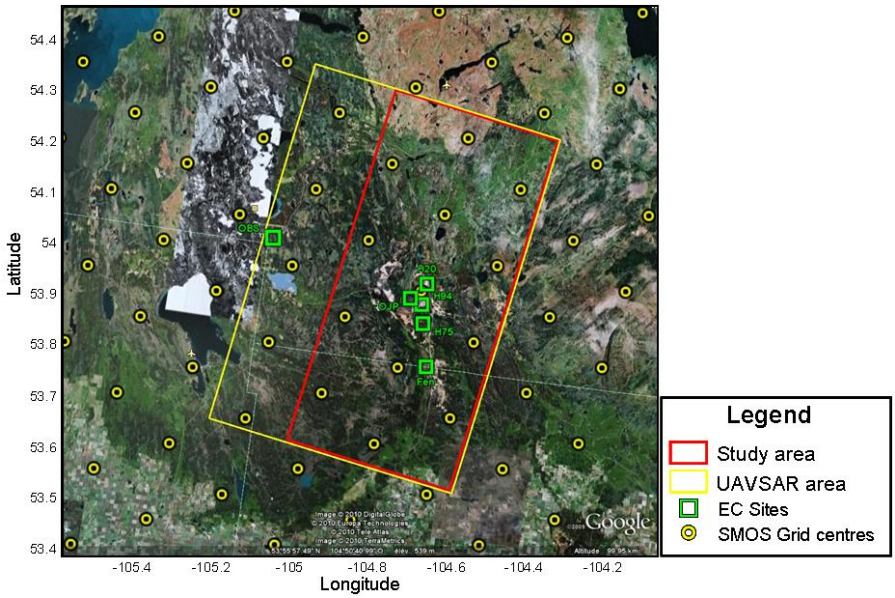

Figure 4.3: CanEx-SM10 study area over BERMS

The Canadian Experiment for Soil Moisture in 2010 (CanEx-SM10) originated as an initiative of Canadian researchers to support the Soil Moisture and Ocean Salinity (SMOS) validation activities over land and to develop soil moisture retrieval algorithms. The experiment was extended to include pre-launch validation and algorithm development for the Soil Moisture Active and Passive (SMAP) mission through a collaboration with US researchers. CanEx-SM10 field phase took place from May 31 to June 17, 2010 over agricultural and forested sites located in Saskatchewan, Canada. The BERMS region is located north of Prince Albert in Saskatchewan near the southern extent of the boreal forest. See map in Figure 4.3. The topography is generally rolling and the dominant vegetation type depends on soil type, drainage conditions and disturbance. The dominant species in well drained and sandy soils are jack pine with black spruce more prominent in wetter, less well drained areas. Aspen, which is typically a disturbance species, can be found in areas that have been burned or harvested. Other species, such as white spruce, birch, and tamarack can also be found. The CanEx-SM10 project does not use the entire BERMS study area but rather is confined to a domain in the most eastern portion of the study area.

BERMS consists of a series of instrumented research sites located in various vegetation types and age structures throughout the region. Within the study domain indicated above are OBS, OJP, FEN, H75, H94 and H02. A brief description of each site is mentioned below. More information can be found at http://berms.ccrp.ec.gc.ca/Sites/e-sites.htm.

- OBS: Old Black Spruce Mature wet coniferous black spruce forest Moss and Labrador tea understory Stand age ~ 114 years Canopy height 11 m.

- OJP: Old jack Pine Mature dry coniferous jack pine forest Lichen understory Stand age ~ 94 years Canopy height 14 m.

- H94: Harvested Jack Pine 1994 Young jack pine stand logged in 1994 Stand age ~ 20 years Canopy height ~ 2-3 m.

- H75: Harvested Jack Pine 1975 Young jack pine stand logged in 1975 (originally part of BOREAS experiment) Stand age: ~ 30 years Canopy height ~ 5 m.

- H02: Harvested Jack Pine 2002 Site was logged in 2000 with the surface scarified in 2002 Ground cover consisting of sparse grass, shrubs and immature jack pine seedlings.

- FEN: Patterned fen surrounded by black spruce, tamarack and jack pine forest (originally part of BOREAS experiment).

4.4.3 Indian sites

L-band is a protected frequency band for radio-astronomy and remote sensing satellite services. However, it is bordered by radio location and communications services, and field experimental campaigns have provided evidence that there is a potential risk for corruption due to out-of-band emission or Radio Frequency Interferences (RFIs). SMOS data which uses L-band, shows severe RFI problems. The RFI sources, present over large parts of Europe, China, South Asia and the Middle East, significantly influence the quality of the SMOS data. Figure 4.4 shows RFI map over India at ascending and descending orbit of SMOS data (www.cesbio.ups-ttlse.fr/SMOS-blog/tag=rfi). Asia and Europe together hold 86% of the sources in the world and 86% of the strongest (Oliva et al. 2012). The American continent is by comparison much cleaner, except for some RFI sources distributed over Canada and United States.

India is also one of the most severely affected countries due to Radio Frequency Interference (RFI). This makes difficult to work with lower frequencies specially L-band over most parts of the India. Since the power transmitted by a RFI source within the passive band is proportional to the T_B measured by the radiometer, this problem directly results in wrong estimation of the T_B and makes the data useless for any further studies. A refined analysis using on-board calibration data allows to focus the T_B images (http://www.smos-bec.imc.csic.es/node/36), but even though the RFI regions become more localized, the amount of RFI was in many cases so large that the tails of the 'impulse response' to a RFI quasi point source extended over the whole image, making it difficult the retrieval of geophysical parameters.

Results of the erroneous T_B values due to RFI over the Indian forest along with RFI maps provided by SMOS are discussed in the following paragraphs.

As the satellite moves, the single SMOS node is viewed with many incidence angles from 0^0 to 60^0, and for each node we have two polarizations XY/HV. Some of these incidence angles are affected by RFI either in X Y or in X or Y. Figure 4.5 (a), indicates the number of view affected by RFI corresponding to X-polarization and Y-polarization, acquired consecutively every 1.2 sec in dual polarization mode. In SMOS imagery, the antenna switches connect the receivers in one array arm either to the X- or Y-polarization antenna probe following a predetermined sequence. Four stokes parameters images are obtained after four switching intervals, and due to pulsed nature of many RFI sources, RFI can happen in one of the intervals and not in others, in an unpredictable manner. Figure 4.5 (b) shows maps of T_B values at Vertical and Horizontal polarization over each Julian day of year 2010 over the forest (Western Ghats), of India. It is obvious from the figure that in some cases the RFI is so strong that it completely corrupts the whole T_B values (Julian Day 67). In most of the other cases, the variation of T_B values at both polarizations are too high or too low, to be realistic. It is also worth noticing that the SMOS RFI is highly variable both in time and polarization and so even averaging the data do not help much. Ground information over some of the Indian forests and few flood plains were available, but due to high RFI issues any further analysis on the area had to be forcibly abandoned.

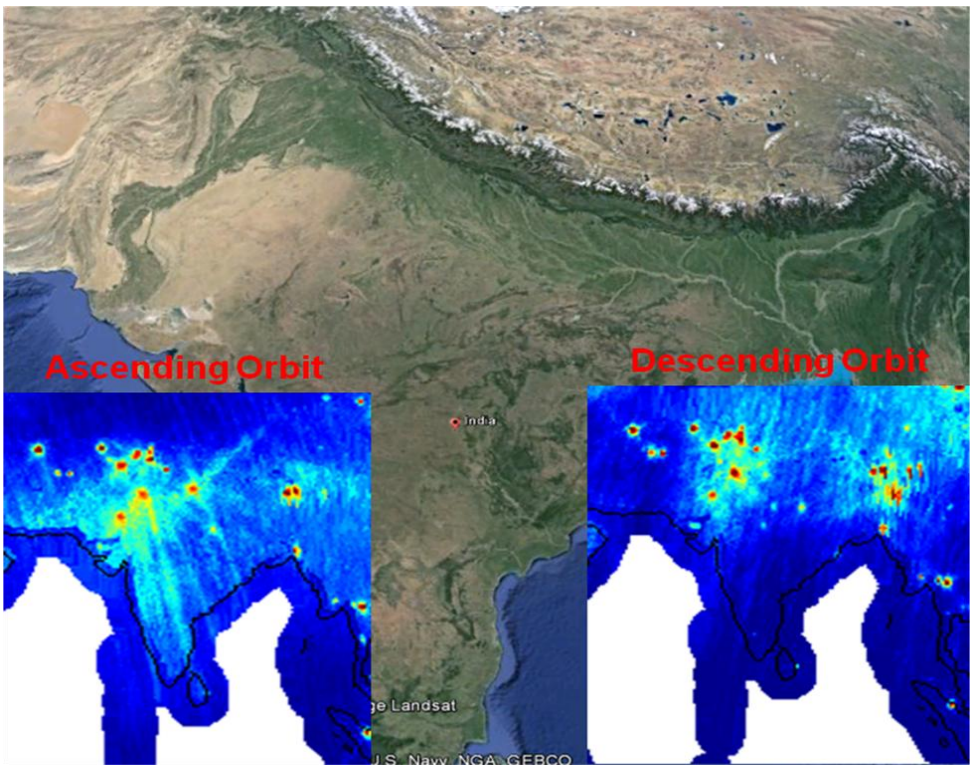

Figure 4.4: RFI map over India

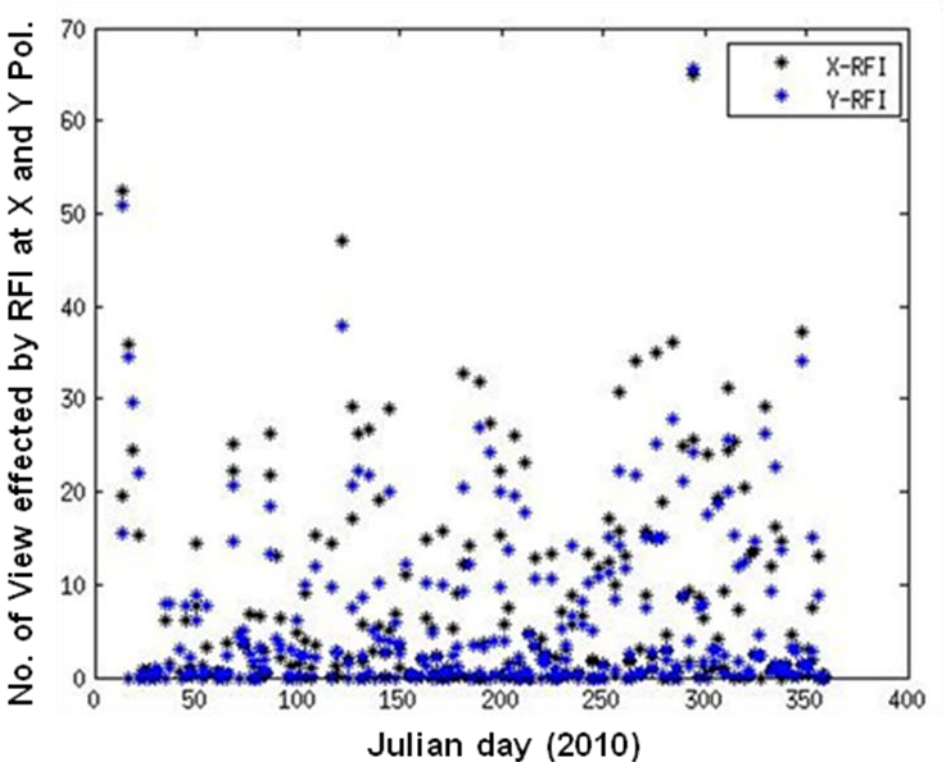

(a)

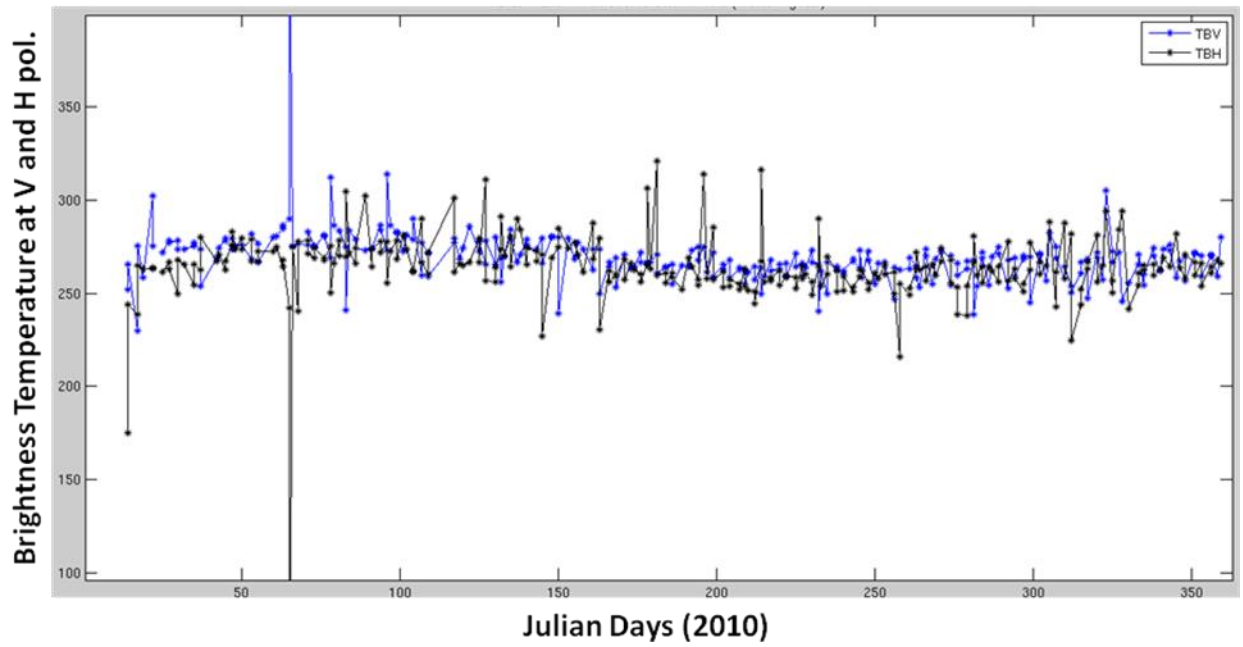

(b)

Figure 4.5: RFI issues over forests (Western Ghats) in India (a) RFI maps at X and Y pol (b)T_B at V and H pol. vs Julian Days

4.5 Results and Analysis

4.5.1 Retrieved Optical Depth

The initial estimate of τ is based on the procedure mentioned in section 4.2.1.1, which has several approximations. The algorithm starts from the initial estimate and uses SMOS L1C data in order to find τ minimizing cost function for each node.

4.5.1.1 Global Optical Depth Map

Global maps of optical depth were generated using the data collected from July, 1, 2011 to July, 4, 2011. ω was set to 0.08 for boreal forests and 0.06 for tropical and subtropical forests, as inputs to the algorithm, as a consequence of the preliminary analysis reported by Rahmoune et al. (2013). The algorithm described in Kerr et al. (2012) was used for low vegetation. The resulting map of optical depth is shown in Figure 4.6.

As expected, the optical depth in the areas covered by forests is higher than in low vegetation. In general, the map shows a correspondence with forest biomass maps available in the literature (FAO 2000 and NASA and Jet Propulsion Laboratory 2012). τ values higher than 1.0 are obtained in large part of the dense and thick Amazon forest, while a decrease is observed moving towards the subtropical Chaco forest, mostly covering Paraguay and Northern Argentina, where the vegetation is less dense. A high optical depth is also observed in Indonesia. Moderate values, typically in the range of 0.7-0.9 are obtained in Boreal forests of Canada, US, and Siberia. The retrieval is unsuccessful in the Congo forest, where the forest is dense and the quality of L1C data resulted to be poor.

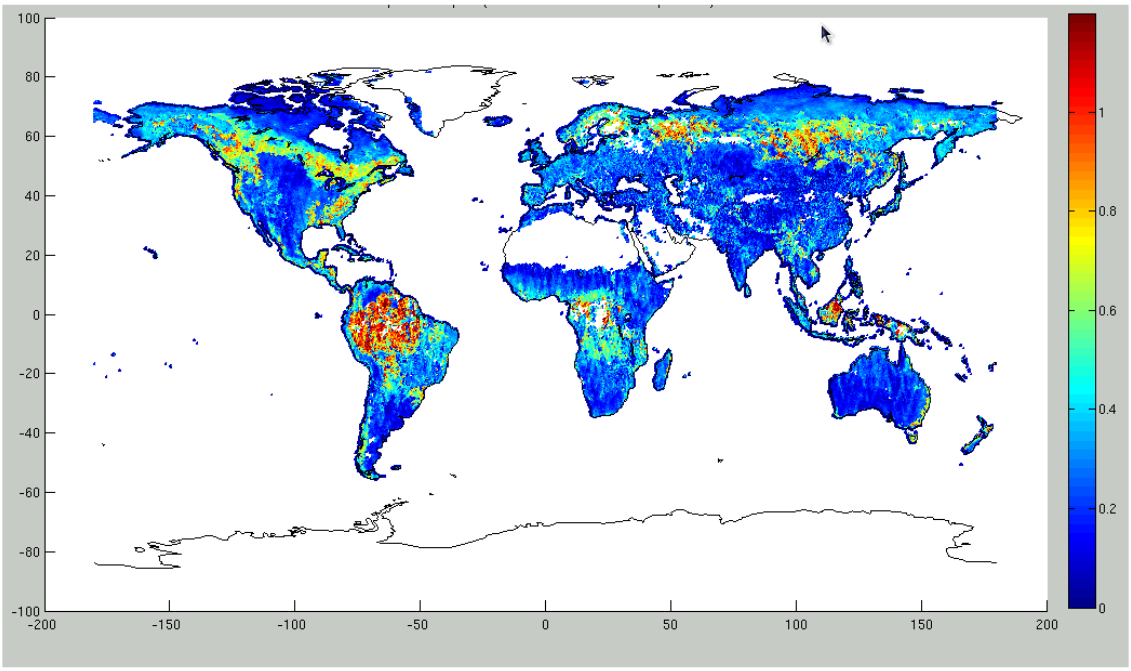

Figure 4.6: Global Map of Retrieved optical depth

4.5.1.2 SMOS optical depth and AMSR-E LPRM (VUA) optical depth

As mentioned in section 4.3, LPRM is a three-parameter retrieval algorithm (soil moisture, vegetation optical depth, and soil/canopy temperature) using passive microwave data and a microwave radiative transfer model. The algorithm uses dual polarized channel (either 6.9 or 10.6 GHz) of AMSR-E for the retrieval of both surface soil moisture and vegetation optical depth.

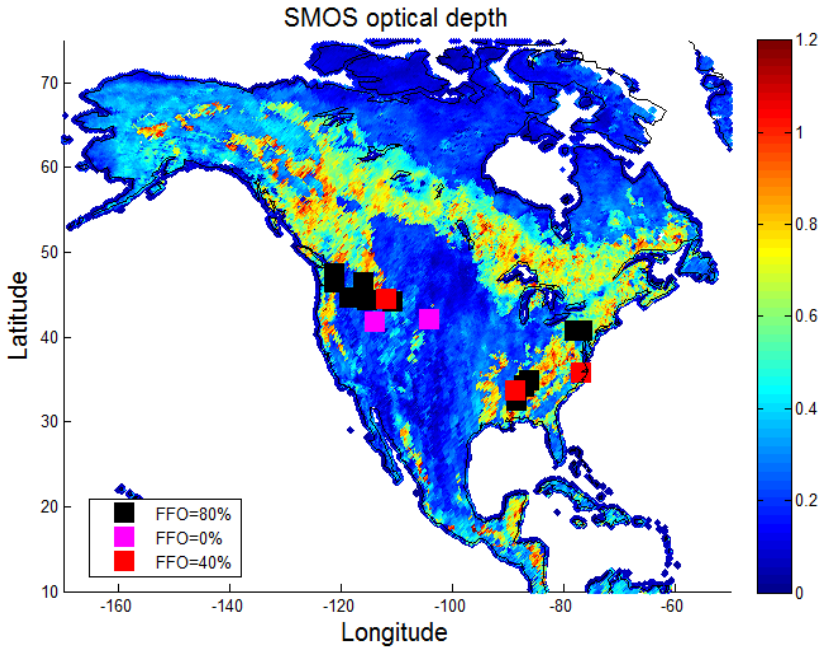

(a)

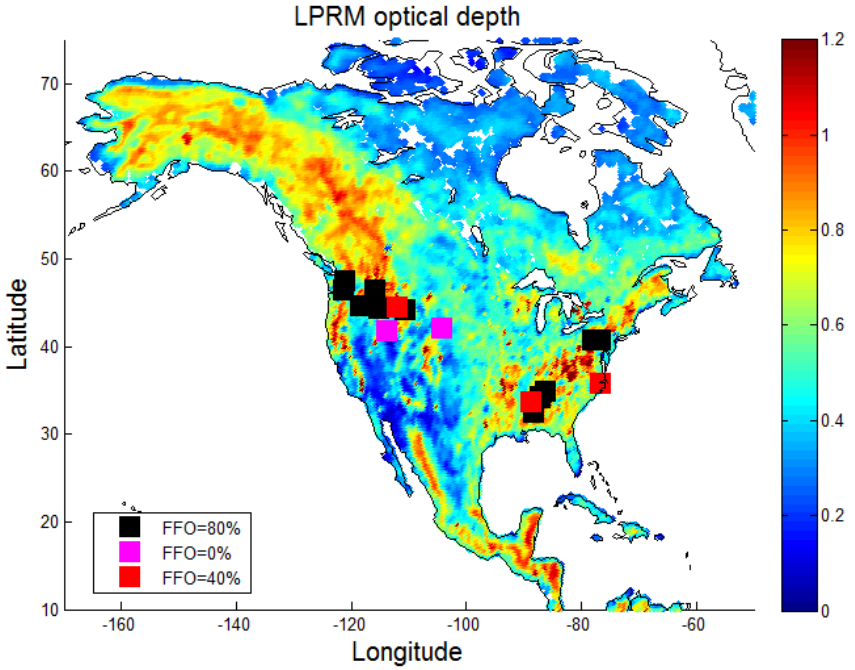

(b)

Figure 4.7: Optical Depth Maps obtained from (a) SMOS (1-4 July 2011) and LPRM (VUA) (1-2 July 2011) algorithms. Colored boxes indicate sites selected for SM retrieval.

Comparison was done between the SMOS retrieved optical depth and LPRM optical depth map under different forest fraction (FFO=80%, 40% and 0%). Figure 4.7 (a) and (b), shows the optical depth map retrieved from SMOS algorithm and the vegetation optical depth retrieved by the LPRM algorithm (and averaged for the period 1st July 2011 and 2nd July 2011).

In general, SMOS retrieval is more sensitive to the presence of forest cover, in comparison to LPRM. While L band signatures are fundamentally influenced by branch attenuation, C band signatures are also strongly affected by low vegetation or other factors. It is also worth noticing that, although noisy, SMOS vegetation optical thickness contains useful information regarding forest cover.

4.5.1.3 Comparison with an independent data source

Retrieved values of optical depth τ have been compared against tree height estimates obtained by the algorithm described in Simard et al. (2011), and made available by NASA Earth Observatory. The algorithm used data collected by the Geoscience Laser Altimeter System (GLAS) of ICESAT satellite, with information from MODIS, additional elevation data from the Shuttle Radar Topography Mission (STRM), and climatology information from both the Tropical Rainfall Measuring Mission (TRMM) and the http://www.worldclim.org/Worldclim database (Simard et al. 2011). GLAS data, which originally had 1 km resolution, were re-sampled at ISEA4H9 grid (1.4.2.2).

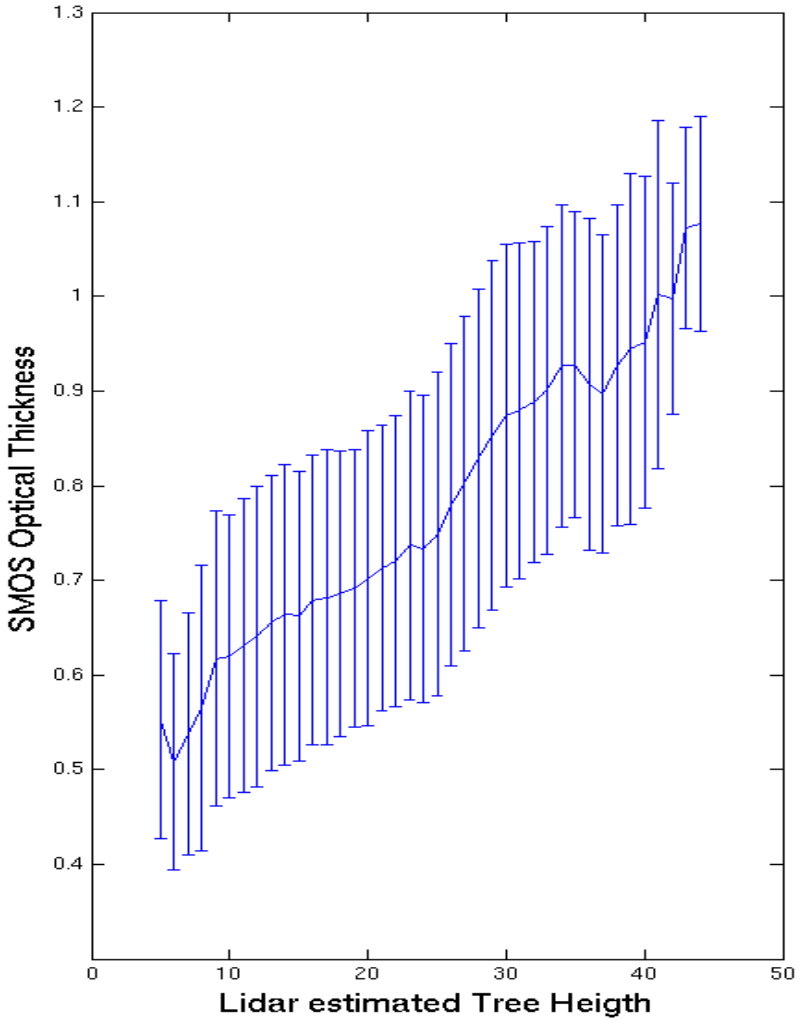

Figure 4.8: Retrieved optical depth vs. forest height (m) reported in Simard et al. (2011).

The results of the comparison are shown in Figure 4.8. Height values available in Simard et al. (2011) were subdivided into 1 m intervals. For each height interval, all the SMOS forest nodes were considered. The average value and standard deviation of τ were computed, and are represented by the continuous line and the error bars (respectively). There is a clear increasing trend, indicating an appreciable correspondence between the two variables. This is an interesting result, since the data were obtained by independent sources. In general, the standard deviation is slightly higher than 0.1. This is not exclusively due to an "error" in the strict sense. At L band, the optical depth is mostly dependent on the overall wood biomass, which is related to forest height but is also dependent on other forest properties.

4.5.2 Retrieved Soil Moisture

In general, the theory indicates that with the increase in vegetation biomass, there is decrease in the contribution of soil to the total emission, and therefore the SM information contained in the microwave signal decreases. This makes the retrieval of SM under forests difficult, since errors in the data and/or in

the algorithm can be comparable with the dynamic range of the variations due to SM itself. Some tests were done and results are reported in this Section.

The SM data analysis and testing was carried out for the SCANS and BERMS sites, since there are large homogeneous areas scarcely affected by RFI problems, and retrieved values of SM can be compared against measurements of extensive networks. In a first analysis, all the SMOS nodes surrounding the ground observed site (within buffer of 15 Km) were considered and the retrieved SM values, sensed by each SMOS node within the buffer, were averaged, algorithm performances obtained using different auxiliary data sets for LAI information were compared against each other. Different LAI inputs were passed to the forward model, viz., LAI input from ECOCLIMAP database (S6 model) and LAI input from MODIS database (S8 model) for the SM estimation. The outputs derived were compared with the ground observed SM for 33 SCAN/SNOTEL test sites (SMOS nodes, covering 80% forest cover and 40% forest cover) and 2 at BERMS test sites. In the first analysis, the conditions for filtering SMOS data regarded the distance of SMOS node from the axis of the swath (Xswath) and the RFI percentage. Outputs of Level 1 Prototype Processor (L1PP) have been used to detect and flag the unwanted emissions observed by SMOS. L1PP uses multi-angular SMOS data to detect the probable position of RFIs. A further Flagging algorithm has been developed by ESA and Level 2 team so that geolocated pixels are flagged depending on the intensity of RFI affecting them. Only pixels with Xswath lower than 300 km and RFI probability less than 5% have been considered, or both S6 and S8 model. The considered time interval was from June 1, 2010 to May 31, 2012. The test was carried out to find the most suitable LAI input into the model.

After that ECOCLIMAP was used as database for giving LAI to the forward model, and the analysis was repeated by considering the SMOS node closest to the ground site (node-to-site comparison) rather than averaged data. Different cases of Xswath limit and RFI filtering conditions were considered for the testing. The rationale behind putting such conditions was to understand the influence of Xswath limit and RFI filtering on the SM derived from SMOS data.

In the third analysis, the SM derived from SMOS data was compared with SM from other data sources (AMSRE). For this comparison, apart from two forest classes few nominal classes were also considered. The time interval considered for node-to-site analysis and comparison with AMSR-E products was from June 1, 2010 to May 31, 2011.

Finally an example of global map of SM, generated using ECOCLIMAP as LAI input and averaged within 4 days, is shown.

4.5.2.1 Results obtained by averaging among closest SMOS nodes with two kinds of auxiliary data

Tests of the SM retrieval algorithm were carried out with LAI inputs from different sources (viz., one from ECOCLIMAP (S6) and another case with MODIS (S8)) to compute the parameters of the simplified ATBD forest model (Kerr 2010) and (Kerr 2012) and to estimate how the SMOS algorithm performs at large scale over forests in different independent LAI data source.

4.5.2.1.1 SCAN/SNOTEL nodes

The SCAN/SNOTEL network includes several nodes in the US, in which multitemporal measurements of soil moisture and other environmental variables are available (Schaefer et al. 2007). The outputs of this network were successfully used in (Al Bitar et al. 2012) to compare ground measurements with SMOS retrieved SM values, mostly collected over agricultural fields. In this work, we have extended the analysis to forest nodes. As mentioned above, 33 SCAN/SNOTEL nodes, for which the ground measurements

were continuously available and with good accuracy, were selected, for each case of 80% (17 sites) and 40% (16 Sites) forest fraction. Then, the averaging of the SMOS nodes surrounding the node (within buffer of 15 Km) were considered, and the retrieved soil moisture values were averaged. The averaging includes from 1 SMOS node up to 7 nodes, for each SCAN/SNOTEL node depending upon the availability of ground data. The filtering criteria for SMOS data was, RFI < 1%, retrieved SM > 0, Tau <= 1.5 and Xswath ± 300. The considered time interval is from June 1, 2010 to May 31, 2012. By considering the multitemporal series, for each node we have compared the retrieved and the measured values of soil moisture. We have computed the RMS error, the bias and the correlation coefficient. For 50% of nodes, the RMS error is lower than 0.1 and the correlation coefficient is higher than 0.7. Further investigations about nodes with worse performance were carried out, in order to evaluate whether the errors are mostly due to noise in SMOS data, or inaccuracies of ground measurements.

As stated above, the testing was carried out by using LAI input, from each ECOCLIMAP (S6) and MODIS (S8) for the forward model. The statistical outputs (CC, RMSE and Bias) are shown in Table 4.1 and Table 4.2 for 40% and 80% forest fraction (FFO), respectively. As can been noticed in both tables, 4.1 and 4.2 in majority of the cases, the output of S6 was better compared to S8 under different Forest fractions on the standards of statistical parameters, however in some cases the RMSE is higher than 0.1.

Table 4.1: Correlation coefficient (CC), Root Mean Square Error (RMSE) and Bias (BA) for different SCAN nodes with respect to SMOS nodes averaged over 15Km buffer (with 40% forest) fraction for S6 and S8 algorithms.

			S6 (FFO=40%)			S8 (FFO=40%)		
SCAN Node	Lon	Lat	CC	RMSE	BA	CC	RMSE	BA
2008	-76.67	35.806	0.8125	0.0829	0.0111	0.8405	0.0761	0.0132
2016	-95.81	30.125	0.7114	0.0766	0.0622	0.6078	0.0714	0.0487
1133	-109.3	42.8	0.6172	0.0903	-0.0546	0.3721	0.1354	-0.097
969	-111.37	34.832	0.7295	0.1006	0.007	0.6363	0.1416	0.0099
1082	-111.03	43.779	0.551	0.11	-0.071	0.528	0.11	-0.064
387	-107.72	37.709	0.6055	0.1098	0.1031	0.5648	0.103	0.0892
424	-111.92	44.466	0.7272	0.062	-0.025	0.696	0.077	-0.058
493	-111.3	42.584	0.453	0.1	-0.001	0.333	0.108	-0.004
522	-109.99	40.895	0.5842	0.0897	-0.0704	0.4454	0.1366	-0.1171
707	-117.24	47.764	0.557	0.068	-0.022	0.605	0.066	-0.025
770	-111.28	42.867	0.95	0.03	0.016	0.94	0.029	-0.01
2053	-86.52	34.893	0.7316	0.0801	0.039	0.7237	0.0761	0.025
2059	-86.96	34.908	0.8392	0.1003	0.1	0.8454	0.0952	0.0944
2064	-88.67	33.639	0.8031	0.0664	-0.0329	0.8061	0.0693	-0.04
2075	-86.61	34.985	0.6965	0.0482	-0.0077	0.7179	0.0524	-0.0263
2090	-93.06	35.167	0.5693	0.0901	0.0497	0.5722	0.0782	0.0277

Table 4.2: Correlation coefficient (CC), Root Mean Square Error (RMSE) and Bias (BA) for different SCAN nodes with respect to SMOS nodes averaged over 15Km buffer (with 80% forest) fraction for S6 and S8 algorithms.

			S6 (FFO=80%)			S8 (FFO=80%)		
SCAN Node	Lon	Lat	CC	RMSE	BA	CC	RMSE	BA
312	-115.23	44.3	0.514	0.097	0.06	0.555	0.123	0.107
515	-120.66	48.72	0.674	0.157	-0.128	0.502	0.184	-0.158
577	-110.67	44.21	0.689	0.153	-0.004	0.646	0.14	-0.023
599	-121.08	46.36	0.343	0.11	0.038	0.408	0.085	0.01
623	-116.27	47.15	0.527	0.105	0.011	0.58	0.099	0.018
734	-121.06	47.38	0.7	0.062	0.024	0.726	0.05	0.005
747	-115.74	46.57	0.71	0.072	0.041	0.691	0.081	0.052
821	-118.43	44.66	0.617	0.105	0.047	0.661	0.096	0.033
2028	-76.67	40.67	0.374	0.095	0.001	0.302	0.126	0.007
2036	-77.93	40.72	0.724	0.067	0.031	0.693	0.065	0.028
2054	-86.1	34.87	0.838	0.091	-0.079	0.813	0.103	-0.08
2058	-87.05	34.43	0.826	0.105	-0.063	0.91	0.101	-0.072
2113	-86.8	34.19	0.701	0.073	-0.042	0.901	0.1	-0.071
2114	-88.2	32.61	0.476	0.121	-0.037	0.416	0.127	-0.04
2173	-87.99	34.82	0.737	0.063	-0.032	0.781	0.058	-0.036
2179	-87.46	34.18	0.731	0.126	0.106	0.797	0.14	0.126
1142	-115.87	46.47	0.811	0.08	0.066	0.754	0.086	0.067

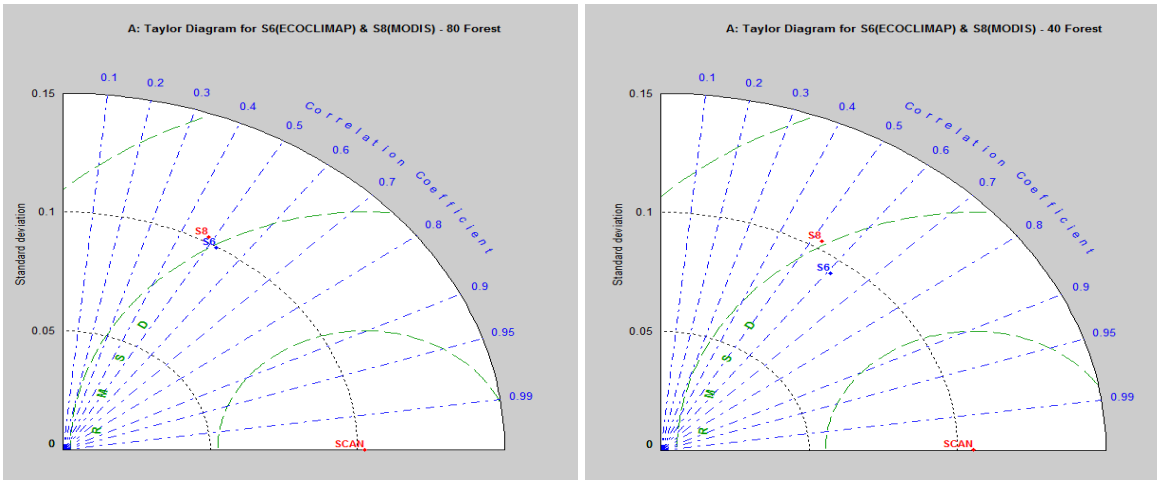

(a) (b)

Figure 4.9: Tailor Diagram of S6 and S8 Models for 80% (a) & 40% (b) Forest Cover

The results of overall CC, RMSE and Standard Deviation for the cases of S6 and S8 over 80% FFO and 40 % FFO are presented in the form of Taylor diagrams in Figure 4.9 (a) and(b). The figure shows that for both 80% and 40% forest cover cases, LAI input from ECOCLIMAP (S6) map is showing better

Correlation and lesser standard deviation with respect to the ground observation as compared with LAI input from MODIS into the model. Even the RMSE is lesser for S6 case than S8 for both forest cover. Details about the meaning and content of Taylor diagrams are given in Appendix B.

To understand in detail the spatial distribution of error in terms of geographical locations the CC and RMSE was plotted for all the nodes for 80% and 40% forest cover of SM obtained from S6 model. The results are shown in Figure 4.10 (a) and (b). It was observed that the algorithm works better in the Eastern forest nodes (mostly deciduous forests over flat soil) rather than in the Western sites (mostly coniferous forests in areas with relief).

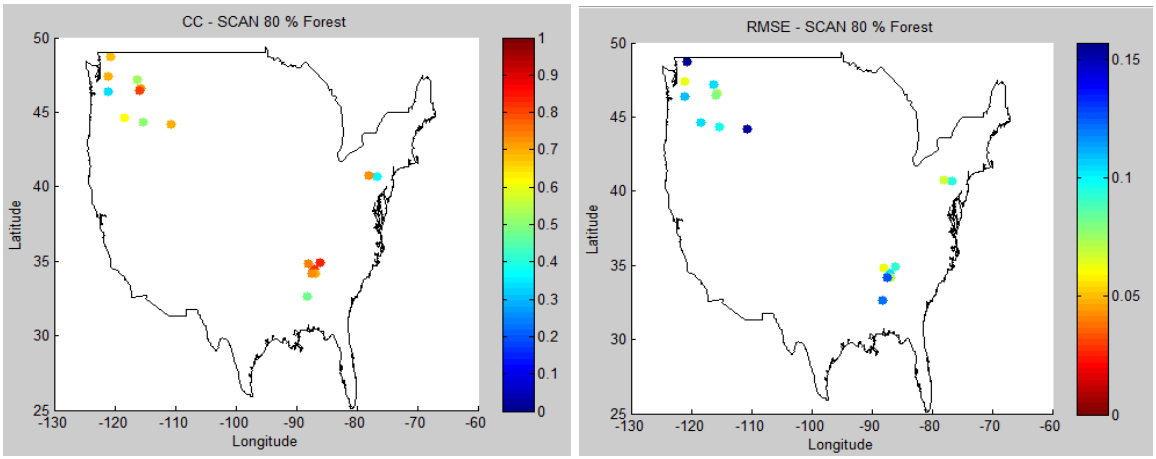

(a)

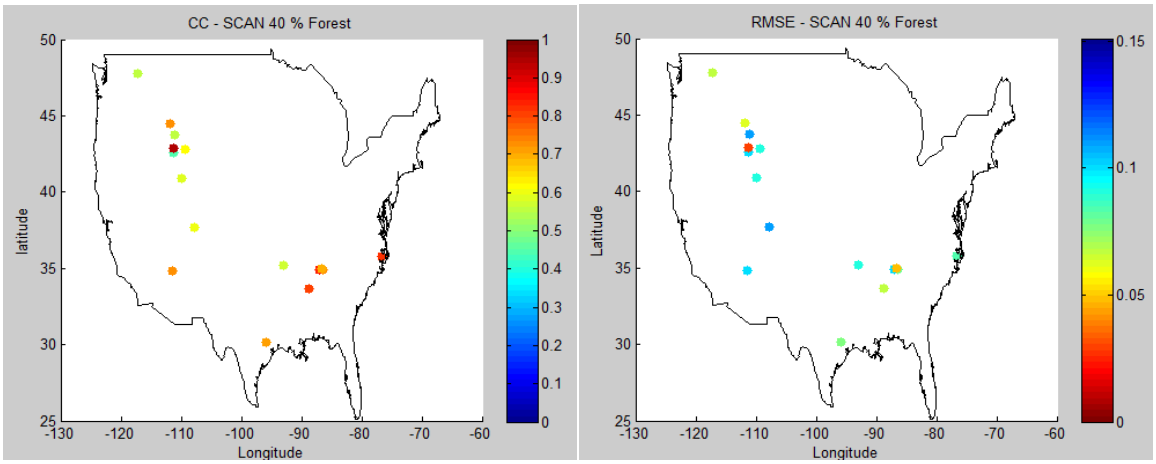

(b)

Figure 4.10: Correlation coefficient and Root Mean Square Error S6 Model

4.5.2.1.2 BERMS nodes

Similarly to SCAN nodes, a comparison between S6 and S8 model outputs of SMOS SM was done using ground measurements of SM at two BERMS sites (OJP and OBS). At FEN site, SM trend measured on

the ground was very flat: For 0-100 Julian days, the range of SM values was 0.06-0.1 and between 101 to 365 Julian days SM was close to 0.9. This site was not considered for the testing. H02, H75 and H95 were also not considered, since all these sites were very close to OJP site, which was falling almost at the center of SMOS grid DGG-Id-139040. For OBS site, averaging of two SMOS nodes (Dgg-Id-138014 & 138526) were done, whereas for OJP site only one SMOS node (DGG-Id-139040) was considered. As mentioned above, that for OJP site, the SMOS node and ground site was almost overlapping each other. It was found that for both the sites the results of the models were very similar, with a small edge over for the S6 model as shown in the Tylor diagrams of Figure 4.11.

Overall the results obtained at BERMS sites were better than SCAN/SNOTEL for both S6 and S8 particularly for RMSE, but the dynamic range of SM values was narrow.

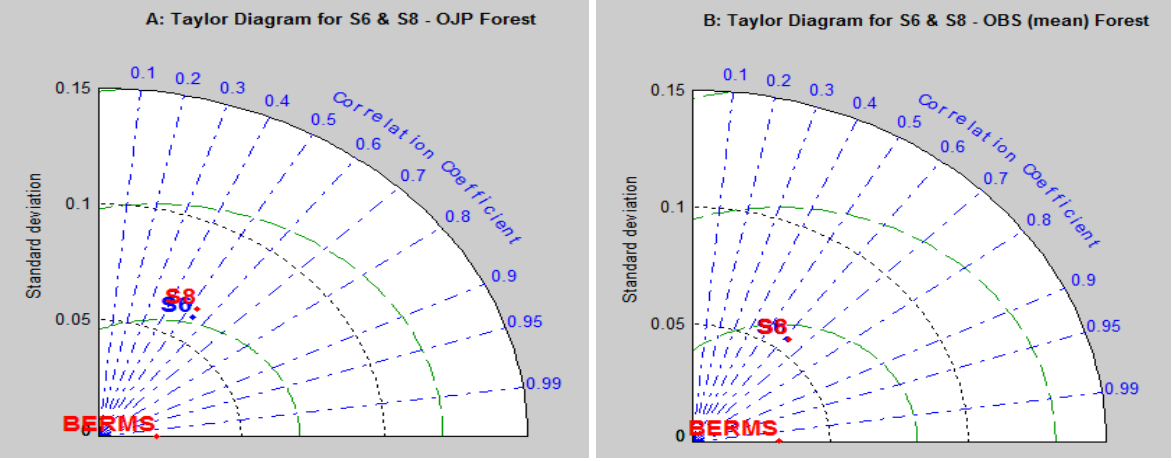

(a) (b)

Figure 4.11: Taylor Diagram for S6 and S8 model SMOS retrieved SM vs BERMS ground observed SM at OJP (a) and OBS (b) sites.

4.5.2.2 Node-to-site comparison results

In this section a detailed node to site comparison over selected sites for 80% and 40% Forest Fraction (FFO), between SMOS and ground measurements was done. Three different cases of Xswath limit and RFI filtering were taken.

- SMOS SM, node to site, Xswath< 300 km, RFI< 5%
- SMOS SM, node to site, Xswath< 300 km, RFI< 10%
- SMOS SM, node to site, no limitations on Xswath, RFI< 10%

The analysis was carried out for both SCAN and BERMS sites. For SCAN/SNOTEL nodes there were 16 sites for 40% FFO and 17 sites for 80% FFO sites for validation, whereas in case of BERMS, good ground data was available only for two sites (OBS and OJP) (details about OBS and OJP is mentioned in section (4.4.2).

4.5.2.2.1 SCAN/SNOTEL nodes

Case 1: SMOS SM, node to site, Xswath ± 300 km, RFI< 5%

Table 4.3: CC, RMSE and Bias for the case 1 for 80% and 40% forest fraction

40%					80%				
SMOS-DGG	SCAN	CC(C1)	RMSE(C1)	BA(C1)	SMOS-DGG	SCAN	CC(C1)	RMSE(C1)	BA(C1)
198946	387	0.23	0.12	-0.07	133834	515	0.95	0.05	0.02
165631	424	0.4	0.13	0.1	168711	577	0.75	0.12	0.07
173828	493	0.54	0.11	0.03	141510	599	0.08	0.15	-0.02
182542	522	0.53	0.11	0.07	138439	734	0.45	0.12	-0.05
144094	707	0.4	0.08	0.06	153302	821	0.63	0.16	-0.05
172804	770	0.52	0.1	0.04	150758	747	0.54	0.06	-0.03
202504	969	0.69	0.09	0.01	151782	1142	0.58	0.07	-0.005
169733	1082	0.27	0.12	0.06	219620	2028	0.45	0.09	-0.01
176401	1133	0.7	0.07	0.04	220124	2036	0.66	0.09	-0.03
246141	2016	0.69	0.07	-0.04	242115	2054	0.6	0.11	0.02
241088	2053	0.73	0.09	0.07	243647	2058	0.77	0.11	0.07
240573	2059	0.71	0.09	-0.07	244160	2113	0.66	0.09	-0.01
244149	2064	0.73	0.1	0.06	248760	2114	0.27	0.14	-0.03
240575	2075	0.75	0.09	0.06	239541	2173	0.5	0.09	0.06
					243133	2179	0.66	0.07	-0.01

Table 4.3 shows the CC, RMSE and Bias were obtained for each site with respect to ground observation. In general it has been found that the correlation coefficient is better in case of 40% forest fraction compared to 80% forest fraction sites. The same pattern is observed with the RMSE and Bias.

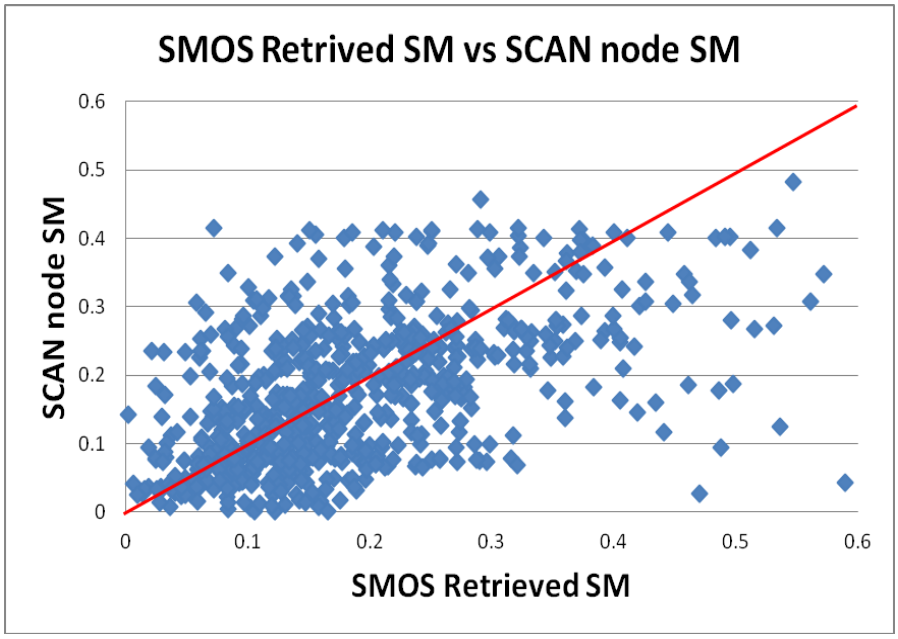

Figure 4.12: Scatterplot of All the SMOS retrieved SM and SCAN node SM obtained from case 1

Figure 4.12 shows the scatter plot of all the samples obtained from case 1 for both FFO. A general positive trend is observed, but with dispersion. In few cases of SM retrieval from SMOS, the retrieved values are higher than measured ones.

Case 2: SMOS SM, node to site, Xswath ± 300 km, RFI< 10%

Table 4.4: CC, RMSE and Bias for the case 2 of 80 % and 40% forest fraction

40%					80%				
SMOS-DGG	SCAN	CC(C2)	RMSE(C2)	BA(C2)	SMOS-DGG	SCAN	CC(C2)	RMSE(C2)	BA(C2)
198946	387	0.12	0.11	-0.06	133834	515	0.47	0.13	0.07
165631	424	0.32	0.14	0.1	168711	577	0.71	0.13	0.08
173828	493	0.4	0.13	0.04	141510	599	0.07	0.15	-0.01
182542	522	0.56	0.11	0.07	138439	734	0.58	0.11	-0.06
144094	707	0.19	0.12	0.06	153302	821	0.63	0.16	-0.05
172804	770	0.4	0.11	0.05	150758	747	0.6	0.1	-0.06
202504	969	0.69	0.09	0.01	151782	1142	0.6	0.08	-0.002
169733	1082	0.06	0.15	0.08	219620	2028	0.45	0.09	-0.01
176401	1133	0.7	0.08	0.05	220124	2036	0.66	0.09	-0.03
246141	2016	0.69	0.07	-0.04	242115	2054	0.6	0.11	0.02
241088	2053	0.73	0.09	0.07	243647	2058	0.77	0.11	0.07
240573	2059	0.71	0.09	-0.07	244160	2113	0.66	0.09	-0.01
244149	2064	0.73	0.1	0.06	248760	2114	0.27	0.14	-0.03
240575	2075	0.74	0.09	0.06	239541	2173	0.5	0.09	0.07
					243133	2179	0.66	0.07	-0.01

In case 2, with the increase in the percentage of samples affected by RFI, there is an obvious increase in RMSE, BA and decrease in correlation with respect to ground observation. In some specific sites, the effect is more severe. A detailed study of those critical sites shows that the fluctuation in the values of T_B is quite random and varies almost 100 K between horizontal and vertical polarization in a day. All these effects are attributed to the RFI issues.

Case 3: SMOS SM, node to site, no limitations on Xswath, RFI< 10%

Table 4.5: CC, RMSE and Bias for the case 3 for 80% and 40% forest fraction

40%					80%				
SMOS-DGG	SCAN	CC(C3)	RMSE(C3)	BA(C3)	SMOS-DGG	SCAN	CC(C3)	RMSE(C3)	BA(C3)
198946	387	0.2	0.12	-0.07	133834	515	0.33	0.16	0.08
165631	424	0.3	0.13	0.09	168711	577	0.26	0.37	0.05
173828	493	0.33	0.13	0.04	141510	599	0.26	0.13	-0.001
182542	522	0.49	0.13	0.07	138439	734	0.49	0.1	-0.04
144094	707	0.36	0.1	0.05	153302	821	0.52	0.16	-0.01
172804	770	0.36	0.12	0.04	150758	747	0.42	0.17	-0.07
202504	969	0.63	0.09	0.01	151782	1142	0.5	0.09	0.005
169733	1082	0.01	0.17	0.09	219620	2028	0.4	0.1	0.004
176401	1133	0.63	0.09	0.06	220124	2036	0.51	0.11	-0.03
246141	2016	0.55	0.09	-0.05	242115	2054	0.58	0.11	0.03
241088	2053	0.65	0.1	0.07	243647	2058	0.75	0.13	0.09
240573	2059	0.66	0.08	-0.05	244160	2113	0.63	0.1	0.01
244149	2064	0.62	0.12	0.07	248760	2114	0.25	0.14	0.003
240575	2075	0.7	0.1	0.06	239541	2173	0.21	0.13	0.09
					243133	2179	0.6	0.08	0.001

For SMOS, SM retrieval error also depends on the part of the instrument field of view where the data were collected. For this reason, any representative overall error budget can only be given as an average over the SMOS swath. Study (Meirold-Mautner et al. 2009), has shown that the BA in SMOS retrieval depends on the distance of the grid points to the centre of the satellite track (Xswath). In case 3, the restriction of Xswath for filtering the data was removed. It was observed that gridpoints within ±300Km from the centre of the track shows smaller BA than grid points greater than ±300Km. Also there is degradation in the RMSE and CC due to Xswath effect.

Notably the spread in the data diminishes when observing grid points closer to the track. A small distance to the track ensures a proximity to bore-sight which has been shown to have the smallest BA in TB_s (Meirold-Mautner et al. 2009),

Figure 4.13 shows a general comparison between case 1, case2 and case 3 regarding overall correlation coefficient, RMSE, Bias, and % of valid samples, obtained by simply dividing the overall number of valid samples by the overall numbers of samples with available ground truth. As expected, there is slight worsening from case 1 to case 2 and from case 2 to case 3, for both 40% forest cover and 80% forest cover. The percentage of valid samples however is significantly increased in case 3.

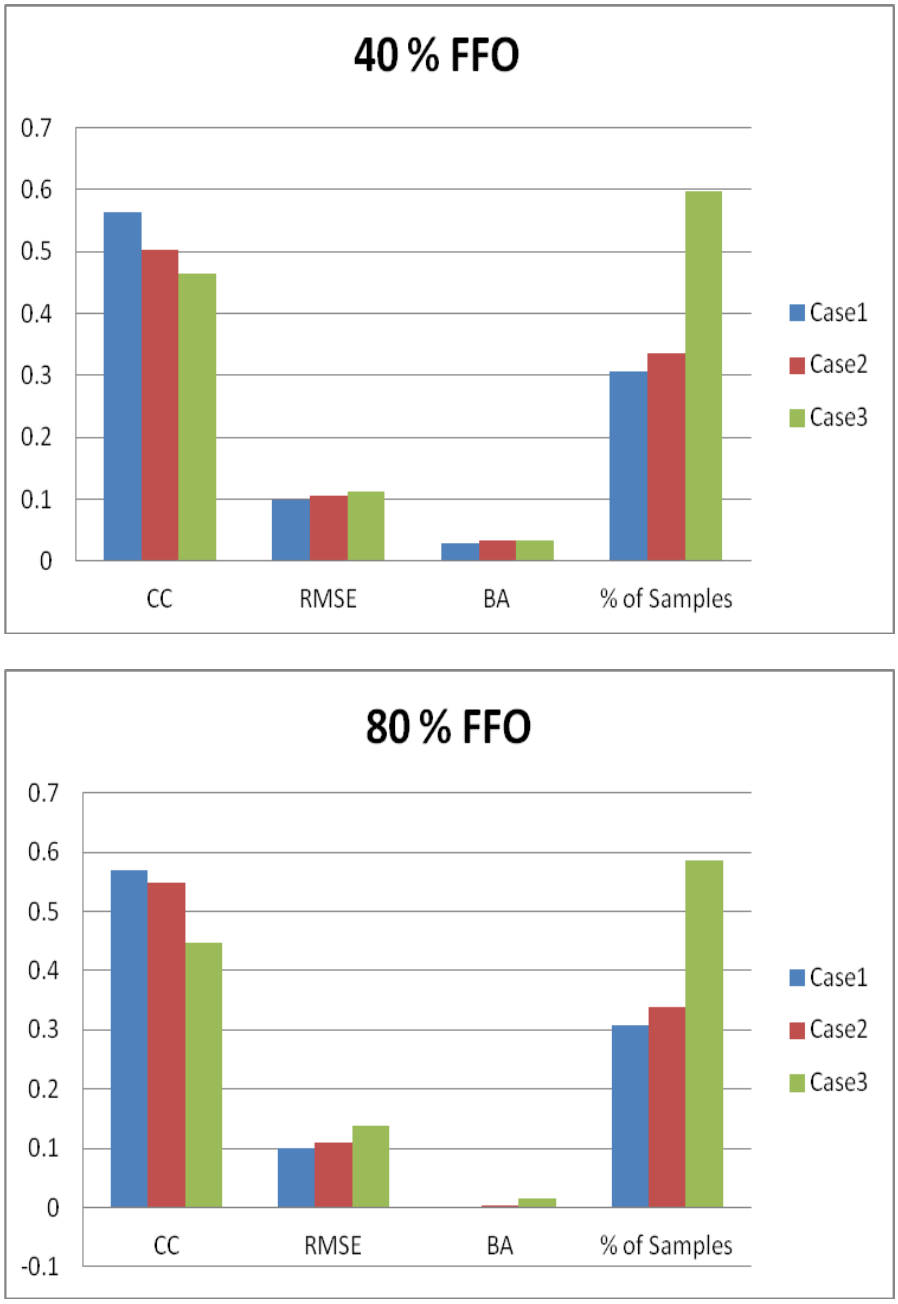

Figure 4.13: Bar charts showing CC, RMSE, BA and % of samples obtained for each case for 40 % FFO and 80 % FFO.

4.5.2.2.2 BERMS nodes

SMOS SM obtained from S6 model is compared with the SM observed at OBS and OJP at BERMS site. Similar to SCAN nodes, for BERMS also three cases were considered. The results are shown in Table 4.6. There is a good Correlation between the satellite measured SM and ground measured SM for both ground sites for case 1. Here, only the results of OBS are mentioned since for OBS site there is a small difference between three cases, but for OJP, the difference is huge. Although this noticeable difference for OJP in case 2 and case 3 is mainly due to inclusion of 2-3 major outliers in the SMOS retrieved SM.

Table 4.6: CC, RMSE and Bias for three cases at OBS site.

	Case 1			Case 2			Case 3		
BERM node	**CC**	**RMSE**	**BA**	**CC**	**RMSE**	**BA**	**CC**	**RMSE**	**BA**
OBS	0.6374	0.0706	0.0273	0.6884	0.0715	0.021	0.6514	0.0758	0.0336

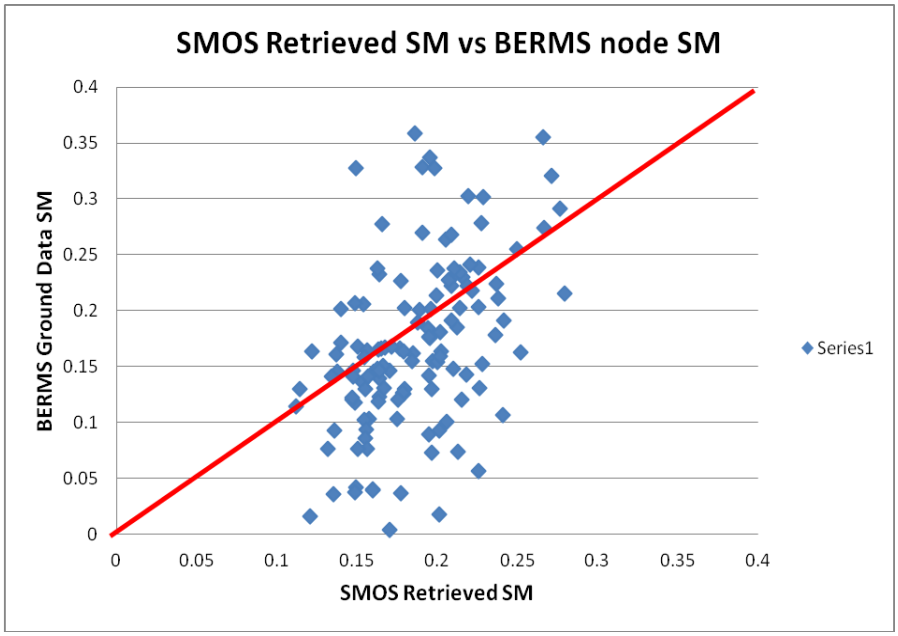

Figure 4.14: Scatterplot of all the SMOS retrieved SM vs BERMS Ground observed SM obtained from case 1.

4.5.2.3 SMOS SM comparison with SM obtained from AMSR_E Data.

In this section comparisons between SM derived from SMOS data and SM derived from AMSR-E products (NSDIC and VUA) are shown. SM derived from descending over pass data of AMSR-E was processed for the duration from June 1st 2010 till May 30th 2011. The analysis was carried out for SCAN/ SNOTEL sites only. Apart from 40% and 80% FFO nodes, few nodes with low vegetation (nominal class) were also taken as a reference. In total 31 sites were considered, viz., 15 nodes with 80% FFO, 14 nodes with 40% FFO and 2 nodes of low vegetation classes.

All the three SMOS datasets were filtered based on criteria adopted in case 2 of section 4.5.2.2 viz., RFI <=10% and Xswath ± 300Km.

For AMSR-E products the following filtering conditions were applied:

Successful retrieval and SM >=0 for VUA retrieval results;
Successful retrieval and SM>=0 for NSIDC retrieval results.

Figure 4.15 (a), (b) and (c), shows the results of comparisons between SM data products and ground measurements as scatter plots for different forest fractions. Red (square), black (diamond) and blue (plus) symbols represents SM data of SMOS, VUA and NSIDC respectively. Figure 4.15 (a), (b) and (c) shows results for 40 % FFO, 80 % FFO and low vegetation class nodes respectively. As expected, the effect of vegetation thickness and frequency is quite visible on the performance of the three algorithms. The performance tends to worsen when the forest fraction increases and/or the frequency of the receiving channels increases. The results indicates that, in all the three cases, SM derived from SMOS data is better correlated with the ground data as compared with UVA or NSDIC outputs. Improvement in correlation for UVA and NSIDC with respect to ground observations is noticed as we move towards low vegetation conditions (viz., 40 % FFO and low vegetation class). For forest pixels, a high dispersion of SM values retrieved by LPRM is observed. Soil moistures retrieved by the AMSR-E L2b algorithm (X band) show a very low dynamic range, when compared to variations of measured SM.

Another study was done to see the total number of successful SM retrievals, before and after applying the filters on SMOS and UVA data. This was useful to understand the total available data and amount of data discarded due to problem of RFI and Xswath (in case of SMOS) and unsuccessful retrieval and SM <=0 (in case of UVA). Since the results of NSIDC data (as seen from figure 4.15 (a), (b) and (c)) were not so good, therefore for this analysis, it was not considered. In most of the cases of both 40 % and 80 % FFO along with low vegetation classes, the number of retrievals for UVA is higher as compared to SMOS. SMOS data and UVA data, were picked up for the same duration (same Julian days) for calculating statistical parameters.

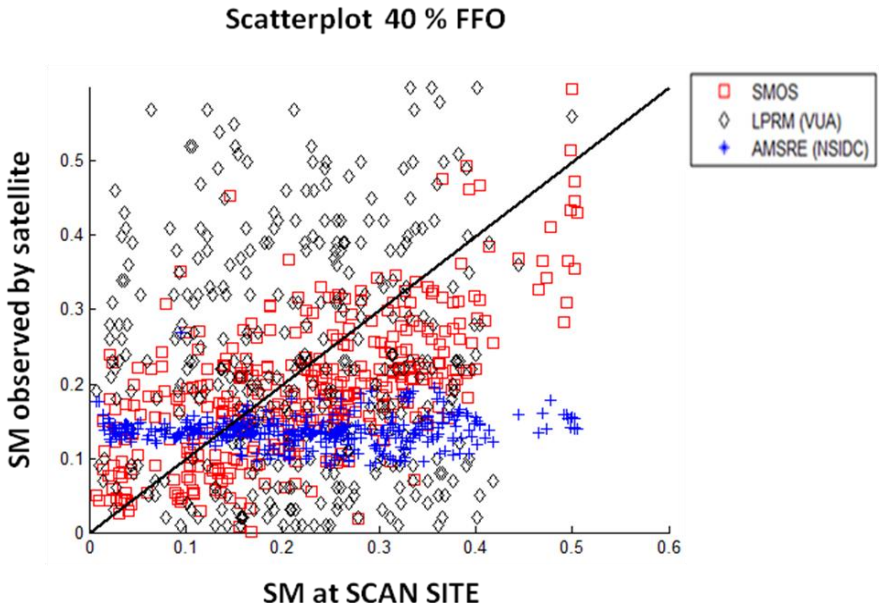

(a)

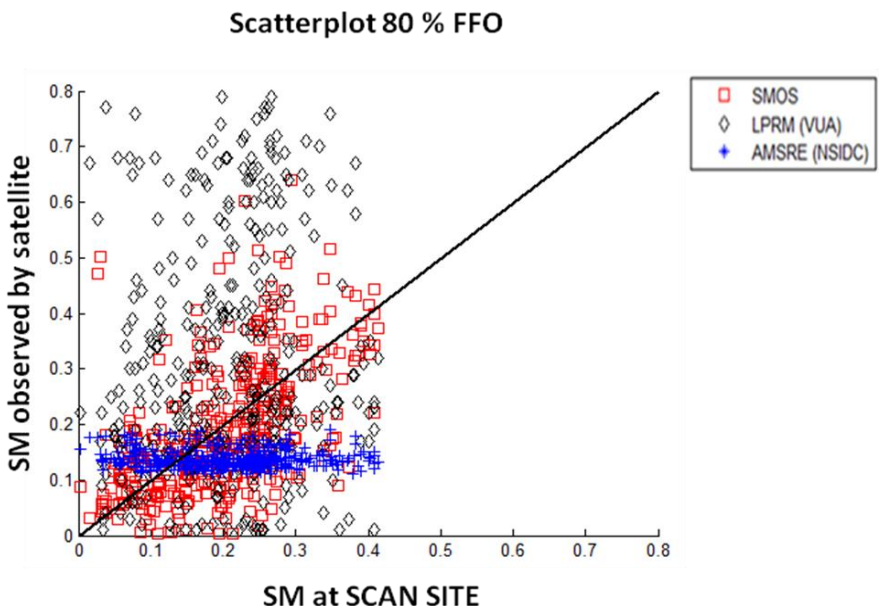

(b)

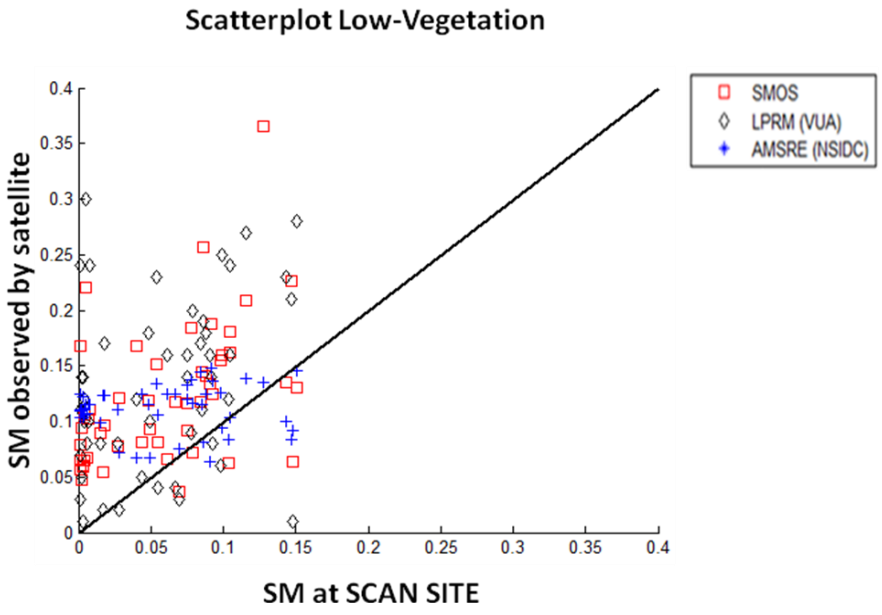

(c)

Figure 4.15: Comparison of Soil Moisture Retrieved from different algorithms vs. SCAN/SNOTEL Ground Observation over different forest land covers (40% forest (a), 80% forest (b) and low vegetation (c)). Results are given in form of a global scatterplot, including all nodes considered in tables 4.3 (40 and 80 % FFO and two nodes of low vegetation.

The percentages of available samples (total available samples and successful retrieved sample) are higher in case of UVA, whereas for SMOS the percentage is lower, Table 4.7 and 4.8 summarize the results.

Table 4.7: Correlation coefficient (CC) and Root Mean Square Error (RMSE) for each node of SMOS node under different forest fractions covered area with respect to the ground observed SM.

40%							
SCAN	GD	SMOS (Total)	SMOS (After Filter)	% of Samples	CC	RMSE	BA
387	350	124	40	32.25806	0.12	0.11	-0.06
424	262	147	55	37.41497	0.32	0.14	0.1
493	365	143	50	34.96503	0.4	0.13	0.04
522	365	134	46	34.32836	0.56	0.11	0.07
707	362	202	74	36.63366	0.19	0.12	0.06
770	365	144	49	34.02778	0.4	0.11	0.05
969	365	177	67	37.85311	0.69	0.09	0.01
1082	363	140	48	34.28571	0.06	0.15	0.08
1133	365	126	38	30.15873	0.7	0.08	0.05
2016	350	211	47	22.27488	0.69	0.07	-0.04
2053	334	217	84	38.70968	0.73	0.09	0.07
2059	312	216	48	22.22222	0.71	0.09	-0.07
2064	338	215	81	37.67442	0.73	0.1	0.06
2075	336	220	84	38.18182	0.74	0.09	0.06
80%							
SCAN	GD	SMOS (Total)	SMOS (After Filter)	% of Samples	CC	RMSE	BA
515	365	137	45	32.84672	0.47	0.13	0.07
577	365	140	48	34.28571	0.71	0.13	0.08
599	365	138	50	36.23188	0.07	0.15	-0.01
734	365	138	48	34.78261	0.58	0.11	-0.06
821	296	142	27	19.01408	0.63	0.16	-0.05
747	365	171	59	34.50292	0.6	0.1	-0.06
1142	365	150	50	33.33333	0.6	0.08	-0.002
2028	365	199	86	43.21608	0.45	0.09	-0.01
2036	338	191	68	35.60209	0.66	0.09	-0.03
2054	338	211	84	39.81043	0.6	0.11	0.02
2058	337	218	82	37.61468	0.77	0.11	0.07
2113	311	219	76	34.7032	0.66	0.09	-0.01
2114	165	217	42	19.35484	0.27	0.14	-0.03
2173	279	216	68	31.48148	0.5	0.09	0.07
2179	335	215	86	40	0.66	0.07	-0.01
Low-Vegetation							
SCAN	GD	SMOS (Total)	SMOS (After Filter)	% of Samples	CC	RMSE	BA
2018	365	209	41	19.61722	0.6	0.06	0.03
2160	365	141	37	26.24113	0.6	0.09	0.05

Table 4.8: Correlation coefficient (CC) and Root Mean Square Error (RMSE) for each node of LPRM node under different forest fractions covered area with respect to the ground observed SM.

40%							
SCAN	GD	LPRM (Total)	LPRM (After filter)	% of Samples	CC	RMSE	BA
387	350	347	139	40.05764	-0.3188	0.5157	-0.4313
424	262	347	165	47.55043	0.349	0.1056	-0.0737
493	365	347	171	49.27954	0.38889	0.2007	-0.1481
522	365	347	167	48.1268	0.0709	0.1445	0.0946
707	362	347	8	2.305476	-0.0228	0.2392	0.275
770	365	347	165	47.55043	0.2359	0.1437	-0.0893
969	365	347	161	46.39769	0.3006	0.2052	0.1751
1082	363	347	171	49.27954	-0.3076	0.236	-0.1608
1133	365	347	195	56.19597	0.0597	0.1631	0.1215
2016	350	347	237	68.29971	0.1493	0.0921	-0.0367
2053	334	347	194	55.90778	0.6577	0.1621	0.1441
2059	312	347	208	59.94236	0.4583	0.1033	-0.0267
2064	338	347	237	68.29971	0.6238	0.237	-0.1993
2075	336	347	194	55.90778	0.6938	0.1581	0.1406
80%							
SCAN	GD	LPRM (Total)	LPRM (After filter)	% of Samples	CC	RMSE	BA
515	365	347	174	50.14409	-0.2093	0.6943	-0.6532
577	365	347	150	43.22767	-0.2514	0.3769	-0.3318
599	365	347	241	69.45245	0.0236	0.2231	-0.1079
734	365	347	226	65.12968	-0.0395	0.3977	-0.282
821	296	347	210	60.51873	0.0548	0.3773	-0.2743
747	365	347	252	72.62248	-0.1626	0.7526	-0.7199
1142	365	347	254	73.19885	-0.2935	0.6382	-0.582
2028	365	347	88	25.36023	0.2407	0.1895	0.1804
2036	338	347	242	69.74063	0.5776	0.3124	-0.1819
2054	338	347	233	67.14697	0.5565	0.2769	-0.1922
2058	337	347	223	64.26513	0.5166	0.1298	0.087
2113	311	347	216	62.24784	0.5632	0.0865	0.0256
2114	165	347	152	43.80403	-0.2354	0.2513	0.2332
2173	279	347	257	74.0634	0.7027	0.2893	-0.2629
2179	335	347	224	64.55331	0.5434	0.1642	-0.1201
Low-Vegetation							
SCAN	GD	LPRM (Total)	LPRM (After filter)	% of Samples	CC	RMSE	BA
2018	365	365	244	66.84932	0.65	0.06	0.05
2160	365	365	176	48.21918	0.74	0.14	0.11

4.6 Conclusion

Results obtained using the prototype SMOS L2 algorithm have been described. Two algorithms were tested, one with the input of LAI from ECOCLIMAP (S6) and the other from MODIS (S8). S6 algorithm was found to work slightly better with respect to S8 algorithm in more than 80% of the total samples selected for the tests at SCANS (US) and BERMS (Canada). For 50% of nodes, the RMS error is lower than 0.09 and the correlation coefficient is higher than 0.7. It was observed that the algorithm works better in the Eastern forest nodes (mostly deciduous forests over flat soil) rather than in the Western sites (mostly coniferous forests in areas with relief) over the forests in US. However the interpretation of this result needs further investigations.

The optical depth map obtained from SMOS data processing are compared with optical depth map provided by LPRM (VUA). Differences are important, since SMOS is mostly sensitive to forest cover, while AMSR-E is also influenced by low vegetation.

The global map of optical depth has been compared with the tree height using LIDAR data shows a clear increasing trend, indicating an appreciable correspondence between the two variables.

Finally the results of SM obtained from SMOS are compared with LPRM and NDICS SM. The performance of LPRM algorithm (C and X band) is inferior with respect to SMOS one (L band) over most of the pixels. The worsening however is moderate over low vegetation, and becomes strong when the forest fraction increases. For forest pixels, a high dispersion of SM values retrieved by LPRM is observed. Soil moistures retrieved by the AMSR-E L2b algorithm (X band) show a very low dynamic range, when compared to variations of measured SM. This problem is observed for all forest fractions.

Publications:

Paper

- Y. Singh, P. Ferrazzoli, R. Rahmoune, Flood Monitoring using Microwave Passive Remote Sensing (AMSR-E) in part of Brahmaputra basin, India'. International Journal of Remote Sensing, 2013 Vol. 34, No. 14, 4967–4985, http://dx.doi.org/10.1080/01431161.2013.786194

- R. Rahmoune, P. Ferrazzoli, Y. Singh, Y. Kerr, P. Richaume, A. Albitar, 'SMOS retrieval results over forests: Comparisons with independent measurements'. (submitted in IEEE-JSTARS)

Conference Proceedings

- P. Ferrazzoli, R. Rahmoune, Y. Singh, Y. Kerr, P. Richaume, A. Al Bitar, C. Moisy, 'SMOS L2 Retrieval Results Over Forests And Tests', at ESA Living Planet Symposium 9 - 13 September, 2013 Edinburgh, United Kingdom.

- R. Rahmoune, Y. Singh, P. Ferrazzoli, Y. Kerr, P. Richaume, A. Albitar, C. Moisy, 'SMOS L2 Retrieval Results Over the American Continent And Comparisons With Independent Data Sources' , at IGARSS-2013, 21-26 July, Melborne, Australia .

- R. Rahmoune, Y. Singh, P. Ferrazzoli, Y. Kerr, P. Richaume, A.Albitar, C. Moisy, Retrieving Soil Moisture over North American Forests: SMOS results and comparisons with previous algorithms, , at SMOS Land Application Workshop-2013, 1-3 July, Frascati(Rome), Italy.

- R. Rahmoune, Y. Singh, P. Ferrazzoli, Y. Kerr, P. Richaume, A.Albitar, R. Magagi, C. Moisy, 'Improved SMOS Soil Moisture Algorithm & Validation over North America Forests' , at SMOS Land Application Workshop-2013, 25-27 Feburary, Frascati(Rome), Italy.

- P. Ferrazzoli, R. Rahmoune, Y. Singh, Y. Kerr, P. Richaume, A. Al Bitar, C. Moisy, "Estimate of forest parameters and comparisons with independent measurements",at SMOS Land Application Workshop-2013, 25-27 Feburary, Frascati(Rome), Italy.

- Y. Singh, P. Ferrazzoli, R. Rahmoune 'Flood Monitoring using Microwave Passive Remote Sensing (AMSR-E) in part of Brahmaputra basin, India ' at IGARSS-2012, 22-27 July, Munich, Germany

- Y. Singh, R. Chakraborty, P. Ferrazzoli, Testing flood monitoring methods using AMSR-E in Indian sites MICRORAD – 2012, 5-9 March.

Bibliography

Al Bitar, A., Leroux, D., Kerr, Y. H., Merlin, O., Richaume, P., Sahoo, A. and Wood, E. F., 2012, Evaluation of SMOS Soil Moisture Products Over Continental U.S. Using the SCAN/SNOTEL Network: IEEE Trans. on Geosci. and Remote Sens., v. 50, p. 1572-1586.

Alsdorf, D. E., Bates, P., Melack, J., Wilson, M. and Dunne, T. , 2007, Spatial and temporal complexity of the Amazon flood measured from space: Geophysical Research Letters, v. 34, p. L08402.

Alsdorf, D. E., Melack, J. M., Dunne, T., Mertes, L. A. K., Hess, L. L. and Smith, L. C. , 2000, Interferometric radar measurements of water level changes on the Amazon flood plain: Nature, v. 404, p. 174-177.

Anterrieu, E. and Camps, A., 2008, On the reduction of the systematic error in imaging radiometry by aperture synthesis: a new approach for the smos space mission, IEEE MicroRad.

Barton, I. J., 1978, A case study of microwave radiometer measurements over bare and vegetated surfaces: Journal of Geophysical Research, v. 83, p. 3515-3517.

Behari, J., 2005, Microwave Dielectric Behavior of Wet Soils: Remote Sensing and Digital Image Processing.

Beljaars, C. M., Viterbo, P., Miller, M. J. and Betts, A. J., 1996, The anomalous rainfall over the United States during July 1993: sensitivity to land surface parameterization and soil moisture anomalies, Monthly Weather Review, p. 362-383.

Berger, M., Kerr, Y., Font, J., Wigneron, J.-P., Calvet, J.-C., Saleh, K., Lopez-Baeza, E., Simmonds, L., Ferrazzoli, P., Van de Hurk, B., Viterbo, P., Waldteufel, P., Petitcolin, F., Van de Griend, A., Attema, E. and Rast, M., 2003, Measuring the moisture in the earth's soil—Advancing the science with ESA's SMOS mission, ESA Bulleteen, p. 41-45.

Bindlish, R., 2009, Role of Passive Microwave Remote Sensing in Improving Flood Forecasts: IEEE Journal iof Selected Topics in Applied Eart6h Observation and Remote Sens., v. 6, p. 112-116.

Birchak, J. R., Gardner, C.G., Hipp, J.E. and Victor, J.M, 1974, High dielectric constant microwave probes for sensing soil moisture: IEEE Proceedings, v. 62, p. 92-98.

Bot, A. and Benites, J., 2005, The importance of soil organic matter. Key to drought resistant soil and sustained food production, FAO Soils Bulletin 80, Rome, Italy, FAO.

Brady, N. C. and Weil, R.R., 2003, Elements of the Nature and Properties of Soils, v. 2nd edn.: NJ, Prentice Hall.

Brakenridge, G. R., Nghiem, S.V., Anderson, E. and Mic, R., 2007a, Orbital microwave measurement of river discharge and ice status: Water Resource Research, v. 43.

Brakenridge, G. R., Nghiem, S. V., Anderson, E. and Mic, R., 2007b, Orbital Microwave Measurement of River Discharge and Ice Status: Water Resources Research, v. W04405, p. 5238.

Brivio, P. A., Colombo, R., Maggi, M. and Tomasoni, R., 2002, Integration of remote sensing data and

GIS for accurate mapping of flooded areas: International Journal of Remote Sensing, v. 23, p. 429-441.

Brown, S., Ruf, C. and Lyzenga, D., 2006, An emissivity-based wind vector retrieval algorithm for the WindSat polarimetric radiometer: IEEE Transactions on Geoscience and Remote Sensing, v. 44, p. 611-621.

Brunfeldt, D. R. and Ulaby, F. T., 1984, Measured microwave emission and scattering in vegetation canopies: IEEE Trans. on Geosci. and Remote Sens., v. GE-22, p. 520-524.

Caizzone, S., Ferrazzoli, P., Guerriero, L. and Pierdicca, N., 2009, Modeling backscattering variations due to flooding over vegetated surfaces: Italian Journal of Remote Sensing, v. 3, p. 2537-2549.

Calvet, J. C., Wigneron, J.P., Chanzy, A., Raju, S. and Laguerre, L. , 1995, Microwave dielectric properties of a silt-loam at high frequencies: IEEE Trans. on Geosci. and Remote Sens., v. 33, p. 634-642.

Camps, A., 1996, Application of interferometric radiometry to Earth observation., Universitat Politµecnica de Catalunya.

Camps, A., Bara, J., Corbella, I. and Torres, F., 1997, The processing of hexagonally sampled signals with standard rectangular techniques: Application to 2-d large aperture syn- thesis interferometric radiometer: IEEE Trans. on Geosci. and Remote Sens., v. 35(1), p. 183-190.

Camps, A., Vall-llossera, M., Corbella, I., Du_o, N. and Torres, F., 2008a, Improved image reconstruction algorithm for aperture synthesis radiometers: IEEE Trans. on Geosci. and Remote Sens., v. 46(1), p. 146-158.

Carr, D., Kahn, R., Sahr, K. and Olsen, T., 1997, ISEA Discrete Global Grids: Statistical Computing & Statistical Graphics Newsletter, v. 8, p. 31-39.

Chanzy, A., Raju, S. and Wigneron, J.-P. , 1997, Estimation of soil microwave effective temperature at L and C bands: IEEE Trans. on Geosci. and Remote Sens., v. 35, p. 570-580.

Chauhan, N. S., Lang, R. H. and Ranson, K. J., 1991, Radar modeling of a boreal forest: IEEE Journal iof Selected Topics in Applied Eart6h Observation and Remote Sens., v. 29, p. 627-638.

Choudhury B. J. and Jackson, T. C., 1987, Monitoring global vegetation using Nimbus-7 37 GHz data: Some empirical relations: International Journal of Remote Sensing, v. 8, p. 1085-1090.

Choudhury, B. J., 1989, Monitoring global land surface using nimbus-7 37GHz data, Theory and examples: International Journal of Remote Sensing, v. 10, p. 1579-1605.

Choudhury, B. J., Schmugge, T.J. and Mo, T., 1982, A simple parameterization of e®ective soil temperature for microwave emission: Journal of Geophysical Research, p. 1301-1304.

Choudhury, B. J., Schmugge, T.J., Chang, A.T.C. and Newton, R.W. , 1979, Effect of surface roughness on the microwave emission of soils: Journal of Geophysical Research, v. 84, p. 5699-5705.

Chukhlantsev, A. A., 2006, Microwave radiometry of vegetation canopies. , v. Advances in Global Change Research, Springer.

Crow, W. T., Bindlish, R. and Jackson T. J. , 2005, The added value of spaceborne passive microwave soil moisture retrievals for forecasting rainfall–runoff partitioning: Geophysical Research Letters, v. 32.

Curtis, J. O., 2001, Moisture effect on the dielectric properties of soils: IEEE Trans. on Geosci. and Remote Sens., v. 39, p. 125-128.

De Lannoy, G. J. M., Houser, P. R., Verhoest, N. E. C., Pauwels, V. R. N. and Gish, T. J. , 2007, Upscaling of point soil moisture measurements to field averages at the OPE3 test site: Journal of Hydrology, v. 343, p. 1-11.

De Lannoy, G. J. M., Ufford, J., Sahoo, A. K., Dirmeyer, P. and Houser, P. R., 2011, Observed and simulated water and energy budget components at SCAN sites in the lower Mississippi Basin: Hydrological Processes, v. 25, p. 634-649.

De Roo, R. D., Du, Y., Ulaby, F. T. and Dobson, M. C., 2001, A semi-empirical backscattering model at L-band and C-band for a soybean canopy with soil moisture inversion: IEEE Trans. on Geosci. and Remote Sens., v. 39, p. 864-872.

Del Frate, F., and Wang, L., 2001, Sunflower biomass estimation using a scattering model and a neural network algorithm: International Journal of Remote Sensing, v. 22, p. 1235-1244.

Del Frate, F., Ferrazzoli, P., & Schiavon, G. , 2003, Retrieving soil moisture and agricultural variables by microwave radiometry using neural networks: Remote Sens. Environ, v. 84, p. 174-183.

Della Vecchia, A., Ferrazzoli, P., Guerriero, L., Rahmoune, R., Paloscia, S., Pettinato, S. and Santi, E., 2010, Modeling the Multifrequency Emission of Broadleaf Forests and Their Components: IEEE Trans. on Geosci. and Remote Sens., v. 48.

Della Vecchia, A., Ferrazzoli, P., Wigneron, J.-P. and Grant, J., 2007, Modeling forest emissivity at L band and a comparison with multitemporal measurements: ieee Geosciences Remote Letters, v. 4, p. 508-512.

Della Vecchia, A., Saleh, K., Ferrazzoli, P., Guerriero, L., & Wigneron, J.-P., 2006, Simulating L-band emission of coniferous forests using a discrete model and a detailed geometrical representation: IEEE Trans. on Geosci. and Remote Sens., v. 3, p. 364-368.

Delworth, T., and Manabe, S., 1988, The influence of potential evaporation on the variability of simulated soil wetness and climate: Journal of Climate, v. 13, p. 2900-2922.

Dobson, M. C., Ulaby, F.T., Hallikainen, M.T. and El-Rayes, M.A., 1985, Microwave Dielectric Behaviour of Wet Soil Part II: Dielectric Mixing Models: IEEE Trans. on Geosci. and Remote Sens., v. 23, p. 35-46.

Dutta, S., Medhi, H., Karmaker, T., Singh, Y., Prabu I. and Dutta, U., 2010, Probabilistic Flood Hazard Mapping For Embankment Breaching: ISH Journal of Hydraulic Engineering, v. 16, p. 15-25.

Eagleman, J. R., and Lin, W.C., 1976, Remote sensing of soil moisture by a 21-cm passive radiometer: Journal of Geophysical Research Oceans and Atmospheres, v. 82, p. 3108-3118.

Entekhabi, D., and I. Rodriguez-Iturbe 1994, Analytical framework for the characterization of the space-

time variability of soil moisture: Advance Water Research, v. 17, p. 35-45.

Entekhabi, D., Rodrigues-Iturbe, I., and Castelli, F., 1996, Mutual interaction of soil moisture state and atmospheric processes: Journal of Hydrology, v. 184, p. 3-17.

Escorihuela, M. J., Kerr, Y. H., de Rosnay, P., Wigneron, J.-P., Calvet, J.-C., and Lemaitre, F., 2007, A simple model of the bare soil microwave emission at L-band: IEEE Trans. on Geosci. and Remote Sens., v. 45, p. 1978-1987.

FAO, 1988, UNESCO Soil Map of the World, UNESCO, Rome World Soil Resources

FAO, 2000, The status of forests: the Global Forest Resources Assessment 2000.

Ferraro, R. R., and Marks, G. F., 1994 Effects of Surface Conditions on Rain Identification Using the SSM/I: Remote Sensing Reviews, v. 11, p. 195-209.

Ferraro, R. R., Smith, E. A., Berg, W., and Huffman, G. J., 1998, Screening Methodology for Passive Microwave Precipitation Retrieval Algorithms: Journal of Atmospheric Sciences, v. 55, p. 1583-1600.

Ferrazzoli, P. and Guerriero, L., 1995, Radar sensitivity to tree geometry and woody volume: A model analysis: IEEE Trans. on Geosci. and Remote Sens., v. 33, p. 360-371.

Ferrazzoli, P. and Guerriero, L., 1996, Passive microwave remote sensing of forests: A model investigation: IEEE Trans. on Geosci. and Remote Sens., v. 34, p. 433-443.

Ferrazzoli, P., Guerriero, L. and Wigneron, J.-P. , 2002, Simulating L-band emission of forests in view of future satellite applications: IEEE Trans. on Geosci. and Remote Sens., v. 40.

Ferrazzoli, P., Guerriero, L., Paloscia, S., Pampaloni, P. and Solimini, D. 1992, Modelling polarizationproperties of emission from soil covered with vegetation: IEEE Trans. on Geosci. and Remote Sens., v. 30, p. 157-165.

Ferrazzoli, P., Rahmoune, R., Moccia, F., Grings, F., Salvia, M., Douna, M. B., V., Karszenbaum, H., Soldano, A., Goniadzki, D., Parmuchi, G., Montenegro, C., Kandus, P. and Borro, M. 2010, The Effect of Rain and Flooding Events on AMSR-E Signatures of La Plata Basin, Argentina: IEEE Journal iof Selected Topics in Applied Eart6h Observation and Remote Sens., v. 3, p. 81-90.

Ferrazzoli, P., Rahmoune, R., Singh,Y., Kerr, Y., Richaume, P., Al Bitar, A., Magagi, R. and Moisy, C. , 2013, Estimate of forest parameters and comparisons with independent measurements: SMOS-workshop.

Fily, M., Royer, A., Goita, K. and Prigent., C., 2003, A Simple Retrieval Method for Land Surface Temperature and Fraction of Water Surface Determination from Satellite Microwave Brightness Temperature in Sub-Arctic Area: Remote Sens. Environ, v. 85, p. 328-338.

Fisch, U., Hasslacher, B. and Pomeau, Y., 1986, Lattice-Gas Automata for the Navier Stokes equation: Physical Review Letters, v. 56, p. 1505-1508.

Freeman, A., Chapman, B. and Siqueira, P., 2002, The JERS-1 Amazon Multi-season Mapping Study (JAMMS): Science objectives and implications for future missions: International Journal of

Remote Sensing, v. 23, p. 1447-1460.

Fung, A. K., 1994, Microwave Scattering and Emission. Models and their applications, Artech House.

Galantowicz, J. F., Entekhabi, D..and Njoku, I. G., 2000, Estimation of soil-type heterogeneity effects in the retrieval of soil moisture from radio brightness: IEEE Trans. on Geosci. and Remote Sens., v. 38, p. 312-316.

Gillespie, T. W., Chu, J., Frankenberg, E. and Thomas, D. , 2007, Assessment and prediction of natural hazards from satellite imagery: Progress in Physical Geography v. 31, p. 459-470.

Gloersen, P. and Barath, F. T., 1977, Scanning multichannel microwave radiometer for Nimbus-G and Seasat-A: IEEE Journal of Ocean Engineering, v. OE(2), p. 172-178.

Goita, K. and Royer, A., 2002, Combination of Passive Microwave and Thermal Infrared for the Retrieval and Analysis of Microwave Emissivities and Temperature: IGRSS (IEEE).

Govt. Of India, 2012, Official Website of Dhemaji District.

Grant, J. P., Saleh, K., Wigneron, J.P., Guglielmetti, M., Kerr, Y.H., Schwank, M., Skou, N. and Van de Griend, A. A., 2008, Calibration of the L-MEB Model Over a Coniferous and a Deciduous Forest: IEEE Trans. on Geosci. and Remote Sens., v. 46, p. 808-818.

Grant, J. P., Van de Griend, A. A., Schwank, M. and Wigneron, J.P., 2009, Observations and modeling of a pine forest floor at L-band: IEEE Trans. on Geosci. and Remote Sens., v. 47.

Grant, J. P., Van de Griend, A. A., Wigneron, J.-P., Saleh, K., Panciera, K. and Walker J. P., 2010, On the Influence of Forest Cover Fraction on L-band Soil Moisture Retrievals from Heterogeneous Pixels using Multi-Angular Observations: Remote Sens. Environ, v. 114, p. 1026-1037.

Grant, J. P., Wigneron, J.-P., Van de Griend, A.A., Kruszewski, A., Schmidl Sbjrg, S. and Skou,, 2007, A field experiment on microwave forest radiometry: L-band signal behaviour for varying conditions of surface wetness: Remote Sens. Environ, v. 109, p. 10-19.

Griddings, L. and Choudhury, B. J., 1989, Observation of Hydrological Features with Nimbus-7 37 Ghz Data, Applied to South America: International Journal of Remote Sensing, v. 10, p. 1673-1686.

Grings, F., Ferrazzoli, P., Karszenbaum, H., Tiffenberg, J., Kandus, P., Guerriero, L. and Jacobo-Berrles, J., 2005, Modeling temporal evolution of junco marshes radar signatures: IEEE Trans. on Geosci. and Remote Sens., v. 43, p. 2238-2245.

Grody, N. C., 1991, Classification of Snow Cover and Precipitation Using the Special Sensor Microwave/Imager (SSM/I): journal of Geophysical Research, v. 96, p. 7423-7435.

Guglielmetti, M., Schwank, M., Mätzler, C., Oberdörster, C., Vanderborght, J. and Flühler, H., 2007, Measured microwave radiative transfer properties of a deciduous forest canopy: Remote Sens. Environ, v. 109, p. 523-532.

Guglielmetti, M., Schwank, M., Mtzler, C., Oberdrster, C., Vanderborght, J. and Flhler, H., 2008, FOSMEX: Forest Soil Moisture Experiments with Microwave Radiometry: IEEE Trans. on Geosci. and Remote Sens., v. 46, p. 727-735.

Hallikainen, M. T., Jolma, P. A. and Hyyppa, J. M., 1988, Satellite microwave radiometry of forest and surface types in Finland: IEEE Trans. on Geosci. and Remote Sens., v. 26, p. 622-628.

Hallikainen, M. T., Ulaby, F.T., Dobson, M.C., El-Rayes, M.A. and L-Wu., 1985, Microwave Dielectric Behavior of Wet Soil-Part 1: Empirical Models and Experimental Observations: IEEE Trans. on Geosci. and Remote Sens., v. 23, p. 25-34.

Hamilton, S. K., Sippel, S. J. and Melack, J. M., 2002, Comparison of inundation patterns among major South American floodplains: Journal of Geophysical Research, v. 107 D20, p. 8038.

Helvey, J. D. and Patric, J. H. 1965, Canopy and litter interception of rainfall by hardwoods of eastern United States: Water Resource Research, v. 1(2), p. 193-206.

Hipp, J. E., 1974, Soil electromagnetic parameters as functions of frequency, soil density, and soil moisture: Proceesings of IEEE, v. 62, p. 98-103.

Hollinger, J. P., Pierce, J. L. and Poe, G. A., 1990, SSM/I instrument evaluation: IEEE Trans. on Geosci. and Remote Sens., v. 28, p. 781-790.

Holmes, T., de Rosnay, P., de Jeu, R., Wigneron, J.-P., Kerr, Y., Calvet, J.-C., Escorihuela, M. J., Saleh, K. and Lematre, F., 2006, A new parameterization of the effective temperature for L- band radiometry: Geophysical Research Letters, v. 33, p. 7405.

Howard, D. and Howard, P. 1993, Relationships between CO2 evolution, moisture content and temperature for a range of soil types: Soil Biology Biochemistry, v. 25, p. 1537-1546.

Idso, S. B., Jackson, R.D. and Reginato, R.J., 1975, Detection of soil moisture by remote surveillance: American Science, v. 63, p. 549-557.

Imaoka, K., Kachi, M., Kasahara, M., Itoa, N., Nakagawa, N. and Oki. T., 2010, Instrument Performance and Calibration of AMSR-E and AMSR2: International Archives of the Photogrammetry, Remote Sensing and Spatial Information Science.

Imaoka, K., Sezai, T., Takeshima, T., Kawanishi, T. and Shibata, A. 2002, Instrument characteristics and calibration of AMSR and AMSR-E: Proc. IGARSS, p. 18-20.

Ip, F., Dohm, J.M., Baker, V.R., Doggett, T., Davies, A.G., Castano, R., Chien, S., Cichy, B., Greeley, R., Sherwood, R., Tran, D. and Rabideau, G. , 2006, Flood detection and monitoring with the autonomous sciencecraft experiment onboard EO-1: Remote Sens. Environ, v. 101, p. 463-481.

Jackson, T. J. and Schmugge, T. J. , 1991, Vegetation effects on the microwave emission from soils: Remote Sens. Environ, v. 36.

Jackson, T. J., Cosh, M. H., Bindlish, R., Starks, P. J., Bosch, D. D., Seyfried, M., Goodrich, D. C., Moran, M. S. and Du, J., 2010, Validation of Advanced Microwave Scanning Radiometer soil moisture products: IEEE Trans. on Geosci. and Remote Sens., v. 48, p. 4256-4272.

Jackson, T. J., Le Vine, D. M., Hsu, A. Y., Oldak, A., Starks, P. J., Sift, C. T., Isham, J. D. and Haken, M., 1999, Soil moisture mapping at Regional Scales using microwave radiometry: The Southern Great Plains hydrology experiment: IEEE Trans. on Geosci. and Remote Sens., v. 37, p. 2136-2151.

Jackson, T. J., Levine, D.M., Griffis, A.J., Goodrich, D.C., Schmugge, T.J., Swift, C.T. and O.Neill, P.E., 1993, Soil moisture and rainfall estimation over a semi-arid environment with the ESTAR microwave radiometer: IEEE Trans. on Geosci. and Remote Sens., v. 31, p. 836-841.

Jacobs, J. M., Myers, D. A. and Whitfield, B. M. , 2003, Improved rainfall/runoff estimates using remotely sensed soil moisture: J. Amer. Water Resour. Assoc., v. 39, p. 313-324.

Jenny, H., 1994, Factors of Soil Formation. A System of Quantitative Pedology: New York, Mcgraw-hill

Jin, K.-W., Njoku, E. G. and Chan, S. 2006, Impact of Rainfall on the Retrieval of Soil Moisture using AMSR-E Data: IGARSS.

Karam, M. A., 1997, A physical model for microwave radiometry of vegetation: IEEE Trans. on Geosci. and Remote Sens., v. 35, p. 1045-1058.

Kawanishi, T., Sezai, T., Ito, Y., Imaoka, K., Takeshima, T., Ishido, Y., Shibata, A., Miura, M., Inahata, H. and Spencer, R., 2003, "The advanced microwave scanning radiometer for the earth observing system (AMSR-E) NASDA's contribution to the EOS for global energy and water cycles studies,: IEEE Trans. on Geosci. and Remote Sens., v. 41, p. 184-194.

Kerr, Y. H., Waldteufel, P., Richaume, P., Wigneron, J. P., Ferrazzoli, P., Mahmoodi, A., Al Bitar, A., Cabot, F., Gruhier, C., Juglea, S. E., Leroux, D., Mialon, A. and Delwart, S., 2012, The SMOS Soil Moisture Retrieval Algorithm: IEEE Trans. on Geosci. and Remote Sens., v. 50, p. 1367-1383.

Kerr, Y. H., Waldteufel, P., Richaume, P., Davenport, I., Ferrazzoli, P. and Wigneron, J.-P., 2010, SMOS level 2 processor for soil moisture, algorithm theoretical based document (ATBD), CESBIO, IPSL-Service d'Aéronomie, INRA-EPHYSE, Reading University, Tor Vergata University. SO-TN-ESL-SM-GS-0001.

Kerr, Y. K. and Njoku, E. G. , 1990, A semiempirical model for interpreting microwave emission from semiarid land surfaces as seen from space: IEEE Trans. on Geosci. and Remote Sens., v. 28, p. 384-393.

Kirdiashev, K. P., Chukhlantsev, A.A. and Shutko, A.M., 1979, Microwave radiation of the Earth's surface in the presence of vegetation cover: Radio Eng. Eletron Physics, v. 2, p. 37-56.

Kruopis, N., Praks, J., Arslan, A. N., Alasalmi, H. M., Koskinen, J. T. and Hallikainen, M. T., 1999, Passive microwave measurements of snow-covered forest areas in EMAC'95: IEEE Trans. on Geosci. and Remote Sens., v. 37, p. 2699-2705.

Kummerow, C., Barnes, W., Kozu, T., Shiue, J. and Simpson, J., 2001, The Tropical Rainfall Measuring Mission (TRMM) sensor package: Journal of Atmospheric Oceanic Technology, v. 15.

Kurum, M., Lang, R., O'Neill, P., Joseph, A., Jackson, T. and Cosh, M., 2011, A First-Order Radiative Transfer Model for Microwave Radiometry of Forest Canopies at L-band: IEEE Trans. on Geosci. and Remote Sens., v. 49, p. 3167-3179.

Kurum, M., O'Neill, P., Lang, R., Cosh, M., Joseph, A. and Jackson, T., 2012, Impact of Conifer Forest Litter on Microwave Emission at L-Band: IEEE Trans. on Geosci. and Remote Sens., v. 47, p. 2024-2034.

Lang, R. H., Utku, C., de Matthaeis, P., Chauhan, N. and LeVine, D. M., 2001, ESTAR and model brightness temperatures over forests: Effects of soil moisture: IGRSS, p. 1300-1302.

Lang, R. H., de Matthaeis, P., LeVine, D. M., Bidwell, S., Haken, M. and Chauhan, N., 2000, L-band radiometer measurements of coniferous forests: IGRSS, p. 1930-1932.

Le Toan, T., Laur, H., Mougin, E. and Lopes, A., 1989, Multitemporal and dual-polarization observationsof agricultural vegetation covers by X-band SAR images: IEEE Trans. on Geosci. and Remote Sens., v. 27, p. 709-718.

Ledieu, J., DeRidder, P., DeClerck, P. and Dautreband, S. , 1986, A method of measuring soil moisture by time-domain reflectometry: Journal of Hydrology, v. 88, p. 319-328.

LeVine, D. M. and Good, J.C. , 1983, Aperture synthesis for microwave radiometry in space, NASA Technical Memorandum.

LeVine, D. M. and Abraham, S., 2002, The effect of the ionosphere on remote sensing of the sea surface salinity from space: absorption and emission at L-band: IEEE Transactions on Geoscience and Remote Sensing, v. 40, p. 771-782.

Lewis, A. J., Henderson, F.M. and Holcomb, D.W. , 1998, Radar fundamentals: the geosciences perspective. : Principles and applications of imaging radar: New York, , Wiley.

Lymburner, L., Mueller, N. and Islam, A. , 2008, Assessing the accuracy of fl ood mapping techniques using coincident MODIS and Landsat TM scenes: 14th Australasian Remote Sensing and Photogrammetry Conference.

MÄatlzler, C. and Standley, A. , 2000, Relief effects for passive microwave remote sensing: journal of Geophysical Research, v. 21, p. 2403-2412.

Macelloni, G., Paloscia, S., Pampaloni, P. and Ruisi, R., 2001, Airborne multifrequency L- to Ka-band radiometric measurements over forests: IEEE Trans. on Geosci. and Remote Sens., v. 39, p. 2507-2513.

Mart´ın-Neira, M., Rib´o, S. and Mart´ın-Polegre, A. J., 2002, Polarimetric mode of MIRAS: IEEE Transactions on Geoscience and Remote Sensing, v. 40, p. 1755-1768.

Masson, V., Champeau, J.-L.,Chauvin, F., Meriguet, C. and Lacaze R., 2003a, A global data base of land surface parameters at 1 km resolution in meteorological and climate models: Journal of Climate, v. 16, p. 1261-1282.

Masson, V., Champeau, J.-L., Chauvin, F., Meriguet, C. and Lacaze, R., 2003b, A global data base of land surface parameters at 1 km resolution in meteorological and climate models: Journal of Climate, v. 16, p. 1261-1282.

Matzler, C., 1994a, Microwave transmissivity of a forest canopy: Experiments made with a beech: Remote Sens. Environ, v. 48, p. 172-180.

Matzler, C., 1994b, Passive Microwave Signatures of Landscape in Winter: Materological Atmospheric Physics, v. 54, p. 241-260.

McMullan, K. D., Brown, M., Martin-Neira, M., Rits, W., Ekhlom, S., Marti, J. and Lemanczyk, J., 2008, SMOS: The payload: IEEE Trans. on Geosci. and Remote Sens., v. 46, p. 594-605.

Meirold-Mautner, I., Mugerin, C., Vergely, J.-L.,Spurgeon, P., Rouffi, F. and Meskini, N., 2009, SMOS ocean salinity performance and TB bias correction: EGU.

Mialon, A., Royer, A. and Fily, M., 2005, Wetland seasonal dynamics and interannual variability over northern high latitudes, derived from microwave satellite data: Journal of Geophysical Research, v. 110.

Mialon, A., Coret, L., Kerr, Y. H., Sécherre, F. and Wigneron, J.-P., 2008, Flagging the topographic impact on the SMOS signal: IEEE Geosciences Remote Sensing, v. 46, p. 689-694.

Miller, D. H., 1977, Water at the Surface of the Earth: An Introduction to Ecosystem Hydrodynamics, v. 2 ed.: NY, USA, Academic Press.

Mironov, V. L., Dobson, M.C., Kaupp, V.H., Komarov, S.A. and Kleshchenko, V.N. , 2004, Generalized refractive mixing dielectric model for moist soils: IEEE Trans. on Geosci. and Remote Sens., v. 42, p. 773-785.

Mironov, V. L., Komarov, S. A. and Kleshchenko, V. N., 1997, Effect of bound water on the dielectric properties of wet frozen soils: Earth Observation Remote Sensing, v. 13, p. 347-356.

Mironov, V. L., Komarov, S. A., Rychkova, N. V. and Kleshchenko, V. N., 1995, Study of the dielectric properties of wet grounds at microwave frequencies: Earth Observation Remote Sensing, v. 12, p. 495-504.

Mo, T. and Schmugge, T.J. , 1987, A parameterization ot the effect of surface roughness on microwave emission: IEEE Trans. on Geosci. and Remote Sens., v. 25, p. 47-54.

Moran, M. S., Peters-Lidard, C. D. and McElroy, S. A., 2004, Estimating soil moisture at the watershed scale with satellite-based radar and land surface models: Canadian journal of Remote Sensing, v. 30, p. 805-826.

Nakahara, K., Itoh, Y., Horiie, Y., Sakura, T., Yoshida, N., Katoh, T., Takagi, T. and Mitsui, Y., 1995, Millimeter-wave monolithic AlGaAs/In-GaAs/GaAs pseudomorphic HEMT low noise amplifier modules for advanced microwave scanning radiometer: IEICE Trans. Electron, v. E78-C, p. 1210-1215.

Nakajima, M., Ito, Y., Maejima, H. and Kojima, Y., 1994, The development of AMSR and GLI for ADEOS-II: 45th Congress of the International Astronautical Federation.

NASA and Jet Propulsion Laboratory, 2012, NASA Map Sees Earth's Trees in New Light.

Njoku, E. G. and Chan, T.K., 2006, Vegetation and surface roughness effects on AMSR-E land observations: Remote Sens. Environ, v. 100, p. 190-199.

Njoku, E. G. and Entekhabi, D., 1996, Passive microwave remote sensing of soil moisture: Journal of Hydrology, v. 184, p. 101-129.

Njoku, E. G. and Kong, J. A., 1977, Theory for passive microwave remote sensing of near-surface soil

moisture: Journal of Geophysical Research Solid Earth and Planets, v. 82, p. 3108-3118.

Njoku, E. G., Ashcroft, P., Chan, T. K. and Li. L., 2005, Global Survey and Statistics of Radio-Frequency Interference in AMSR-E Land Observations: IEEE Trans. on Geosci. and Remote Sens., v. 43, p. 938-947.

Njoku, E. G., Jackson, T., Lakshmi, V., Chan, T. and Nghiem, S. V., 2003, Soil moisture retrieval from AMSR-E: IEEE Trans. on Geosci. and Remote Sens., v. 41, p. 215-229.

Noboroi, K., 2001, Measurement of soil water content and electrical conductivity by time domain reflectometry: a review: Computer and Electronics in Agriculture, v. 31, p. 213-237.

Or, D. and Wraith, J. M. 1999, Temperature effects on soil bulk dielectric permittivity measured by time domain reflectometry: A physical model: Water Resource Research, v. 35, p. 371-383.

Overton, I. C., McEwan, K., Gabrovsek, C. and Sherrah, J.R. , 2006, The River Murray Floodplain Inundation Model – Hume Dam to Lower Lakes, CSIRO Water for a Healthy Country Technical Report, CSIRO, Canberra.

Owe, M., Van De Griend, A. A.,.De Jeu, R., De Vries, J. J., Seyhan, E. and Engman, E. T., 1999, Estimating Soil Moisture from Satellite Microwave Observations: Past and Ongoing Projects, and Relevance to GCIP: Journal of Geophysical Research, v. 104, p. 19735-19742.

Owe M., Ram, D. J. and Holmes, T. R. H., 2008, Multi-Sensor Historical Climatology of Satellite-Derived Global Land Surface Moisture: Journal of Geophysical Research, v. 113.

P.531-6, I.-R., 2001, Ionospheric propagation data and prediction methods required for the design of satellite services and systems, Tech. rep., ITU. (document), 2.1.5.

Paloscia, S. and Pampaloni, P., 1988, Microwave polarization index for monitoring vegetation growth: IEEE Trans. on Geosci. and Remote Sens., v. 26, p. 617-621.

Paloscia, S., Macelloni, G. and Santi, E., 2006, Soil moisture estimates from AMSR-E brightness temperatures by using a dual-frequency algorithm: IEEE Trans. on Geosci. and Remote Sens., v. 44, p. 3135-3144.

Paloscia, S., Pampaloni, P., Chiarantini, L., Coppo, P., Gagliani, S. and Luzi, G., 1993, Multifrequency passive microwave remote sensing of soil misture and roughness: International Journal of Remote Sensing, v. 14, p. 467-483.

Pampaloni, P., 2004, Microwave radiometry of forests: Wave Random Media, v. 14, p. S275-S298.

Parde, M., Wigneron, J.-P., Waldteufel, P., Kerr, Y.H., Chanzy, A., Sobjaerg, S.S. and Skou, N., 2004, N-parameter retrievals from L-band microwave observations acquired over a variety of crop fields: IEEE Trans. on Geosci. and Remote Sens., v. 42, p. 1168-1178.

Pauwels, R. N., Hoeben, R., Verhoest, N. E. C., De Troch, F. R. and Troch, P. A. , 2002, Improvement of TOPLATS-based discharge predictions through assimilation of ERS-based remotely sensed soil moisture values: Hydrological Processes, v. 16, p. 995-1014.

Peplinsky, N. R., Ulaby, F.T. and Dobson, M.C, 1995, Dielectric properties of soils in the 0.3-1.3 GHz

range. : IEEE Trans. on Geosci. and Remote Sens., v. 33, p. 803-807 (correction: IEEE Trans. on Geosci. and Remote Sens. 1995 33:1349).

Prigent, C., Aires, F., Rossow, W. B. and Robock, A., 2005, Sensitivity of satellite microwave and infrared observations to soil moisture at a global scale: Relationship of satellite observations to in situ soil moisture measurements: Journal of Geophysical Research, v. 110, D07110.

Prigent, C., Aires, F.,. Rossow, W. B. and Matthews, E., 2001, Joint Characterization of Vegetation by Satellite Observations from Visible to Microwave Wavelength: A Sensitivity Analysis: Journal of Geophysical Research, v. 106, p. 20665-20685.

Prigent, C., Rossow, W. B. and Matthews, E., 1997, Microwave Land Surface Emissivities Estimated from SSM/I Observations: Journal of Geophysical Research, v. 102, p. 21867-21890.

Rahmoune, R., Ferrazzoli, P., Kerr, Y. and Richaume, P., 2013, SMOS L2 algorithm over forests: Description and generation of global maps: IEEE Journal of Selected Topics in Applied Eart6h Observation and Remote Sens (in press).

Rahmoune, R., Ferrazzoli, P., Walker, J. P. and Grant, J. P, 2010, L-band emission from a Eucalyptus forest in various soil conditions during the NAFE campaign: MICRORAD.

Rahmoune, R., Singh, Y., Ferrazzoli, P., Kerr, Y., Richaume, P., Al Bitar, A. and Moisy, C., 2013a, SMOS L2 Retrival Results over the American continents and comparison with independent data sources: IGARSS.

Randa, J., 2008, Recommended terminology for microwave radiometry, Tech. rep., National Institution of Standards and Tecnology.

Robinson, D. A., Campbell, C. S., Hopmans, J. W., Hornbuckle, B. K., Jones, S. B., Knight, R., Ogden, F., Selker, J. and Wendroth, O., 2008, Soil moisture measurement for ecological and hydrological watershed-scale observatories : A review: Vadose Zome Journal, v. 7, p. 358-389.

Robock, A., 2000, The Global Soil Moisture Data Bank: Bull Atmospheric Meterological Society, v. 81, p. 1281-1299.

Rodell, M., Houser, P. R., Jambor. U., Gottschalck, J., Mitchell, K., Meng, C.J., Arsenault, K., Cosgrove, B., Radakovich, J., Bosilovich, M., Entin, J. K., Walker, J. P., Lohmann, D. and Toll, D., 2004, The global Land Data Assimilation System: Bulleten American Meterological Society, v. 85(3), p. 381-394.

Rodriguez-Iturbe, I., 2000, Ecohydrology : A hydrologic perspective of climate-soil-vegetation dynamics: Water Resource Research, v. 36, p. 3-9.

Roth, C. H., Malicki, M.A. and Plagge, R. , 1992, Empirical evaluation of the relationship between soil dielectric constant and volumetric water content as the basis for calibrating soil moisture measurements by TDR: Journal of Soil Science, v. 43, p. 1-3.

Running, S. W., 1994, Testing FOREST-BGC ecosystem process simulations across a climatic gradient in Oregon: Ecological Applications, v. 4, p. 238-247.

Sabburg, J., Ball, J. A. R. and Hancock, N. H., 1997, Dielectric behavior of moist swelling clay soils at

microwave frequencies: IEEE Trans. on Geosci. and Remote Sens., v. 35, p. 784-787.

Sahoo, A. K., Houser, P. R., Ferguson, C., Wood, E. F., Dirmeyer, P. A. and Kafatos, M., 2008, Evaluation of AMSR-E soil moisture results using the insitu data over the Little River Experimental Watershed, Georgia: Remote Sens. Environ, v. 112, p. 3142-3152.

Sakamoto, T., Nguyen, N.V., Kotera, A., Ohno, H., Ishitsuka, N. and Yokozawa, M. , 2007, Detecting temporal changes in the extent of annual flooding within the Cambodia and the Vietnamese Mekong Delta from MODIS time-series imagery: Remote Sensing of Environment, v. 109, p. 295-313.

Saleh, K., Wigneron, J.-P., de Rosnay, P., Calvet, J.-C., Escorihuela, M. J., Kerr, Y. and Waldteufel, P., 2005, Impact of rain interception by vegetation and litter on the L-band emission of natural grasslands (SMOSREX Experiment): Journal of Geophysical Research.

Saleh, K., Wigneron, J.-P., de Rosnay, P., Calvet, J.-C., Escorihuela, M.J., Kerr, Y. and Waldteufel, P., 2006a, Impact of rain interception by vegetation and mulch on the L-band emission of natural grass: Remote Sens. Environ, v. 101, p. 127-139.

Saleh, K., Wigneron, J. P., Calvet, J. C., Lopez-Baeza, E., Ferrazzoli, P., Berger, M., Wursteisen, P., Simmonds, L. and Miller, J., 2004, The EuroSTARRS airborne campaign in support of the SMOS mission: first results over land surfaces: International Journal of Remote Sensing, v. 25, p. 177-194.

Salvia, M., Grings, F., Ferrazzoli, P., Barraza, V., Douna, V., Perna, P. and Karszenbaum, H., 2011, Estimating flooded area and mean water level using active and passive microwaves: the example of Paran´a River Delta floodplain: Hydrological Earth System Science Discussion, v. 8, p. 2895-2928.

Sandholt, I., Nyborg, L., Fog, B., Lo, M., Bocoum, O. and Rasmussen, K, 2003, Remote sensing techniques for flood monitoring in the Senegal River Valley: Danish Journal of Geography, v. 103, p. 71-81.

Santi, E., Paloscia, S., Pampaloni, P. and Pettinato, S., 2009, Ground-based microwave investigations of forest plots in Italy: IEEE Trans. on Geosci. and Remote Sens., v. 47, p. 3016-3025.

Schaefer, G. L., Cosh, M. H. and Jackson, T. J., 2007, USDA natural resources conservation service Soil Climate Analysis Network (SCAN): Journal Atmos. Ocean Technology, v. 24, p. 2073-2077.

Schar, C., Luthi, D., Beyerle, U. and Heise, E., 1999, The soil-precipitation feedback: A process study with a regional climate model: Journal of Climate, v. 12, p. 722-741.

Schmugge, T., Jackson, T. J., Kustas, W. P., Roberts, R., Parry, R., Goodrich, D. C., Amer, S. A. and Weltz, M. A.,1994, Push broom microwave radiometer observations of surface soil moisture in Monsoon '90: Water Resource Research, v. 30, p. 1321-1327.

Schmugge, T. J., Menennly, J.M., Rango, A. and Neff, R., 1977, Satellite microwave observations of soil moisture variations: Water Resource Bull., v. 13, p. 265-281.

Schneeberger, K., Schwank, M., Stamm, Ch., de Rosnay, P., MÄatzler, C. and FlÄuhler, H. , 2004, Topsoil Structure Influencing Soil Water Retrieval by Microwave Radiometry: Vadose Zome

Journal, v. 3, p. 1169-1179.

Schwank, M., StÄahli, M., Wydler, H., Leuenberger, J., MÄatzler, C. and FlÄuhler, H. , 2004, Microwave L-band emission of freezing soil: IEEE Trans. on Geosci. and Remote Sens., v. 42, p. 1252-1261.

Scofield, R., LaDue, J. G., Scofield, R., Grody, N. and Ferraro, R., 1994, A soil wetness index for monitoring the great flood of 1993: 7th Conf. Satellite Meteorol. Oceanography, p. 580-583.

Seneviratne, S. I., Luthi, D., Litschi, M. and Schar, C., 2006, Land-atmosphere coupling and climate change in Europe: Nature, v. 443(7108), p. 205-209.

Shi, J., Chen, K.S., Qin, L., Jackson, T.J., O'Neill, P.E. and Leung, T. , 2002, A parameterized surface reflectivity model and estimation of bare-surface soil moisture with L-band radiometer: IEEE Trans. on Geosci. and Remote Sens., v. 40, p. 2674-2686.

Shibata, A., Imaoka, K. and Koike, T., 2003, AMSR/AMSR-E level 2 and 3 algorithm developments and data validation plans of NASDA: IEEE Trans. on Geosci. and Remote Sens., v. 41, p. 195-203.

Shibata, K. I., Kachi, M. and Murakami, H., 1999, SST observation by TRMM microwave imager aboard tropical rainfall measuring mission: Umi no Kenkyu, v. 8, p. 135-139.

Shutko, A. M. and Reutov, E.M. , 1982a, Mixture formulae applied in estimation of dielectric and radiative characteristics of soils and grounds at microwave frequencies: IEEE Trans. on Geosci. and Remote Sens., v. GE-20, p. 29-32.

Shutko, A. M. and Chukhlantsev, A. A., 1982b, Microwave radiation peculiarities of vegetative covers: IEEE Trans. on Geosci. and Remote Sens., v. GRS-20, p. 27-29.

Simard, M., Pinto, N., Fisher, J. B. and Baccini, A., 2011, Mapping forest canopy height globally with spaceborne lidar", Journal of Biophysical Research: Biophysical Research v. 116.

Singh, Y., Dutta U. and Prabhu I., 2008, Multi-variate Segmentation Approach for Flood Monitoring using Microwave Data: PORSEC 2008.

Singh, Y., Ferrazzoli, P. and Rahmoune, R., 2012, Testing flood monitoring methods using AMSR-E in Indian sites: MICRORAD.

Singh, Y., Ferrazzoli, P and Rahmoune, R., 2012(a), Flood monotoring using Passive Remote Sensing (AMSR-E) over a part of Brahmaputra Basin, India: IGARSS.

Singh, Y., Ferrazzoli, P. and Rahmoune, R., 2013, Flood monitoring using microwave passive remote sensing (AMSR-E) in part of the Brahmaputra basin, India: International Journal of Remote Sensing, v. 34, p. 4967-4985.

Sippel, S. J., Hamilton, S. K., Melack, J. M., and Novo, E. M. M., 1998, Passive microwave observations of inundation area and the area/stage relation in the Amazon River floodplain: International Journal of Remote Sensing, v. 19, p. 3055-3074.

Sippel, S. K., Hamilton, S. K., Melack, J. M. and Choudhury, B. J., 1994, Determination of inundation area in the Amazon River floodplain using the SMMR 37 GHz polarization difference: Remote

Sens. Environ, v. 48, p. 70-76.

Skou, N., 1989, Microwave radiometer systems: Design and analysis, Artech House.

Smith, L. C., 1997, Satellite remote sensing of river inundation area, stage, and discharge, A review: Hydrological Processes, v. 11, p. 1427-1439.

Solimini, D., 2013, Understanding Earth Observation, v. Draft Ver. 2.1: Rome, Italy.

Talone, M., Camps, A., Monerris, A., Vall-llossera, M., Ferrazzoli, P. and Piles, M., 2007, Surface topography and mixed pixel effects on the simulated L-band brightness temperatures: IEEE Trans. on Geosci. and Remote Sens., v. 42, p. 786-794.

Tanaka, M., Sugimura, T., Tanaka, S. and Tamai, N. , 2003, Flood-drought cycle of Tonle Sap and Mekong Delta area observed by DMSP-SSM/I: International Journal of Remote Sensing, v. 24(7), p. 1487-1504.

Thankappan, M., Reddy, S., Ackerly, S. and Forghani, A., 2008, Sentinel floods prototype: a system for rapid dissemination of satellite derived information on flooding: 14th Australasian Remote Sensing and Photogrammetry Conference.

Ticehurst, C. J., Dyce, P. and Guerschman, J.P., 2009, Using passive microwave and optical remote sensing to monitor flood inundation in support of hydrologic modelling 18th World IMACS / MODSIM Congress, Crains, Australia.

Topp, G. C., Davies, J.L. and Annan, A.P. , 1980, Electromagnetic determination of soil water content: Measurements in coaxial transmission lines: Water Resource Research, v. 16, p. 574-582.

Ulaby, F., Moore, R. and Fung, A., 1981, Microwave remote sensing active and passive, v. 1 & 2, Artech House.

Ulaby, F., Moore, R. and Fung, A. K., 1982, Microwave Remote Sensing: Active and Passive v. volume II: Radar remote sensing and surface scattering and emission theory, Addison-Wesley Publishing Company.

Ulaby, F. T., Sarabandi, K., McDonald, K., Whitt, M. and Dobson, M. C., 1990, Michigan microwave canopy scattering model: International Journal of Remote Sensing, v. 11, p. 1223-1253.

Ulaby, F. T., Moore, R. K. and Fung, A. K. , 1986a.

Ulaby, F. T., Moore, R. K. and Fung, A. K. , 1986b, Microwave Remote Sensing: Active and Passive. Vol. II, Radar remote sensing and surface scattering and emission theory: Reading,Massachusetts, Addison-Wesley.

Van de Griend, A. A. and Wigneron, J. P, 2004, The b-factor as a function of frequency and canopy type at H-polarization: IEEE Trans. on Geosci. and Remote Sens., v. 42, p. 786-794.

Van de Griend, A. A., Wigneron, J. P. and Waldteufel, P., 2003, Consequences of Surface Heterogeneity for Parameter Retrieval from 1.4 GHz Multiangle SMOS Observations: IEEE Trans. on Geosci. and Remote Sens., v. 41, p. 803-811.

Verstraeten, W. W., Veroustraete, F., van der Sande, C. J., Grootaers, I. and Feyen, J., 2006, Soil moisture

retrieval using thermal inertia, determined with visible and thermal spaceborne data, validated for European forests: Remote Sens. Environ, v. 101, p. 299-314.

Vinnikov, K. Y., Robock, A., Qiu, A. S., Entin, J. K., Owe, M., Choudhury, B. J., Hollinger, S. E. and Njoku., E. G., 1999, Satellite Remote Sensing of Soil Moisture in Illinois, United States: journal of Geophysical Research, v. 104, p. 4145-4168.

Viterbo, P. and Betts, A. K., 1999, Impact of the ECMWF reanalysis soil water on forecasts of the July 1993 Mississippi flood: Journal of Geophysics Research, v. 104, p. 19361-19366.

Wagner, W., Scipal, K., Pathe, C., Gerten, D., Lucht, W. and Rudolf, B., 2003, Evaluation of the agreement between the first global remotely sensed soil moisture data with model and precipitation data: Journal of Geophysical Research, v. 108(D19), p. 4611.

Wang, J. R., 1983, Passive microwave sensng of soil moisture content: The effects of soil bulk density and surface roughness: Remote Sens. Environ, v. 13, p. 329-344.

Wang, J. R. and Choudhury, B.J. , 1981, Remote sensing of soil moisture content over bare field at 1.4 GHz frequency: Journal of Geophysical Research, v. 86, p. 5277-5282.

Wang, J. R. and Schmugge, T. J. , 1980, An empirical model for the complex dielectric permittivity of soils as a function of water content: IEEE Trans. on Geosci. and Remote Sens., v. 18, p. 288-295.

Wang, Y., Hess, L., Filoso, S. and Melack, J., 1995, Understanding the radar backscattering from flooded and nonflooded Amazonian Forests: results from canopy backscatter modeling: Remote Sens. Environ, v. 54, p. 324-332.

WegmÄuller, U. and MÄatzler, C. , 1999, Rough bare soil reflectivity model: IEEE Trans. on Geosci. and Remote Sens., v. 37, p. 1391-1395.

Wigneron, J.-P., Chanzy, A., Calvet, J.-C. Olioso, A. and Kerr, Y., 2002, Modeling approaches to assimilating LBand passive microwave observations over land surfaces: Journal of Geophysical Research, v. 107.

Wigneron, J.-P., Chanzy, A., de Rosnay, P., RÄudiger, C. and Calvet, J.-C., 2008, Estimating the effective soil temperature at L-band as a function of soil properties: IEEE Trans. on Geosci. and Remote Sens., v. 46, p. 797-807.

Wigneron, J.-P., Guyon, D., Calvet, J.-C., Courrier, G. and Bruguier, N., 1997, Monitoring coniferous forest characteristics using a multifrequency (5–90 GHz) microwave radiometer: Remote Sens. Environ, v. 60, p. 299-310.

Wigneron, J.-P., Laguerre, L. and Kerr, Y.H. , 2001, A simple parameterization of the L-band microwave emission from rough agricultural soils: IEEE Trans. on Geosci. and Remote Sens., v. 39, p. 1697-1707.

Yueh, S., 2000, Estimates of Faraday rotation with passive microwave polarimetry for microwave remote sensing of Earth surfaces: IEEE Transactions on Geoscience and remote Sensing, v. 38, p. 2434–2438. .

Yueh, S., Wilson, W., Li, F., Nghiem, S. and Ricketts, W., 1995, Polarimetric measurements of sea

surface brightness temperatures using an aircraft K-band radiometer: IEEE Transactions on Geoscience and Remote Sensing, v. 33, p. 86-92.

Appendix A

Radiative Transfer Equation (RTE)

The specific intensity of radiation is the energy flux per unit time, unit frequency, unit solid angle and unit area normal to the direction of propagation.

The radiative transfer equation states that the specific intensity of radiation I_σ during its propagation in a medium is subject to losses due to extinction and to gains due to emission:

$$\frac{dI_\sigma}{d_x} = -\mu_\sigma . I_\sigma + \rho . j_\sigma \tag{A.1}$$

Where, x is the co-ordinate along the optical path, μ_σ is the extinction coefficient, ρ is the mass density j_σ is the emission coefficient per unit mass. First to understand the simple case of the radiative transfer equation where there is no scattering effect, local thermodynamic equilibrium and the medium is homogeneous. In general, the extinction coefficient μ_σ includes both the absorption coefficient α_σ and the scattering coefficient s_σ , of both the gas and the aerosols present in the gas:

$$\mu_\sigma = \alpha_\sigma^{gas} + s_\sigma^{gas} + \alpha_\sigma^{aerosol} + s_\sigma^{aerosol} \tag{A.2}$$

In case of of a pure gas atmosphere with no-scattering a simple expression is obtained:

$$\mu_\sigma = \alpha_\sigma^{gas} = \alpha_\sigma \tag{A.3}$$

In absence of scattering and for local thermodynamic equilibrium (LTE), the source function is equal to :

$$\rho . j_\sigma = \alpha_\sigma B_\sigma (T) \tag{A.4}$$

where α_σ is the absorption coefficient (equal to the emission coefficient for the Kirchhoff's law) and $B_\sigma (T)$ is the Plank function at frequency σ and temperature *T*.

So, for an atmosphere with no scattering and in LTE the radiative transfer equation is reduced to:

$$\frac{dI_\sigma}{dx} = -\alpha_\sigma . I_\sigma + \alpha_\sigma . B_\sigma (T) \tag{A.5}$$

Losses and gains must obey the second law of thermodynamics. For any term that introduces a loss there must be a term that introduces a gain. In the propagating beam a change of intensity is caused by the difference between the intensity of the source I_σ that is being attenuated and the intensity of the local

source $B_\sigma(T)$. An analytical integral expression of the differential equation of radiative transfer can be obtained for a homogeneous medium.

The differential equation is at point *x* and we want to obtain the integral from x_1 and x_2 .

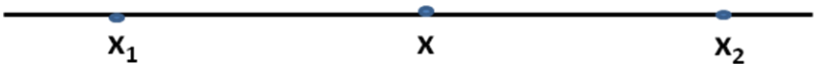

This can be formally obtained by multiplying both terms of the differential equation by (i.e. the attenuation from x_1 to x

$$
\begin{aligned}
& e^{\alpha_\sigma(x-x_1)}.\frac{dI_\sigma}{dx} = \alpha_\sigma.e^{\alpha_\sigma(x-x_1)}.[-I_\sigma + .B_\sigma(T)] \\
& e^{\alpha_\sigma(x-x_1)}.\frac{dI_\sigma}{dx} + \alpha_\sigma.e^{\alpha_\sigma(x-x_1)}.I_\sigma = \alpha_\sigma.e^{\alpha_\sigma(x-x_1)}.B_\sigma(T) \\
& \frac{d}{dx}[e^{\alpha_\sigma(x-x_1)}.I_\sigma] = \frac{d}{dx}[e^{\alpha_\sigma(x-x_1)}].B_\sigma(T)
\end{aligned}
\qquad \text{(A.6)}
$$

An expression is obtained that can be integrated from x_1 to x_2.

$$
\begin{aligned}
& e^{\alpha_\sigma(x_2-x_1)}.I_\sigma(x_2) - e^{\alpha_\sigma(x_1-x_1)}.I_\sigma(x_1) = (e^{\alpha_\sigma(x_2-x_1)} - e^{\alpha_\sigma(x_1-x_1)}).B_\sigma(T) \\
& e^{\alpha_\sigma(x_2-x_1)}.I_\sigma(x_2) = I_\sigma(x_1) + B_\sigma(T).(e^{\alpha_\sigma(x_2-x_1)} - 1) \\
& I_\sigma(x_2) = I_\sigma(x_1).e^{-\alpha_\sigma(x_2-x_1)} + B_\sigma(T).(1-e^{-\alpha_\sigma(x_2-x_1)})
\end{aligned}
\qquad \text{(A.7)}
$$

In the integral expression of radiative transfer

$$I_\sigma(x_2) = I_\sigma(x_1).e^{-\alpha_\sigma(x_2-x_1)} + B_\sigma(T).(1-e^{-\alpha_\sigma(x_2-x_1)}) \qquad \text{(A.8)}$$

the first term is the Lambert-Beer law which gives the attenuation of the external source and the second term gives the emission of the local source.

The modelling of radiative transfer is made more complicated by, scattering, non-LTE and variable medium. In presence of scattering (2.27) becomes $\mu_\sigma = \alpha_\sigma + s_\sigma$ and the differential equation equals to

$$\frac{dI_\sigma}{dx} = -\alpha_\sigma.I_\sigma - s_\sigma.I_\sigma + \alpha_\sigma.B_\sigma(T) + s_\sigma.J_\sigma \qquad \text{(A.9)}$$

Where, $s_\sigma.I_\sigma$ is the loss and $s_\sigma.J_\sigma$ is the gain due to scattering and the and the solution over an homogeneous path from x_1 to x_2 is equal to:

$$I_\sigma(x_2) = I_\sigma(x_1).e^{-(\alpha_\sigma+s_\sigma).(x_2-x_1)} + \frac{\alpha_\sigma.B_\sigma(T) + s_\sigma.J_\sigma}{(\alpha_\sigma - s_\sigma)}.(1-e^{-(\alpha_\sigma+s_\sigma).(x_2-x_1)}) \qquad \text{(A.10)}$$

Radiative transfer is an exchange of energy between the radiation field and the energy levels of molecules and atoms (which are defined by the Boltzman temperature). We are in local thermodynamic equilibrium

(LTE) when the Boltzman temperature is in equilibrium with the kinetic temperature. Of course LTE does not imply a complete equilibrium that includes the radiation field. When an equilibrium exists between the radiation field and the local black-body emission no energy exchange and no radiative transfer occur. The Boltzman temperature is controlled by chemical reaction, radiation absorption and thermal collisions. When the collisions are not frequent enough the Boltzman temperature can be different from the kinetic temperature and we are in non-LTE conditions. When in non-LTE conditions we must consider the different components of the medium and define for each of them their individual temperature *T(i)* and absorption coefficient α_σ *(i)*. In the case of non-LTE conditions, the differential equation of radiative transfer equation is :

$$\frac{dI_\sigma}{dx} = -\sum_i \alpha_\sigma{}^{(i)}.I_\sigma + \sum_i \alpha_\sigma{}^{(i)}.B_\sigma(T^{(i)})$$

and the solution over a path from x_1 to x_2 is equal to (A.11)

$$I_\sigma(x_2) = I_\sigma(x_2).e^{-\sum_i \alpha_\sigma{}^{(i)}(x_2-x_1)} + \frac{\sum_i \alpha_\sigma{}^{(i)} B_\sigma(T^{(i)})}{\sum_i \alpha_\sigma{}^{(i)}}.(1-e^{-\sum_i \alpha_\sigma{}^{(i)}(x_2-x_1)})$$

When the optical and physical properties of the medium are not constant along the optical path, the absorption coefficient α_σ *(x)* and the local temperature *T(x)* depend on the variable of integration *x*. In general, for a non-homogeneous medium the differential equation cannot be analytically integrated. The general integrated radiative transfer equation for non-homogeneous medium is

$$I_\sigma(L) = I_\sigma(0)e^{-\tau_\sigma(0,L)} + \int_0^{\tau_\sigma(0,L)} B_\sigma(T(x))e^{-\tau_\sigma(x,L)} d\tau_\sigma$$

where, (A.12)

$$\tau_\sigma(x,L) = \int_x^L \alpha_\sigma(x')dx'$$

$I_\sigma(L)$ is the spectral intensity observed at L, $e^{-\tau_\sigma(0,L)}$ is the transmittance between 0 and L. $I_\sigma(0)e^{-\tau_\sigma(0,L)}$ represents the absorption term and $\int_0^{\tau_\sigma(0,L)} B_\sigma(T(x))e^{-\tau_\sigma(x,L)} d\tau_\sigma$ represents the emission component.

Appendix B

Taylor Diagrams

Taylor diagrams (Taylor 2001) provide a way of graphically summarizing how closely a pattern (or a set of patterns) matches observations. The similarity between two patterns is quantified in terms of their correlation, their centered root-mean-square difference and the amplitude of their variations (represented by their standard deviations). These diagrams are especially useful in evaluating multiple aspects of complex models or in gauging the relative skill of many different models.

Figure 48 is a sample Taylor diagram which shows how it can be used to summarize the relative skill with which several global climate models simulate the spatial pattern of annual mean precipitation. Statistics for eight models were computed, and a letter was assigned to each model considered. The position of each letter appearing on the plot quantifies how closely that model's simulated precipitation pattern matches observations. Consider model F, for example. Its pattern correlate on with observations is about 0.65. The centered root-mean-square (RMS) difference between the simulated and observed patterns is proportional to the distance to the point on the x-axis identified as "observed." The green contours indicate the RMS values and it can be seen that in the case of model F the centered RMS error is about 2.6 mm/day. The standard deviation of the simulated pattern is proportional to the radial distance from the origin. For model F the standard deviation of the simulated field (about 3.3 mm/day) is clearly greater than the observed standard deviation which is indicated by the dashed arc at the observed value of 2.9 mm/day.

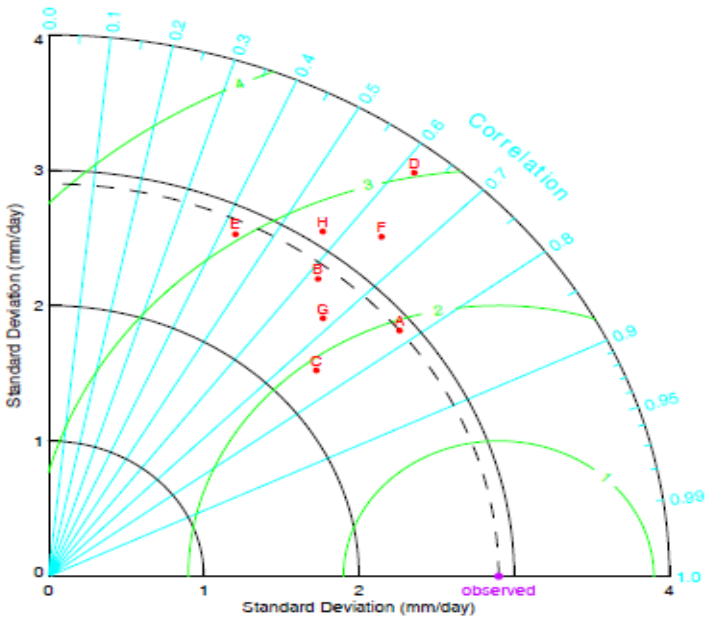

Figure 48: Sample Taylor diagram displaying a statistical comparison with observations of eight model estimates of the global pattern of annual mean precipitation.

The relative merits of various models can be inferred from Figure 48. Simulated patterns that agree well with observations will lie nearest the point marked "observed" on the x-axis. These models will have

relatively high correlation and low RMS errors. Models lying on the dashed arc will have the correct standard deviation (which indicates that the pattern variations are of the right amplitude). In Figure 48, it can be seen that models A and C generally agree best with observations, each with about the same RMS error. Model A, however, has a slightly higher correlation with observations and has the same standard deviation as the observed, whereas model C has too little spatial variability (with a standard deviation of 2.3 mm/day compared to the observed value of 2.9 mm/day). Of the poorer performing models, model E has a low pattern correlation, while model D has variations that are much larger than observed, in both cases resulting in a relatively large (~3 mm/day) centered RMS error in the precipitation fields. Note also that although models D and B have about the same correlation with observations, model B simulates the amplitude of the variations (i.e., the standard deviation) much better than model D, and this results in a smaller RMS error.

In summary, the Taylor diagram characterizes the statistical relationship between two fields, a "test" field (often representing a field simulated by a model) and a "reference" field (usually representing “truth”, based on observations). Note that the means of the fields are subtracted out before computing their second-order statistics, so the diagram does not provide information about overall biases, but solely characterizes the *centered* pattern error.

Declaration

I herewith declare that I have produced this paper without the prohibited assistance of third parties and without making use of aids other than those specified; notions taken over directly or indirectly from other sources have been identified as such. This paper has not previously been presented in identical or similar form to any other Italian or foreign examination board.

The thesis work was conducted from November 2010 to November 2013 under the supervision of Professor Paolo Ferrazzoli at the Dipartimento di Ingegneria Civile e Ingegneria Informatica (DICII), University of Rome Tor Vergata, Italy

ROME,